SYNTHESIS AND INVESTIGATION OF OPTICAL PROPERTIES OF Ce^{3+}, Dy^{3+}, Eu^{3+} SINGLE DOPED, Ce^{3+}/Dy^{3+} CODOPED, $Dy^{3+}/Ce^{3+}/Eu^{3+}$ AND Yb^{3+} SINGLE DOPED, $Tb^{3+}/Ce^{3+}/Yb^{3+}$ TRIPLE DOPED $GdBO_3$

A THESIS SUBMITTED TO
THE GRADUATE SCHOOL OF NATURAL AND APPLIED SCIENCES
OF
MIDDLE EAST TECHNICAL UNIVERSITY

BY

OĞUZCAN TANEROĞLU

IN PARTIAL FULFILLMENT OF THE REQUIREMENTS
FOR
THE DEGREE OF MASTER OF SCIENCE
IN
CHEMISTRY

SEPTEMBER 2020

Approval of the thesis:

SYNTHESIS AND INVESTIGATION OF OPTICAL PROPERTIES OF Ce^{3+}, Dy^{3+}, Eu^{3+} SINGLE DOPED, Ce^{3+}/Dy^{3+} CODOPED, $Dy^{3+}/Ce^{3+}/Eu^{3+}$ AND Yb^{3+} SINGLE DOPED, $Tb^{3+}/Ce^{3+}/Yb^{3+}$ TRIPLE DOPED $GDBO_3$

submitted by **OĞUZCAN TANEROĞLU** in partial fulfillment of the requirements for the degree of **Master of Science in Chemistry, Middle East Technical University** by,

Prof. Dr. Halil Kalıpçılar
Dean, Graduate School of **Natural and Applied Sciences**

Prof. Dr. Cihangir Tanyeli
Head of the Department, **Chemistry**

Prof. Dr. Ayşen Yılmaz
Supervisor, **Chemistry, METU**

Prof. Dr. Okan Esentürk
Co-Supervisor, **Chemistry, METU**

Examining Committee Members:

Prof. Dr. Ceyhan Kayran İşçi
Chemistry, METU

Prof. Dr. Ayşen Yılmaz
Chemistry, METU

Prof. Dr. Okan Esentürk
Chemistry, METU

Prof. Dr. Enver Bulur
Physics, METU

Assistant Prof. Dr. Ferdi Karadaş
Chemistry, Bilkent University

Date: 23.09.2020

I hereby declare that all information in this document has been obtained and presented in accordance with academic rules and ethical conduct. I also declare that, as required by these rules and conduct, I have fully cited and referenced all material and results that are not original to this work.

Name Last name: Oğuzcan Taneroğlu

Signature:

ABSTRACT

SYNTHESIS AND INVESTIGATION OF OPTICAL PROPERTIES OF Ce^{3+}, Dy^{3+}, Eu^{3+} SINGLE DOPED, Ce^{3+}/ Dy^{3+} CODOPED, Ce^{3+}/Dy^{3+}/ Eu^{3+} TRIPLE DOPED AND Yb^{3+} SINGLE DOPED, Ce^{3+}/Tb^{3+}/ Yb^{3+} TRIPLE DOPED $GDBO_3$

Taneroğlu, Oğuzcan
Master of Science, Chemistry
Supervisor: Prof. Dr. Ayşen Yılmaz
Co-Supervisor: Prof. Dr. Okan Esentürk

September 2020, 137 pages

The effect of triple doping in photoluminescence has been investigated in recent years, and it could utilize the compounds in terms of some demands. The photoluminescence activity of the materials can be used for quantum cutting solar cells, white light-emitting diodes, flat display panels, optical thermometer, or for the purpose of biosensor, etc.

Single doped Ce^{3+}, Dy^{3+}, Eu^{3+}, Yb^{3+} doped, and Ce^{3+}/Dy^{3+} codoped, Dy^{3+}/Ce^{3+}/Eu^{3+} and Tb^{3+}/Ce^{3+}/Yb^{3+} triple doped $GdBO_3$ nanocompounds were synthesized by sol-gel method using metal oxides and carbonates as precursors in this study.

Crystal structure, vibrational band modes, photoluminescence properties of all produced compounds were characterized by X-Ray Diffraction (XRD), IR Transmission, Fluorescence spectrometers, respectively. Besides, the decay lifetimes and quantum yield of selected samples were calculated. Scattering Electron Microscope (SEM) was used for the determination of the morphology of the crystals. The colors of phosphors were determined by CIE 1931 color space chromaticity coordinates.

X-Ray patterns prove that all synthesized compounds except for 7% Dy^{3+} doped one compound have the same crystal structure with pure $GdBO_3$. FTIR results showed that sol-gel all synthesized $GdBO_3$ compounds had $B_3O_9^{9-}$ in their structure. With this study, also, the emission intensity of Dy^{3+} was ion increased by Ce^{3+}-Dy^{3+} energy transfer. The emission of Eu^{3+} was increased by using Dy^{3+}-Eu^{3+} energy transfer and increased energy of Dy^{3+} ion in the case of a small amount of Eu^{3+} ion. Moreover, Ce^{3+}-Tb^{3+} and Yb^{3+}-Tb^{3+} energy transfers were examined, and both downconversion and upconversion properties could be measured in one compound. Furthermore, according to luminescence measurements, the colors of the samples can be tuned by codoping.

Keywords: Gadolinium Borate, Gadolinium, Luminescence, Rare Earth Elements,

ÖZ

Ce^{3+}, Dy^{3+}, Eu^{3+} TEKİ KATKILAMALARININ , Ce^{3+}/Dy^{3+} İKİLİ KATKILAMALARININ , $Ce^{3+}/Dy^{3+}/Eu^{3+}$ ÜÇLÜ KATKILAMALARININ VE Yb^{3+} TEKLİ KATKILAMASININ , $Ce^{3+}/Tb^{3+}/Yb^{3+}$ ÜÇLÜ KATKILAMALARININ $GdBO_3$ YAPISI ÜZERİNDE SENTEZLENMESİ VE OPTİK ÖZELLİKLERİNİN İNCELENMESİ

Taneroğlu, Oğuzcan
Yüksek Lisans, Kimya
Tez Yöneticisi: Prof. Dr. Ayşen Yılmaz
Ortak Tez Yöneticisi: Prof. Dr. Okan Esentürk

Eylül 2020, 137 sayfa

Son yıllarda üçlü katkılamanının üzerindeki etkisi incelenmekte ve birkaç anlamda kullanılabilmeltedir. Malzemelerin fotoluminesans aktiviteleri kuantum kesme güneş pilleri, beyaz ışık yayan diyotlar, ekranlar, optik termometreler ve biyosensör amacı ile kullanılabilmektedir.

Bu çalışmada, tekli Ce^{3+}, Dy^{3+}, Eu^{3+}, Yb^{3+}, ikili katkılanmış Ce^{3+}/Dy^{3+}, üçlü katkılanmış $Ce^{3+}/Dy^{3+}/Eu^{3+}$ ve $Ce^{3+}/Tb^{3+}/Yb^{3+}$ gadolinyum borat kristalleri nadir toprak element oksitleri ve karbonatları başlangıç, malzemeleri olmak üzere kullanılarak, sol-gel yöntemiyle sentezlenmiştir.

Bütün sentezlenen malzemelerin kristal yapıları, titreşim bantları, fotoluminesans özellikleri X-Işını saçılımı, kızıl ötesi geçirim ölçümleri ve florosans spekrometresiyle ölçülmüştür. Ayrıca, belirlenen örneklerin, ışınım zamanları ve kuantum verimlilikleri hesaplanmıştır. Parçacık boyutu tayini için taramalı elektron mikroskopu kullanılmıştır. Fosforların renkleri CIE 1931 renk uzayı ile tayin edilmiştir.

X-ray desenleri 7% Dy^{3+} katkılanmış örnekler haric bütün örneklerin bileşik ile aynı kristal yapısına sahip olduğunu kanıtlamıştır. FTIR sonuçları sentezlenen malzemelerin yapılarında $B_3O_9^{9-}$ grubuna sahip olduğunu göstermistir. Bu çalışmayla birlikte Dy^{3+} iyonunun emisyonu, Ce^{3+} sensitizasyonu ve Ce^{3+}-Dy^{3+} enerji transferi kullanılarak artırıldı. Dy^{3+}-Eu^{3+} enerji transferi ve Dy^{3+} iyonunun artırılmış enerjisi kullanılarak Eu^{3+} iyonunun emisyonu düşük konsantrasyonlarda artırıldı. Dahası, Ce^{3+}-Tb^{3+} ve Yb^{3+}-Tb^{3+} enerji transferleri kullanılarak, tek bir malzemeden yukarı dönüşüm ve aşağı dönüşüm özellikleri gözlemlenebilmektedir. Üstelik malzemelerin renkleri ikili katkılama ile ayarlanabilmektedir.

Anahtar Kelimeler: Gadolinyum Borat, Gadolinyum, Lüminesans, Nadir Toprak Elementleri,

To my family and my dear friend Ali Baran…

ACKNOWLEDGMENTS

Firstly, I would like to thank my supervisor, Prof. Dr. Ayşen Yılmaz, for the opportunity she gave to me for her endless support and patience. All the things I have learned from her were invaluable.

I would like to thank my thesis co-supervisor, Prof. Dr. Okan Esentürk, for his guidance and Prof Dr. Ahmet Önal for his collaboration in luminescence studies, and Prof. Dr. Enver Bulur for decay lifetime and quantum yield measurements, also sharing his knowledge.

I would like to thank Prof. Dr. Özgül Persil Çetinkol for her support about measurements of photoluminescence.

I would like to thank my laboratory mates, Gençay Çelik, Özde Ceren Abacı, Mehmet Burak Uzun, for their friendship and endless support.

I would like to thank my great laboratory friend Dr. Sera İflazoğlu for her endless support and guidance, and she is like an older sister for me.

Lastly, I would like to thank my family for making me, as I know.

.

TABLE OF CONTENTS

CHAPTERS

LIST OF TABLES

TABLES

LIST OF FIGURES

FIGURES

CHAPTER 1

INTRODUCTION

1.1 Boron

Boron, a semi-metal element, is in group 3A in the periodic table, and its atomic number is five. As all of its isotopes considered, the most common and stable ones are with atomic numbers ten and eleven. At room temperature, elemental boron occurs as a solid as black monoclinic crystal or as a yellow or brown amorphous powder if it has an impurity. The values of specific gravities of amorphous and crystalline boron are 2.37 and 2.34 (can be used as density), respectively. Boron is mostly found in rocks, soil, and water as salts because of its high reactivity. Some of the compound which is boron primarily located in the compounds is given in **Table 1.1**. (Environmental Health Care, p.12) Most of the soils have boron of less than 10 ppm. The average concentration of boron in soil is 10 to 20 ppm, and only a few of world area is not boron deficient. Boron concentrations change in different sources, such as in rocks range from 5 ppm in basalts to 100 ppm in shales and averages ten ppm in earth crust overall. (Woods, 1994) As boron exists in the earth's crust, it can also be found in the water sources. Seawater contains an average of 4.6 ppm boron but ranges from 0.5 to 9.6 ppm. Freshwaters typically range from <0.01 to 1.5 ppm with relatively higher concentrations in regions of high boron soil levels. (Mellor, 1929) On earth, boron element exists as borate minerals in 230 different species and borosilicate. (Helvaci, 2015)

Table 1.1 Most common sources and their properties of Boron (Environmental Health Care)

Substance	*Relative Molecular Mass*	*Color*	*% Boron*	*Relative Density*	*Water Solubility*	*Melting Point (℃)*	*Boiling Point*
Borax Pentahydrate ($Na_2B_4O_7.5H_2O$)	291.35	White	14.55	1.81	3.6 g/100 g at 20 ℃	742	--
Borax	381.37	Colorless	11.34	1.73	5.92 g/100 g at 25 ℃	75, Decomposes	--
Ulexite	810.6	White	13.33	1.62	Slightly Soluble	Decomposes	--
Colemanite	411.1	White	15.78	2.42	Slightly Soluble	Decomposes	--
Sodium Perborate Tetrahydrate	153.9	White	7.03	1.73	23 g/1L at 20 ℃	Decomposes	--
Sodium Perborate Monohydrate	99.8	White	10.83	--	15 g/1L at 20 ℃	Decomposes	--
Boric Acid	61.84	Colorless	17.48	1.435 at 15 ℃	63.5 g/1L at 20 ℃	169	--
Anhydrous Borax	201.22	White	21.49	2.367	2.556 g/1L at 20 ℃	741	1575
Boron Oxide	69.62	Colorless	31.06	2.46	Slightly Soluble	450	1860
Boron	10.81	Black crystal, or yellow-brown amorphous	100	2.3	Insoluble	2300	3500

1.2 Borates

Minerals, which include or supply boric oxide (B_2O_3), are named as borates. (Helvaci, 2015) They have various application fields different from luminescence, such as the production of leather, carpet or fertilizer, manufacture of porcelain, glass, etc. (Vengosh, Heumann, Juraske, & Kasher, 1994). The identification of compounds is made by using oxygen and boron atoms interchangeably. Simply, the groups are named according to the boron-oxygen network. These groups are firstly given by Krogh-Moe and summarized by Konijnendijk. This notation is used for anhydrous borate compounds. **Table 1.2** is provided for known examples of these compounds. (Mazelev, 1960)

Table 1.2 Table of some borate structure (Mazelev, 1960)

Formula	*Notation*
$Mg_3B_2O_6$	Magnesium Orthoborate
$Mg_2B_2O_5$	Magnesium Pyroborate
$Na_2B_2O_4$	Sodium Metaborate
$Na_2B_4O_7$	Sodium Diborate
$Na_2B_6O_7$	Sodium Triborate
$Na_2B_8O_{13}$	Sodium Tetraborate
$K_2B_{10}O_{16}$	Potassium Pentaborate
$Cs_2B_{18}O_{28}$	Caesium Anneaborate

For this nomenclature, bonding and configuration of BO_3 and BO_4 units are used. Indefinable structural elements containing more than one boron will be termed as either a ‘group’ or ‘structural grouping’. Krogh-Moe gave detailed fundamental examples from his article. (Mazelev, 1960) **Figure 1.1** and **Figure 1.2** are shown for the representation of these groups.

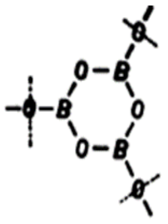

The boroxol ring (a_3), observed in vitreous B_2O_3.

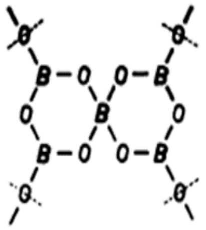

The pentaborate group (a_4c), observed in the compounds α-$K_2O . 5 B_2O_3$ and β-$K_2O . 5 B_2O_3$.

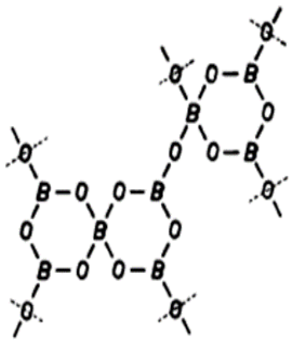

The tetraborate group (a_6c_2), observed in the compound $Na_2O . 4 B_2O_3$.

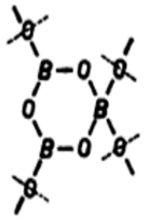

The triborate group (a_2c), observed in the compound $Cs_2O . 3 B_2O_3$.

The diborate group (a_2c_2), observed in the compound $Li_2O . 2 B_2O_3$.

Figure 1.1. Some borate groups (Mazelev, 1960)

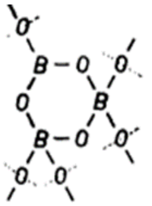

The di-triborate group (ac_2), observed in the compound $K_2O \cdot 2\,B_2O_3$.

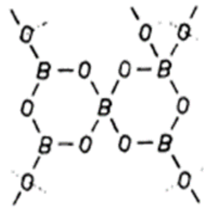

The di-pentaborate group (a_3c_2), observed in the compound $Na_2O \cdot 2\,B_2O_3$.

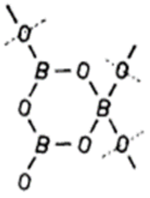

The triborate group with one non-bridging oxygen ion (abc), observed in the compound $Na_2O \cdot 2\,B_2O_3$.

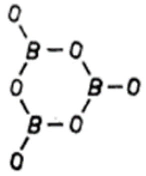

The ring-type metaborate group (b_3), observed in the compounds $Na_2O \cdot B_2O_3$ and $K_2O \cdot B_2O_3$.

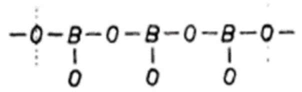

The chain-type metaborate group (b_∞), observed in the compounds $Li_2O \cdot B_2O_3$ and $CaO \cdot B_2O_3$.

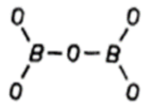

The pyroborate group (b_2''), observed in the compounds $2\,MgO \cdot B_2O_3$ and $2\,CaO \cdot B_2O_3$.

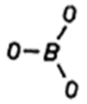

The orthoborate group (b'''), observed in the compounds $3\,MgO \cdot B_2O_3$ and $3\,CaO \cdot B_2O_3$.

Figure 1.2. Some borate groups (Mazelev, 1960)

1.3 Phosphors

The word ‘phosphor’ originated from Greek and is used to name the luminescent or light-emitting materials. (Capper, Kasap, & Willoughby, 2010) Phosphors are commonly solid inorganic species involving a host lattice, usually intentionally doped with impurities (also called “dopant”).

The absorption of energy applied to materials for excitation of luminescence is exposed by readily doped impurities or by host lattice. In most cases, electromagnetic radiation is accepted by the impurity ions, named activator ions, when they bring out the desired emission. However, sometimes, activator ions can show very weak absorption. In this case, the second kind of impurity can be added, and it is called as sensitizer. Sensitizers are used when the activator of host materials do not work properly by means of luminescence. (Cornelis R. Ronda, 2008)

1.4 Luminescence Mechanism

There are two most common ways to create a light, and these are incandescence and luminescence. Incandescence is observed from materials given heat energy (such as the sun). Luminescence is a general term for forms of cold light. (Thejo Kalyani & Dhoble, 2012)The ‘luminescence’ phenomenon (the literal translation from Latin “weak glow”) is explained as the emission of electromagnetic radiation from phosphors when they are exposed to absorption energy, was firstly named by Eilhard Wiedemann who is a German physicist for the characterization of emission of light with no change in the temperature of the compound in 1888. (Gribovskii, V. P. et al., 1998)

There are two primary mechanisms for luminescence: *intrinsic* and *extrinsic luminescence*. Intrinsic defects emerge as a consequence of the removal of an atom in a matrix being from the initial position to an interstitial position. This removal allows a point defect, providing a vacancy defect in the structure. Luminescence emerges with absorbed electromagnetic radiation, and this excessive energy brings the transition of electrons from the valence band to the conduction band. After that, the particles are de-excited to the valence band via a luminescent center, explained in the next sections. These luminescent centers can be either intrinsic or extrinsic defects. When a material with intrinsic defects absorbs radiation, they leave holes with a positive charge in its valence band. With this positive charge's help, the donor level applies a columbic force onto the excited electrons in the conduction band and attracts them.

Equivalently, as there are positively charged holes in the valence band, there are negative charges in the acceptor level caused by extra electrons. The negative charge of the acceptor level attracts the free holes in the valence band. These events exist in a bound state temporarily, and finally, the electrons are released to recombine with the holes. During this process, electrons lose their energy, and the system releases electromagnetic waves. (Luyanda L. Noto, Hendrik C. Swart, Bakang M. Mothudi, 2011)Extrinsic defects are different from intrinsic defects. Dopant atoms or ions are incorporated deliberately with the structure of the host structure to generate a luminescent center.

The excited electrons release their energy to the luminescent center, further de-excite to a less energetic state of the center radiatively by releasing electromagnetic radiation with different frequencies. The frequencies of the waves depend on the ion-doped for the luminescent center. It is also essential that when the luminescent center is excited, the excitation of the conduction band emerges directly. (Luyanda L. Noto, Hendrik C. Swart, Bakang M. Mothudi, 2011) The schematic representations of both types are given in **Figure1.3**.

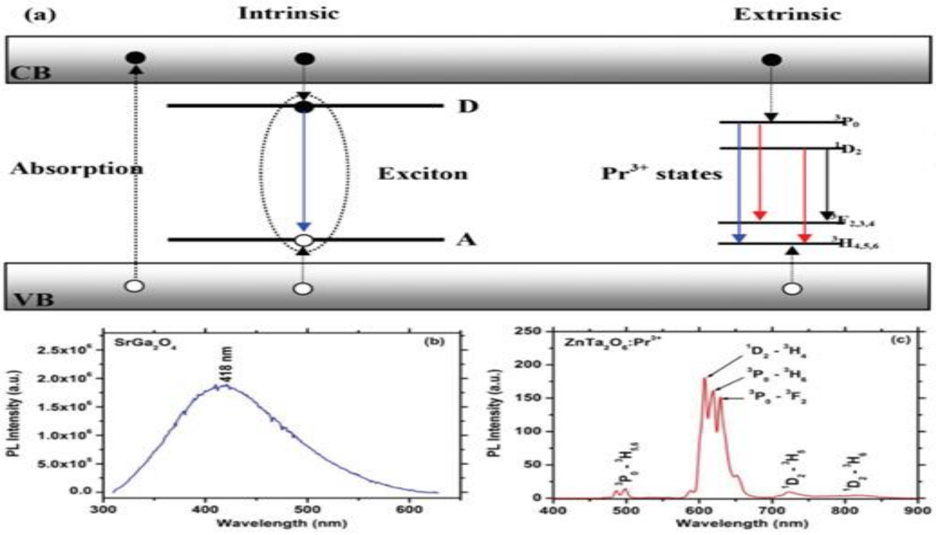

Figure 1.3. (a) The diagram shows emission from both intrinsic and extrinsic defects (b) An emission spectrum and (c) An emission spectrum of $ZnTa_2O_4$: Pr^{3+}(Luyanda L. Noto, Hendrik C. Swart, Bakang M. Mothudi, 2011)

For extrinsic luminescence, several radiative and non-radiative events. A diagram was created by Aleksander Jabłoński to simplify these events. A Jablonski diagram is given in **Figure 1.4**. Nevertheless, to understand this diagram, it is necessary to know some terms.

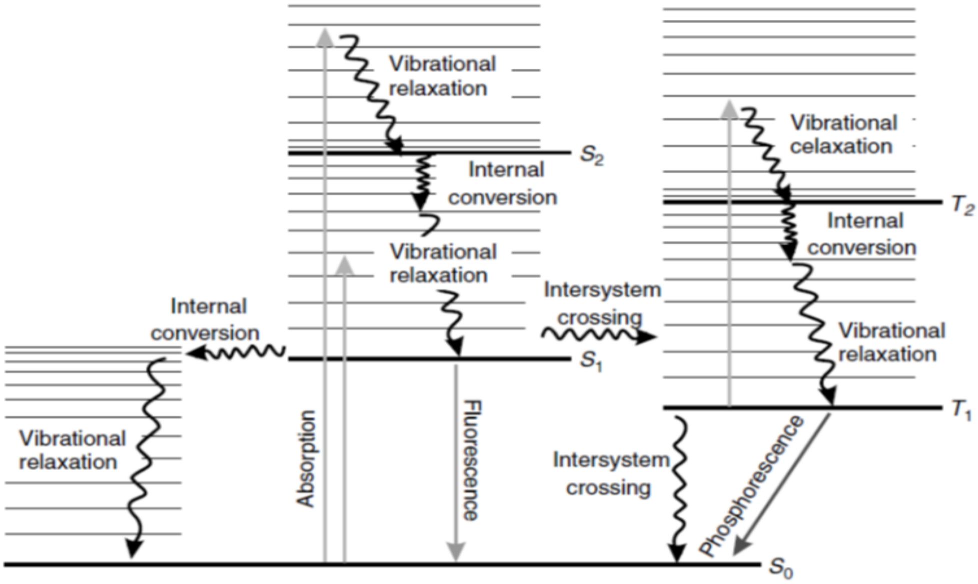

Figure 1.4. Jablonski diagram (Sauer, Hofkens, & Enderlein, 2011).

Absorption is the conversion of radiative energy to a different type of energy, usually heat or electromagnetic energy, by their interaction with matter. An electron is defined as a subatomic particle that turns around the nucleus with a specified distance, the electron shell. The number of shells and electrons in the shells change according to the type of atom or ion. The electrons arranged in the shells closest to the nucleus keep less energy than the further shells' electrons. When particular atoms or ions are exposed to electromagnetic (or radiative) energy, a photon will provide residing energy for the electrons in a lower-energy shell to be temporarily promoted to a higher-energy shell. The electrons are ‘excited’.(H. Zhang, Chen, Liu, & Zhang, 2020). Optical absorption permits a compound to place to higher probable one of vibrational states of its electronically excited states. Therefore, the excited compound has to release some energy. Absorbed energy is released either in a non-radiative or radiative way. Non-radiative processes are *vibrational relaxation*, *internal conversion,* and *intersystem crossing*. *Vibrational relaxation* is the effect that a compound relaxes to its ground state within picoseconds. The second process is *internal conversion*, which is the dissipation of excess vibrational energy as heat. The time necessary for the internal conversion is commonly much less than that for other radiative processes. The electrons in the excited state S_1 can also undergo *intersystem crossing*; it is a non-radiative transition between states of different spin multiplicity. A transition to the triplet state T_1 is usually followed by another radiative or non-radiative deactivation. (Jain, Blum, & Subramaniam, 2009)

Compounds, which do not acquire adequate non-radiative decay channels, can consume their excitation energy upon a photon's radiation. There two ways of this process, which are fluorescence and phosphorescence. Fluorescence and phosphorescence are distinguishable according to their different electronic nature. (Jain et al., 2009)

Fluorescence is the process that occurs when the internal conversion and vibrational relaxation cause the electronically excited compound in the lowest vibrational sublevels of the first singlet excited state, and the resulting electron provides a photon. An excited fluorescence compound commonly remains in the S_1 state, which is the lowest excited state, and finally released to its energy in order to go to the ground state. (Jain et al., 2009)(smaller than 10^{-8} s). (H. Zhang et al., 2020) The resulting product of this process is commonly light in the visible range. The process is explained mathematically.

Excitation: $S_0 = hv_{ext} + S_1$

Fluorescence (emission): $S_1 \rightarrow S_0 + hv_{em}$ + heat

Phosphorescence is a specific type of photoluminescence. Compounds, which phosphoresce, do not emit absorbed light immediately. The larger time scales of emission of radiation are related to 'forbidden' energy state transitions. All along the phosphorescence process, a compound in the excited triplet state may not often undergo the intersystem crossing to turn back to its ground state; instead, it loses its energy by emitting a photon. A transition, which changes the angular momentum number of an electron, is less probable than the transition, in which an electron remains its angular momentum number. The time-domain for this process can be up to 10 seconds. Internal conversion and radiationless transition processes challenge so profitably with phosphorescence, mostly seen only at low temperatures or in quite viscous (or dense) media. (Thejo Kalyani & Dhoble, 2012) In the case of photoluminescence, both fluorescence and phosphorescence can occur in the compounds. In **Figure 1.5**, characteristic times consumed for the optical processes are given.

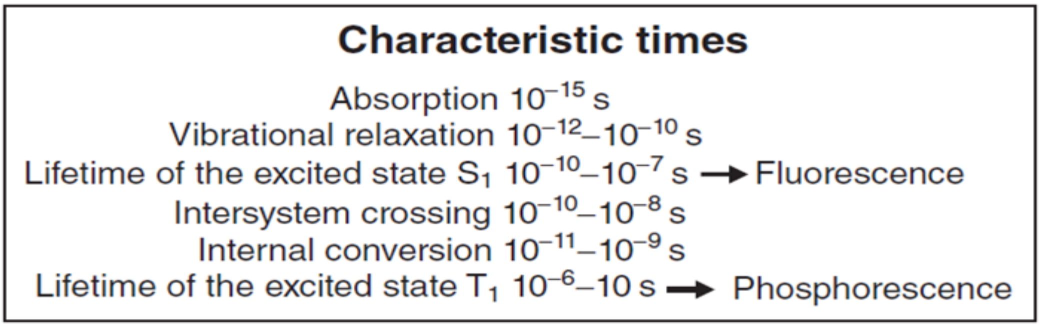

Characteristic times

Absorption 10^{-15} s
Vibrational relaxation 10^{-12}–10^{-10} s
Lifetime of the excited state S_1 10^{-10}–10^{-7} s → Fluorescence
Intersystem crossing 10^{-10}–10^{-8} s
Internal conversion 10^{-11}–10^{-9} s
Lifetime of the excited state T_1 10^{-6}–10 s → Phosphorescence

Figure 1.5. Tabulated values for times of some processes (Valeur & Berberan-Santos, 2012)

In addition, there is three explanation of releasing the absorbed energy in terms of quantity of energy of released light for the concept of photoluminescence. These are Rayleigh scattering, Stokes’ shift, and anti-Stokes’ shift. Rayleigh scattering is the event that the quantity of absorbed light is equal to the amount of emitted light. In the case of Stokes’ shift, the energy of absorbed light is larger than the emitted light and, for anti-Stokes’, it is vice versa. For fluorescence and phosphorescence, compounds undergo Stokes’ shift. Stokes’ shift is very important for Stokes’ shift in the spectrum founds out the detection of fluorescence since the difference of Rayleigh scattered incident light from fluorescence. Moreover, Stokes’ shift is essential for down-conversion, and downshifting and anti-Stokes’ shift is vital for upconversion. (H. Zhang et al., 2020)

1.4.1 Luminescent Center

The luminescent center is an ion or a molecular complex that generates the emission by the optical transition between the host matrix states or different species. (Cornelis R. Ronda, 2008)

The environment of the dopant ions dynamic: surrounding ions have some vibrational motion about some average positions; therefore, the crystal field changes. The configurational coordinate model is the simplest model for the explanation of this varying field effect. In this mode, it is considered as only one vibrational mode, which is named as breathing mode. This mode is movement (symmetrical stretching) that the dopant ion goes in and out around the lattice of the host matrix. The configurational coordinate (Q) represents the vibration.

Before the explanation of this model, it is imperative to know the term ‘Frank-Condon’ principle. Electronic absorption of light emerges in less than 10^{-15} seconds, and because of a short time, the nucleus of an atom is assumed to ‘frozen’. Due to that assumption, the transition between various energy levels is represented as ‘vertical’ transitions in the energy level diagram of atoms. It is known as the

‘Frank-Condon principle’. The principle states that the displacement of the nucleus is negligible during electronic transitions. (Lindon, Tranter, & Holmes, 1942) **Figure 1.6** is an illustration of the principle mathematically.

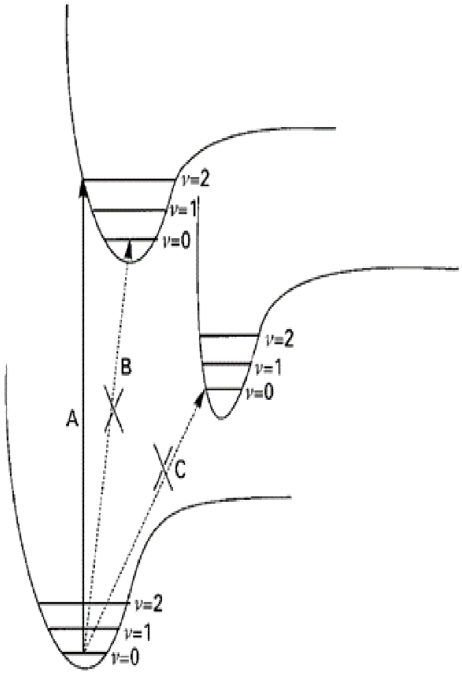

Figure 1.6. The Franck-Codon principle. Only the vertical electronic transition is allowed.

As is seen in the diagram, only transition A occurs since electronic transitions have to be vertical. Transition A, B, and C represented in the figure explain the reason for the absorption. Other than transition A, transition B, and C, they do not occur according to the model since they are not vertical. The model explains Transition B as a representation of the transition from the ground state to excited state v=0 and transition C as the transition from the ground state to T_1 state. (Lindon et al., 1942)

If the model is considered, the central atom is regarded as a reference point, so if it is assumed that Q is the distance between two atoms and energy versus distance (Q), electronic states parabola can be observed as a harmonic oscillator. In this plot, u is used for the ground state, and v is used for the excited state, and also, Q_0 represents the equilibrium distance, and Q_0’ represents the excited state distance.

Figure 1.7 illustrates the configurational coordinate diagram; it is the coordinate system, which is energy versus position (coordinate). The shapes of parabolas can change according to the bond strength of atoms. If the interaction is weak, the parabola will be broader or vice versa. (Maccari et al., 1991) **Figure 1.7** represents a relatively basic configurational coordinate diagram.

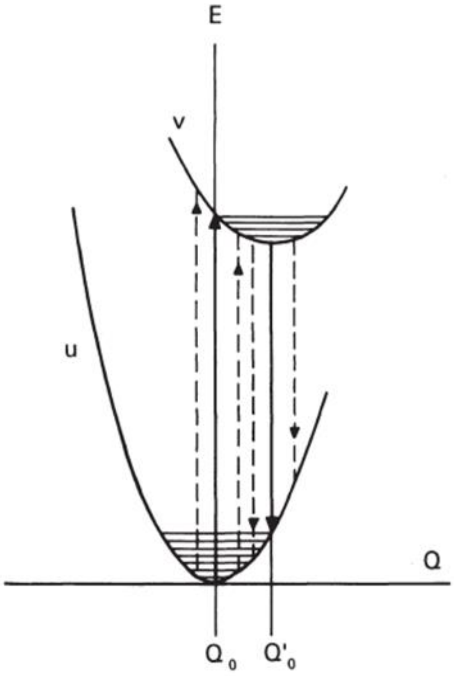

Figure 1.7. Representation of configurational coordinate diagram.

Parabola u and parabola v are states of particles. In the case of optical excitation, absorption refers to the transition from u to the v state, and emission is reverse transition. In this diagram, it is crucial to understand what occurs after the absorption. Firstly, the compound releases few of its energy to the lattice to drop to the lowest vibrational level of state v, which is the relatively higher energy state. This released energy is heat. The transition for emission is described in the same way as the transition for absorption. Lastly, the system relaxes within u parabola to the lowest vibrational level.

Besides, suppose the surrounding temperature is not low. In that case, it is evident that a higher vibrational level can be occupied thermally so that the process does not begin from the level higher from n=0.

Although according to Franck-Condon principle, the nuclei of excited compounds are not movable, empirically, it is not so observable. This difference emerges from variation between the bonding (molecular orbitals) properties of the ground and excited states. The diagrams shown below represent the two cases of excited state distortion. The transitions given are the diagrams that are called a vibronic transition. A vibronic transition is a transition that includes a change in both electronic and vibrational states. **Figure 1.8** shows the difference between non-zero distortion and zero distortion cases by means of potential energy.

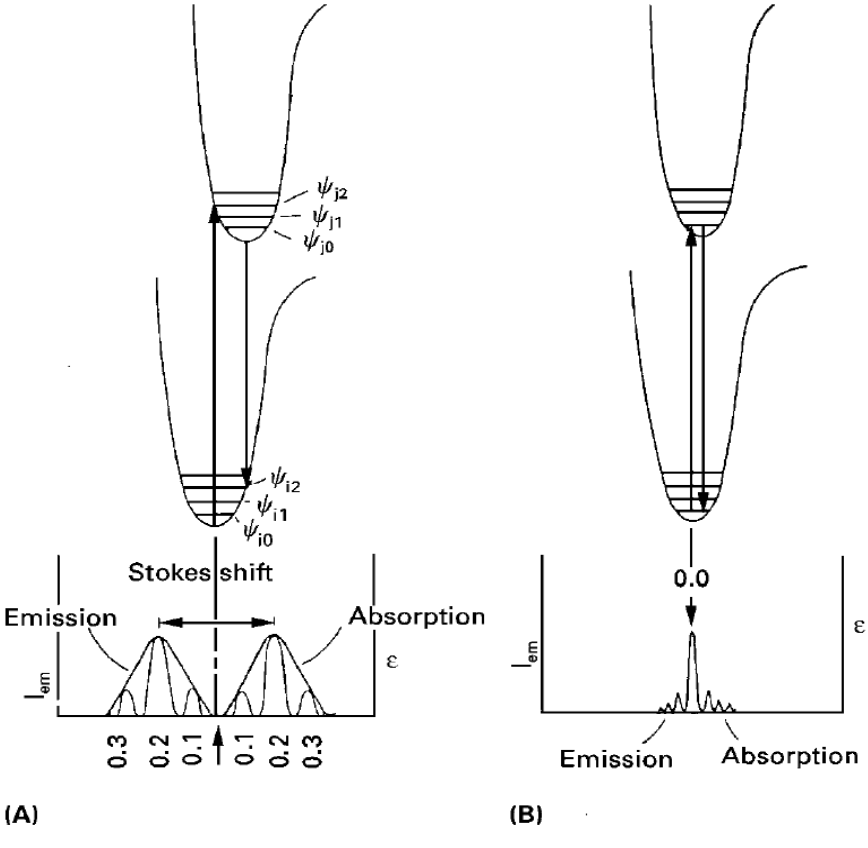

Figure 1.8. Potential energy diagrams for two cases of excited state distortions: (A) non-zero distortion and (B) zero distortion.

The case given in **Figure 1.8.B** shows an extraordinary case in which the excited state distortion is virtually zero. The electronic transition from ground state v=0 to excited state v=0 (called '0-0 vibronic transition' is the most probable one, and thus, intensities are highest for both absorption and emission. Suppose the excited state distortion is remarkable, as it is in Figure 1.8.A. In that case, the probability of 0-0 vibronic transition decreases, and the intensity of 0-0 vibronic transition will be much weaker than the other 0-vibronic transition with higher v values. (Lindon et al., 1942)

1.4.2 Energy Transfer

Energy transfer is explained as the process in which an excited molecule (donor) or atom gives absorbed energy to an acceptor atom or molecule during the lifetime of the donor excited state. (Lindon et al., 1942) Energy transfer between Rear Earth Metal ions has various applications in infrared quantum counters, sensitizing the solid-state laser as well as infrared to visible converters. Aside from energy transfer with the help of displacement of charge transports, there are mainly four mechanisms for the energy transfer between rare earth ions, resonant radiative transfer through the emission of sensitizer, and absorption by activator; non-radiative transfer associated with the resonance between absorber (sensitizer) and emitter (activator); multiphonon –assisted energy transfer; cross-relaxation between two identical ions. These processes are given schematically in **Figure 1.9**. (Q. Y. Zhang & Huang, 2010)

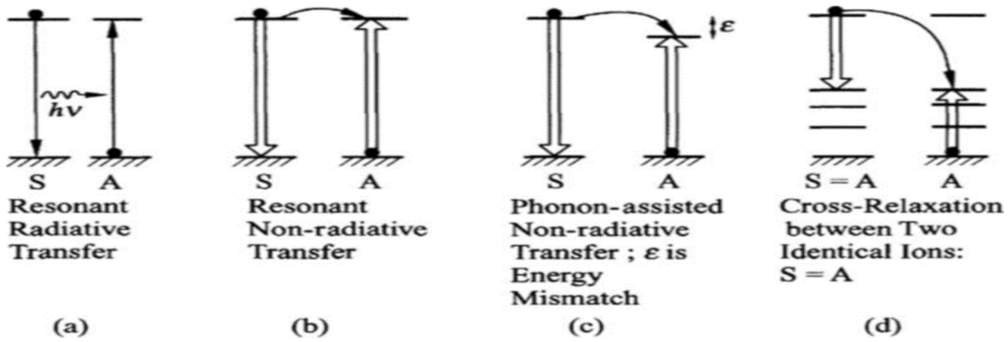

Figure 1.9. Energy transfer processes: (a) Resonant Radiative Transfer, (b) Resonant Non-radiative Transfer, (c) Phonon-assisted Non-radiative Transfer, (d) Cross-Relaxation between Two Identical Ions (A is for activator and S is for sensitizer) (Q. Y. Zhang & Huang, 2010)

First, it is crucial how efficiently fluorescence of the activator is excited by sensitizer emission. A compelling spectral overlap between the emission of sensitizer and the absorption of activator and a perceptible intensity of the activator's absorption is required for energy transfer efficiency. The decay time of the sensitizer fluorescence does not change with the activator's concentration when the radiative energy transfer occurs mainly. (Q. Y. Zhang & Huang, 2010). In this type of mechanism, there is significant interaction between sensitizer and activator. (Lindon et al., 1942)Contrary to the radiative energy transfer, the non-radiative energy transfer has a longer decay time. As a consequence of the requirement for a noticeable absorption competence of activator, the radiative energy transfer can commonly be ignored relative to non-radiative energy transfer in most inorganic systems. Energy transfer can happen when the energy gap between the ground and excited states ıd donor (sensitizer) and the energy gap between these states of the acceptor (activator) are equal. (Nawalha & Rohwer, 2003)

Energy transfer occurs with the help of phonon when differences between ground states of donor and acceptor and excited states of donor and acceptor are not massive in the material. If two rare earth metal ion has different excited states, the probability of energy transfer between donor and acceptor is equal to zero experimentally. However, it is observed that a small energy mismatch (=100 cm^{-1})

it can be achieved by one or two phonon assistance. On the other hand, in the case of rare-earth ions, it is commonly high as several thousand reciprocal centimeters, and for the energy transfer, multiphonon processes are encountered. The number of phonons is mainly proportional to electron-lattice coupling, the temperature of the host matrix, and the energy of phonons that emerged from the processes. (Miyakawa & Dexter, 1970) Lastly, when the Cross-Relaxation process is considered, all types of energy transfers of downconversion processes between identical ions. Cross-Relaxation can increase when the diffusion process considered between the levels included of sensitizers are similar unless it can cause self-quenching. There is no loss in the transferred energy in the first case, so the emitted photons; however, in the second, there is a loss or a change in the emitted photons.

1.4.3 Downshifting and Downconversion

Downshifting is the phenomenon, which explains the amount of emitted light is smaller than the amount of absorbed light, which is the Stokes' shift of light. Most of the luminescent materials are known for their downconversion properties. The energy of absorbed electromagnetic radiation is smaller than the energy of the emitted electromagnetic radiation. Besides, downconversion is very similar to this process. The absorbed electromagnetic radiation is converted to two or more photons with larger wavelengths in the downconversion process. The schematic representations of these processes are given in **Figure 1.10**.

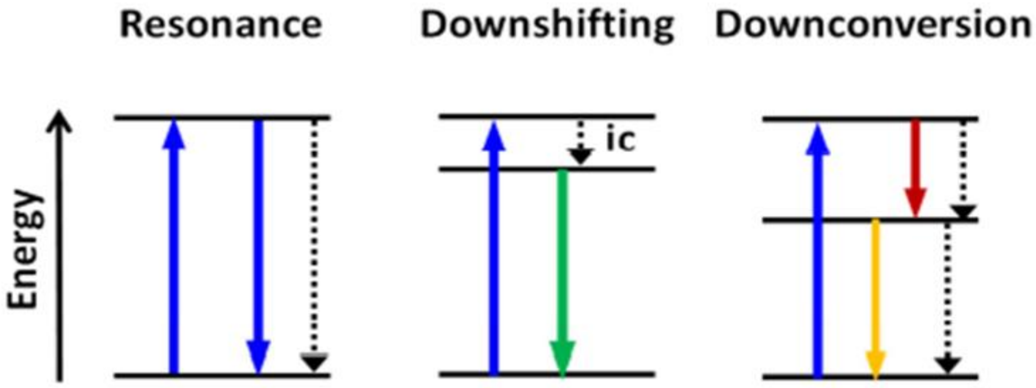

Figure 1.10. Energy diagram which describes resonance, downshifting, and downconversion (Devi, Devi, & Singh, 2020)

Most of the luminescent materials undergo downconversion. The theoretical background of the downconversion phenomenon is explained in previous sections.

1.4.4 Upconversion

Upconversion is mainly a non-linear optical process, in which the energy of the emitted light is larger than the energy of absorbed radiation. Physicist N.Bloemberg realized the approach of upconversion in 1959 to invest an infrared photon detector for counting infrared photons through the interaction of infrared photons with rare earth or transition metal incorporated in crystalline materials. (Bloembergen, 1959) There are various methods for creating upconverted photons: lanthanide-doped crystals, dye-sensitized compounds, and triplet-triplet annihilation (TTA) based compound. Unlike the lanthanide-doped crystals, the other two methods need a sensitizer, which is typically an organic-inorganic framework (mostly organometallic complex) compound. (Singh-Rachford & Castellano, 2010) The sensitizer forms a singlet state, and then this state changes to a triplet state. The energy is relocated from the excited triplet state of the sensitizer to a triplet state of the annihilator. The process, transfer of energy from the sensitizer to the annihilator, is named interface energy transfer. (Wen et al., 2019) (M. Wu et al., 2016). For TTA, during the scope of this work, these were not used for the production of upconverted photons. A schematic representation is given in **Figure 1.11**.

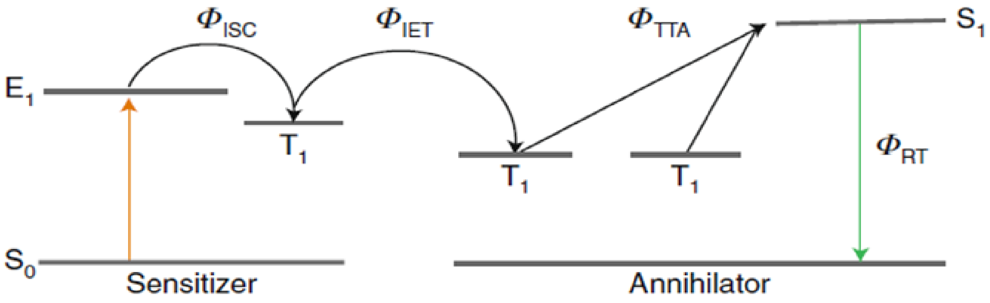

Figure 1.11. Schematic representation of TTA upconversion (ISC: intersystem crossing, IET: interface energy transfer, TTA: triplet-triplet annihilation, RT: radiative transfer) (Wen et al., 2019)

Another type of upconversion process is the dye-sensitized process. In this type of process, an organic dye is used to absorb the incident light, and then the absorbed energy is transferred from the dye to a sensitizer. (Duan, Liang, Li, Zhang, & Xu, 2018) This sensitizer transfers the energy to lanthanide-doped nanoparticles. **Figure 1.12** gives the primary mechanism for dye-sensitized upconversion.

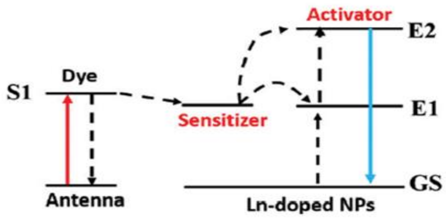

Figure 1.12. Schematic representation of dye-sensitized upconversion process (Duan et al., 2018)

After the developments in optical technologies and laser systems, the milestone experiment to detect infrared to visible upconversion was reported for the first time by F. Auzel in 1966 and clarify the energy transfer in Tm^{3+}-Yb^{3+} and Er^{3+}-Yb^{3+} systems. (Auzel, 2004)(Mahata, Hofsäss, & Vetter, 2012). After these mechanisms, the processes that will be explained. They are involved in only lanthanide-doped compounds. For upconverting lanthanide-doped compounds, there are several mechanisms. These processes are represented in **Figure 1.13**.

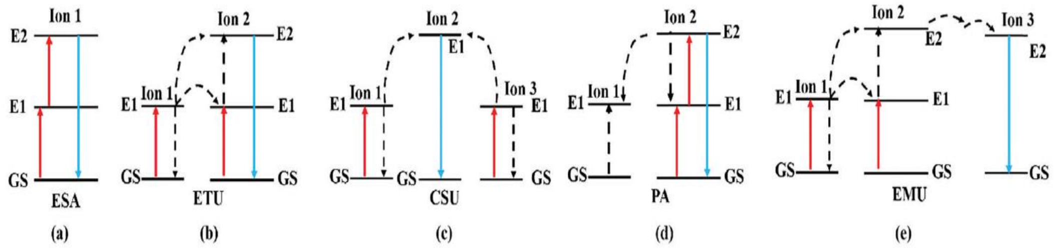

Figure 1.13. Upconversion processes for Ln-doped UCNPs. GS: ground state; E1 and E2: excited states: ESA: excited-state absorption; ETU: energy transfer upconversion; CSU: cooperative sensitization upconversion; PA: photon avalanche; EMU: energy migration upconversion(Duan et al., 2018)

The energy states of lanthanide (Ln^{3+}) ions bestow (provide) the lanthanide doped nanoparticles with significant advances for the energy transfer upconversion process. These processes are so convoluted, therefore, can be sum up as excited-state absorption (ESA), energy transfer upconversion (ETU), cooperative sensitization upconversion (CSU), photon avalanche (PA), and energy migration upconversion (EMU).

In ESA, the excitation state or emission state (E2) consists of consecutive photons through a ground state Ln^{3+} ion with convenient excitation states. As represented in **Figure 1.13(a)**, an intermediate excited state emerges after the electron's excitation. The excited electron goes through the higher excited state E2 for the upconversion of after another excitation of a second photon. Hence, emission efficiency depends on the stability of the first excited state (Duan et al., 2018). The absorption cross-section of the excited ion is essential for the second pump photon. (Mahata et al.,

2012) Currently, only a few Ln^{3+} ions, such as Er^{3+}, $Tm^{3+,}$ and Nd^{3+}, are applicable since the well-paired energy states with the energy for excitation given from the conventional lasers (975 nm and 808 nm). Even though the concentrations of dopants do not affect the ESA process's emission efficiency, the concentration of Ln^{3+} doping is commonly lower than 1% when considering the cross-relaxation of the excitation states. (Duan et al., 2018)

ETU is the most efficient way of upconversion. (J. Zhou, Liu, Feng, Sun, & Li, 2015) In this type of luminescence, a sensitizer and an activator ion are participating. Subsequent irradiation with a convenient laser, both sensitizer and activator are induced to the E1 excitation state by absorbing incident photons. Then, the sensitizer at the E1 state of the activator, coherent with the activator being excited to the E2 state for upconversion emission. The upconversion emission efficiency depends on the doping concentration (distance between sensitizer and activator) and is commonly more significant than the ESA process. Similar to ETU, CSU contains two sensitizers and one activator for the upconversion energy transfer. The activator here is excited to its E2 excitation state with energy transfer by two sensitizers at the E1 excitation state. The de-excitation of the activator from the E2 state to GS causes to release of upconversion photons. (Duan et al., 2018) There is an advantage of ETU compared to ESA, in which one pump source is needed for the ETU process. Moreover, lanthanide ion concentration has to be sufficiently high ion-ion interaction in order to generate the ETU process. (J. Zhou et al., 2015)

The PA-based process is known as much less efficient as ETU. In this type of process, all of the lanthanide dopants are induced with the energy unmatched pump photons, typically larger the energy gap between the intermediate excitation state and GS. ESA and the cross-relaxation may emerge until the energy population to an intermediate state, and then the E2 energy state of Ln^{3+} ions produces upconversion luminescence. High pump intensity and long irradiation time are necessary for this type of upconversion process. (Duan et al., 2018)

Discrepant from the process, which is explained before, EMU is most commonly detected from the core-shell lanthanide-doped UCNPs nanomaterials, where the active shell may cause higher emission efficiency. Liu first observed this upconversion process. (Wang et al., 2011) In this phenomenon, four types of luminescence pieces, namely sensitizer, accumulator, migrator, and activator with an appropriate concentration are integrated within one nanoparticle at separate layers. After the laser irradiation, the EMU process occurs at the core of the nanoparticle, followed by the systematic energy transfer from the accumulator to the activator, providing upconversion luminescence. (Duan et al., 2018)

Other types of upconverting processes of lanthanide-doped upconverting compounds are two-photon absorption (TPA) and second-harmonic generation. In TPA, the simultaneous absorption of two photons occurs without involving a real intermediary energy level. During this process, some of the energy is lost in the system. (Wang et al., 2011) In addition to TPA, SHG occurs by doubling the frequency of irradiated light without any absorption taking place. SHG is a second-order non-linear optical process in which two photons at the frequency interacting with non-centrosymmetric media combine to form a new photon with the doubled frequency. (Wang et al., 2011) (Pantazis, Maloney, Wu, & Fraser, 2010)

Moreover, the time response from SHG is shorter than the one for TPA. The schematic representation of both processes given in **Figure 1.14**. (Pantazis et al., 2010)

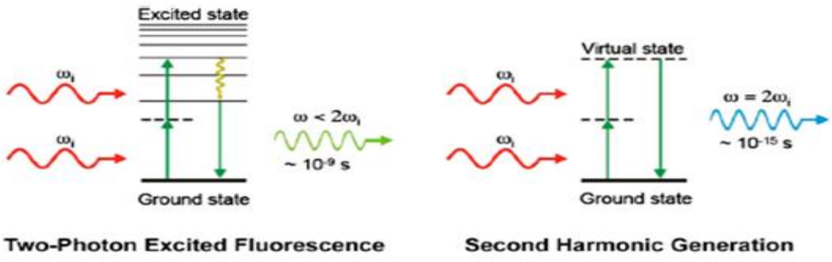

Figure 1.14. The schematic representations of (a) two-photon absorption and (b) second-harmonic generation (Pantazis et al., 2010)

1.5 Host Materials

Host compounds have to be thermally and chemically stable to tolerate high temperatures and maintain their luminescent properties. As long as no energy transfer occurs from the host material to the dopant, transparent host matrices are chosen for the emission processes. (Shang, Li, & Lin, 2014) Crystalline and amorphous compounds may be utilized for this purpose. There is a wide range of host matrices, which are studied for the production of rare-earth-based luminescent compounds. These are silicates(Lu, Li, & Wang, 2013), phosphates (J. Wu et al., 2017), tungstate(Ambast, Kunti, Som, & Sharma, 2013), borates, etc. For instance, in a study made by Mahata et al., a vanadate structure (YVO_4) structure is used as a host material, and the dopant is Ho^{3+} ion. (Mahata, Koppe, Hofsäss, Kumar, & Vetter, 2015) Also, phosphates are appropriate as a host material in technology and high thermal stability. Therefore, they are chosen in many studies such as $KMgLa(PO_4)$: Dy^{3+}(Z. Yang et al., 2016), $SrGdNa(PO_4)_3F$: Dy^{3+}(Han, Sun, & Sun, 2016)

1.5.1 Borates as Host Materials

Rare earth metal borates such as $GdBO_3$, YBO_3, and $LaBO_3$ are auspicious candidates for luminescence due to high luminous efficiency, exceptional thermal stability, and substantial absorption in the range of vacuum ultraviolet (VUV) to ultraviolet (UV). (C. H. Yang, Pan, & Zhang, 2007) Mostly, the synthesis of borate compounds is at a lower temperature, and they are very durable at high temperatures as phosphates and tungstates are considered. If the luminescent properties of borate crystals are regarded, these compounds may be applied in display panels (Velchuri et al., 2011), light-emitting diodes (LED), lasers (Arun Kumar & Dhanasekaran, 2011), etc. Levin et al. studied lanthanide orthoborates ($LnBO_3$) in 1961. The study reported that depending on the type of the rare earth metal ion, lanthanide orthoborates ($LnBO_3$) crystallizes in the three different forms of calcium carbonate ($CaCO_3$), which are vaterite, aragonite, and calcite. (LEVIN, ROTH, & MARTIN, 1961)There are five most common structures for classification of the crystals based on $CaCO_3$ structure, which are the hexagonal vaterite type with P63/m space group, the orthorhombic aragonite type with Pnma space group, the rhombohedral vaterite type with R32 space group, and rhombohedral calcite type with R3c space group, and monoclinic pseuowollastonite type with C2/c space group. (Pitscheider, Kaindl, Oeckler, & Huppertz, 2011)

1.6 Structural Properties of $GdBO_3$

As a beginning, it is essential to consider the crystal structure of $GdBO_3$. $GdBO_3$ has mainly two crystal structures. These structures interchange between each other according to the temperature of the crystal. Therefore, they are named as Low-Temperature phase and High-Temperature phase. The temperature, which $GdBO_3$ transforms from Low Temperature to High-Temperature phase, is about 836 ℃ and the reverse transformation occurs at about 546 ℃.

Low Temperature (LT) crystal structure is considered hexagonal and similar to the crystal structure of YBO_3. The edge lengths of this structure are a=3.770 Å and c=8.804 Å. However, this is a misassignment of the structure since, in X-Ray Diffraction patterns, there have to be peaks at approximately 15°; however, boron atom is so much small and may not reflect the X-Ray beam. Yet, the difference between hexagonal and rhombohedral cell is explained as $a_r=\sqrt{3}a_h$ and $c_r=3c_h$ In LT structure, the unit cell is described as rhombohedral because the Chadeyron model is used for the description of boron and oxygen groups in the structure. (Ren et al., 1999) According to this model, boron and oxygen groups create a $B_3O_9^{9-}$ group, and Rare Earth ion are at the center of this structure. (Chadeyron, El-Ghozzi, Mahiou, Arbus, & Cousseins, 1997) The structure is given in **Figure 1.15**.

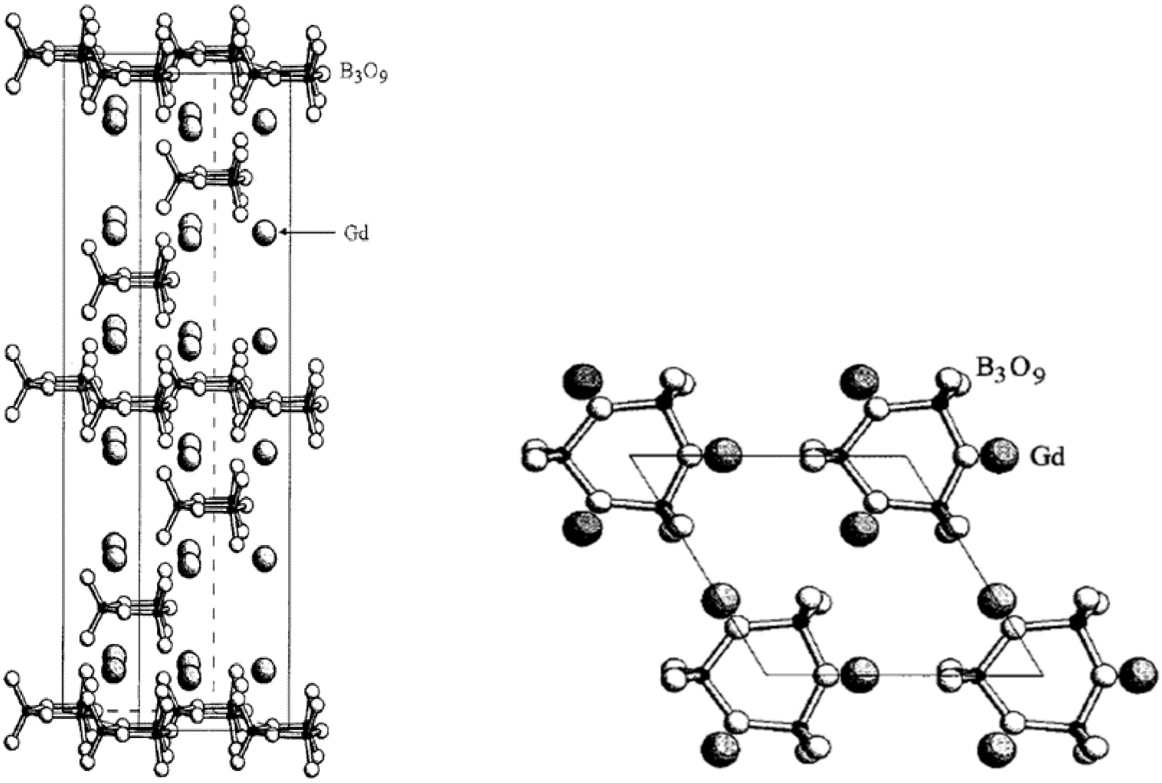

Figure 1.15. Low-Temperature crystal structure of $GdBO_3$ and $B_3O_9^{9-}$ sheets in the structure (Ren et al., 1999)

Nonetheless, *High Temperature (HT) crystal structure* is different from *Low-Temperature crystal structure*. The High-Temperature crystal structure in the hexagonal space group P63/mmc with the lattice constants of a=4.110(4) and c=8.579-(4). High-temperature measurement was taken at 700°C. In this structure, the $B_3O_9^{9-}$ units are converted to planar BO_3^{3-} units. A representation is given in **Figure 1.16**. (Ren et al., 1999)

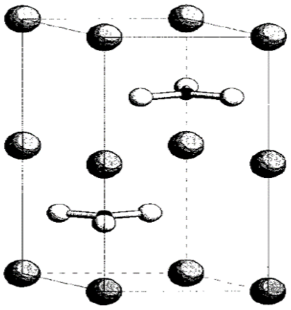

Figure 1.16. High-Temperature crystal structure of $GdBO_3$ (Ren et al., 1999)

In the given structure, planar BO_3^{3-} groups are placed perpendicular to the c axis of the structure and forming an anion sheet. It is the arrangement of BO_3^{3-} groups that provide the expansion of the a-axis and the extraction of the c-axis during the phase transition. The gadolinium atoms exist in between these sheets and are coordinated in a trigonal antiprismatic polyhedron. It is obvious that the borate groups change from $B_3O_9^{9-}$ to BO_3^{3-}; however, the positions of gadolinium ions remain the same. The arrangement of the boron and oxygen atoms, as well as B-O bond breakage and formation. (Ren et al., 1999) In addition, there is three rhombohedral structure, which consists of one triclinic and one monoclinic form. If gadolinium ion coordination is considered, both types have gadolinium ions, which are surrounded by eight oxygen ions. (Nair, Nigam, Sudarsan, Rao, et al., 2018) The lattice parameters of them are given in **Figure 1.17**.

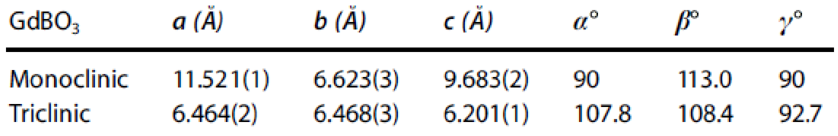

$GdBO_3$	*a (Ă)*	*b (Ă)*	*c (Ă)*	*α°*	*β°*	*γ°*
Monoclinic	11.521(1)	6.623(3)	9.683(2)	90	113.0	90
Triclinic	6.464(2)	6.468(3)	6.201(1)	107.8	108.4	92.7

Figure 1.17. Lattice parameters of monoclinic and triclinic forms of $GdBO_3$ obtained from Rietveld Refinement (Nair et al., 2018)

Moreover, according to a more recent study of Seyyidoğlu, it has $R3_2$ space group and rhombohedral structure. (SEYYİDOĞLU, 2009) The parameter that defines the structure and representation of the $GdBO_3$ structure are given in the following **Table 1.14** and **Figure 1.18**.

Table 1.3 Crystal data and structure refinement (SEYYİDOĞLU, 2009)

Empirical formula	$GdBO_3$
Molar Mass	216.1 g/mol
Crystal System	Rhombohedral
Space Group	$R3_2$
Unit Cell Dimensions	a=6.63899(8)Å
	c=26.7219(5)Å
Volume	1020.00
2 Theta Range	0-150°
R_{wp}	0.0454
R_p	0.0320

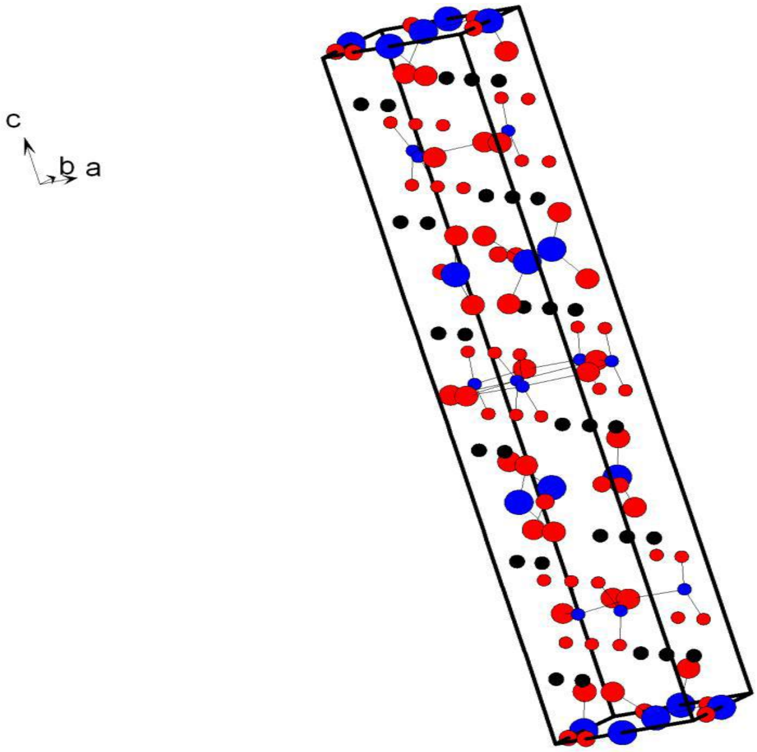

Figure 1.18. Representation of the crystal structure of $GdBO_3$ (black ones are Gd^{3+}, blue ones are B^{3+} and red ones are O^{2-} ions) (SEYYİDOĞLU, 2009)

Nair et al. state that this differentiation may be made using both XRD measurement and IR measurement. For XRD measurement, different peaks exist in the patterns, and for IR measurements, there are various bands for both of the structures. In **Figure 1.19**, it is obviously seen that different types of bonding and different structural properties occur.

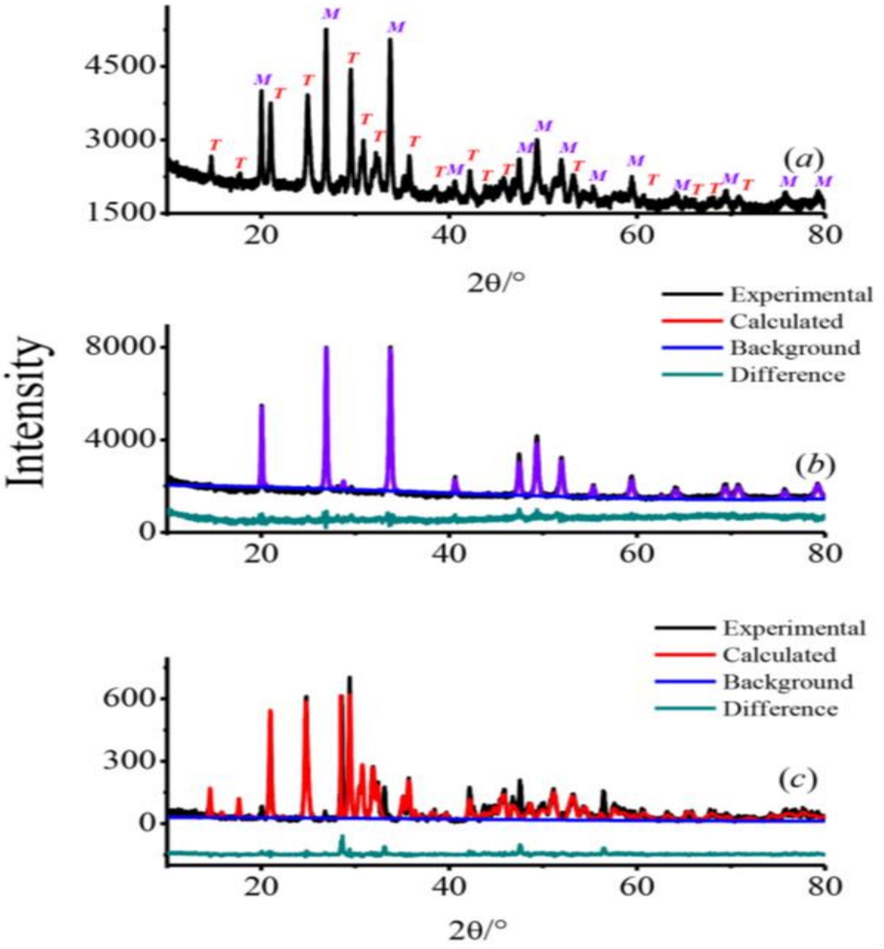

Figure 1.19. (a) is the experimental resulting of synthesized $GdBO_3$ by hydrothermal method and then annealed at 800 °C, (b) is single-phase monoclinic $GdBO_3$, and (c) is a single-phase triclinic $GdBO_3$ synthesized by polyol method annealed at 800 °C by polyol method. (The markers T and M in the first one show peaks corresponding to the triclinic and monoclinic forms of $GdBO_3$)(Nair, Nigam, Sudarsan, Rao, et al., 2018)

In the XRD patterns, the first one shows the synthesized $GdBO_3$ by the hydrothermal method. In this pattern, it is obviously seen that the peaks of both of the structures can be seen, and because of the different arrangements of atoms, they have very different patterns. The second and the last ones are given to indicate the separated patterns of monoclinic and triclinic structure. The second one belongs to the monoclinic structure of $GdBO_3$, and the last one belongs to the triclinic structure of $GdBO_3$. There are calculated, experimental background and difference between them in the patters, given if there exist. In addition, if the IR measurement is considered, indicated differences are found in the analyses. In the same study, IR peaks are given separately in **Figure 1.20**.

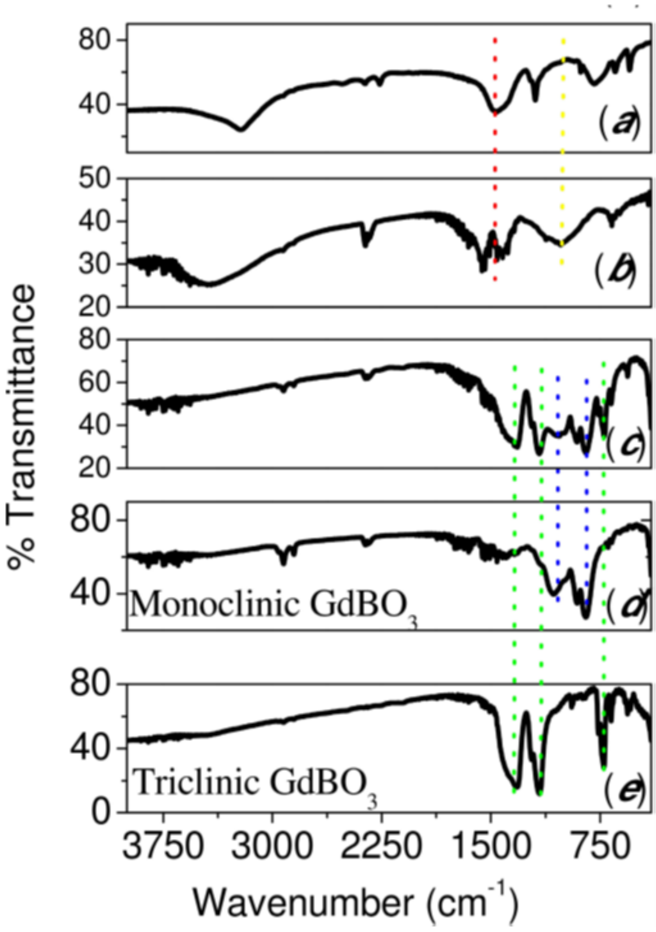

Figure 1.20. FTIR measurements of (a) boric acid (b) as prepared sample obtained by hydrothermal method, (c) as prepared sample subjected to annealing at 400 °C, (d) single-phase monoclinic $GdBO_3$, and (e) single-phase triclinic $GdBO_3$

These spectra show boric acid, $GdBO_3$ prepared by hydrothermal method, annealed at 400 °C, single-phase monoclinic $GdBO_3$ and single-phase triclinic $GdBO_3$. As seen in the figures, the monoclinic and triclinic phases show different peaks from their spectra. The peaks around 852, 912, and 1073 cm^{-1} are used to characterize single-phase monoclinic $GdBO_3$. The peaks around 1166 and 1317 cm^{-1} are used for the characterization of single-phase triclinic $GdBO_3$.(Nair, Nigam, Sudarsan, Rao, et al., 2018) Based on the other studies, the peak around 1073 cm^{-1} is related to terminal B-O stretching vibration of $B_3O_9^{9-}$ rings, and the stretching modes of B-O linkages in the ring appear around 912 and 852 cm^{-1}. (Kubasiewicz, Runowski, Lis, & Szczeszak, 2015) (Szczeszak, Grzyb, Lis, & Wiglusz, 2012)

1.7 Luminescent Properties of Rare Earth Metal Ions

Rare earth metals involve 15 lanthanide elements with an atomic number from 57 to 71. Lanthanides are transition metals, which are in the 4f-block and sixth period of the periodic table, as well as scandium (its atomic number is 21) and yttrium (its atomic number is 39). These elements have several application areas, which are computers, plasma displays with their emission in UV, visible and near-IR ranges. Besides, their color purity and luminescent yield, great Stokes' shift, narrowband emission, and long-lasting luminescent decay lifetimes make them very popular for many fields. Moreover, they have 5s and 5p orbitals, and they shield the fourth shell of these metals. This permits 4f orbitals not to be affected by the surroundings or lattice electronic environment. (Dieke, Crosswhite, & Dunn, 1961) Both number of electrons and electronic configurations in 4 f shell are given in **Figure 1.21**

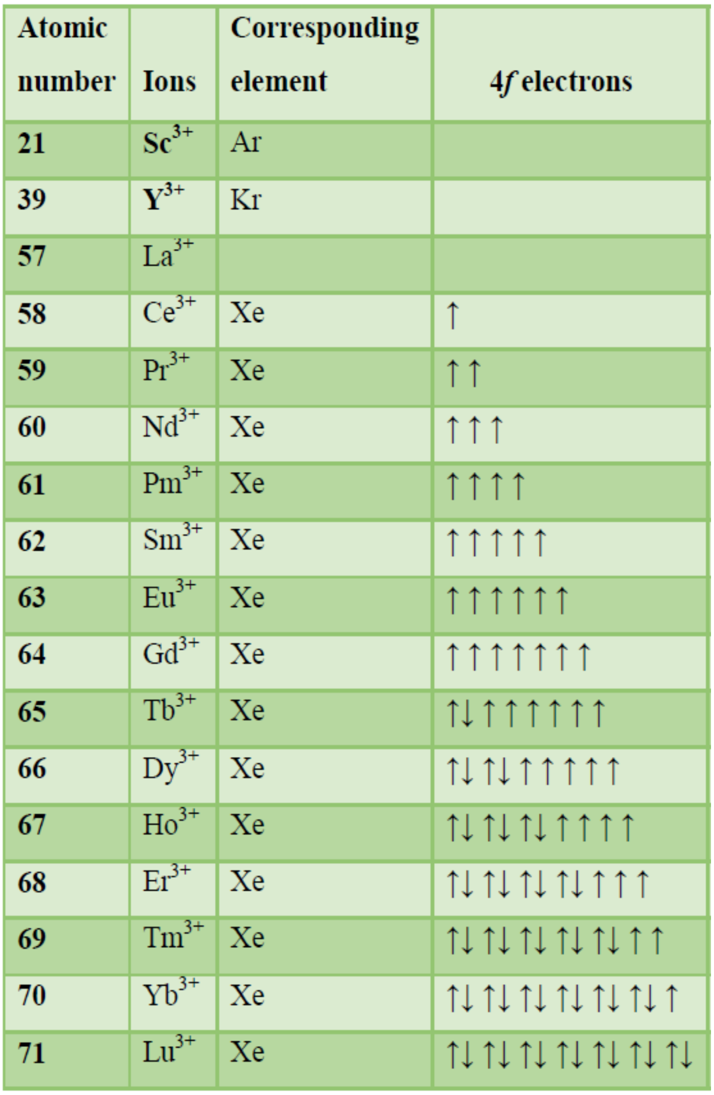

Atomic number	Ions	Corresponding element	4*f* electrons
21	Sc^{3+}	Ar	
39	Y^{3+}	Kr	
57	La^{3+}		
58	Ce^{3+}	Xe	↑
59	Pr^{3+}	Xe	↑ ↑
60	Nd^{3+}	Xe	↑ ↑ ↑
61	Pm^{3+}	Xe	↑ ↑ ↑ ↑
62	Sm^{3+}	Xe	↑ ↑ ↑ ↑ ↑
63	Eu^{3+}	Xe	↑ ↑ ↑ ↑ ↑ ↑
64	Gd^{3+}	Xe	↑ ↑ ↑ ↑ ↑ ↑ ↑
65	Tb^{3+}	Xe	↑↓ ↑ ↑ ↑ ↑ ↑ ↑
66	Dy^{3+}	Xe	↑↓ ↑↓ ↑ ↑ ↑ ↑ ↑
67	Ho^{3+}	Xe	↑↓ ↑↓ ↑↓ ↑ ↑ ↑ ↑
68	Er^{3+}	Xe	↑↓ ↑↓ ↑↓ ↑↓ ↑ ↑ ↑
69	Tm^{3+}	Xe	↑↓ ↑↓ ↑↓ ↑↓ ↑↓ ↑ ↑
70	Yb^{3+}	Xe	↑↓ ↑↓ ↑↓ ↑↓ ↑↓ ↑↓ ↑
71	Lu^{3+}	Xe	↑↓ ↑↓ ↑↓ ↑↓ ↑↓ ↑↓ ↑↓

Figure 1.21. Electronic configurations of Rare Earth Metal ions

1.7.1 The electronic Energy States

For luminescence of rare earth metal ions, the electrons are found in the states, which are called energy states. They are described as spin angular momentum number (S), the orbital angular momentum number (L), and total angular momentum number (J). It is well known that electrons have a spin, and the value of that can be +1/2 or -1/2. Summing up them will give the total spin angular momentum number, which is S. L is the total value of the azimuthal quantum number (l) of the electron-found orbitals, and The total angular momentum number, J, is the summation of L and S. For ground state, S has to be its maximum value. Optical transitions occur in these states. The rules specified for 4f orbitals trivalent ions in $LaCl_3$ crystal. Dieke (Sorokina, 2003) arranges these states, and this diagram is given (**Figure 1.22**).

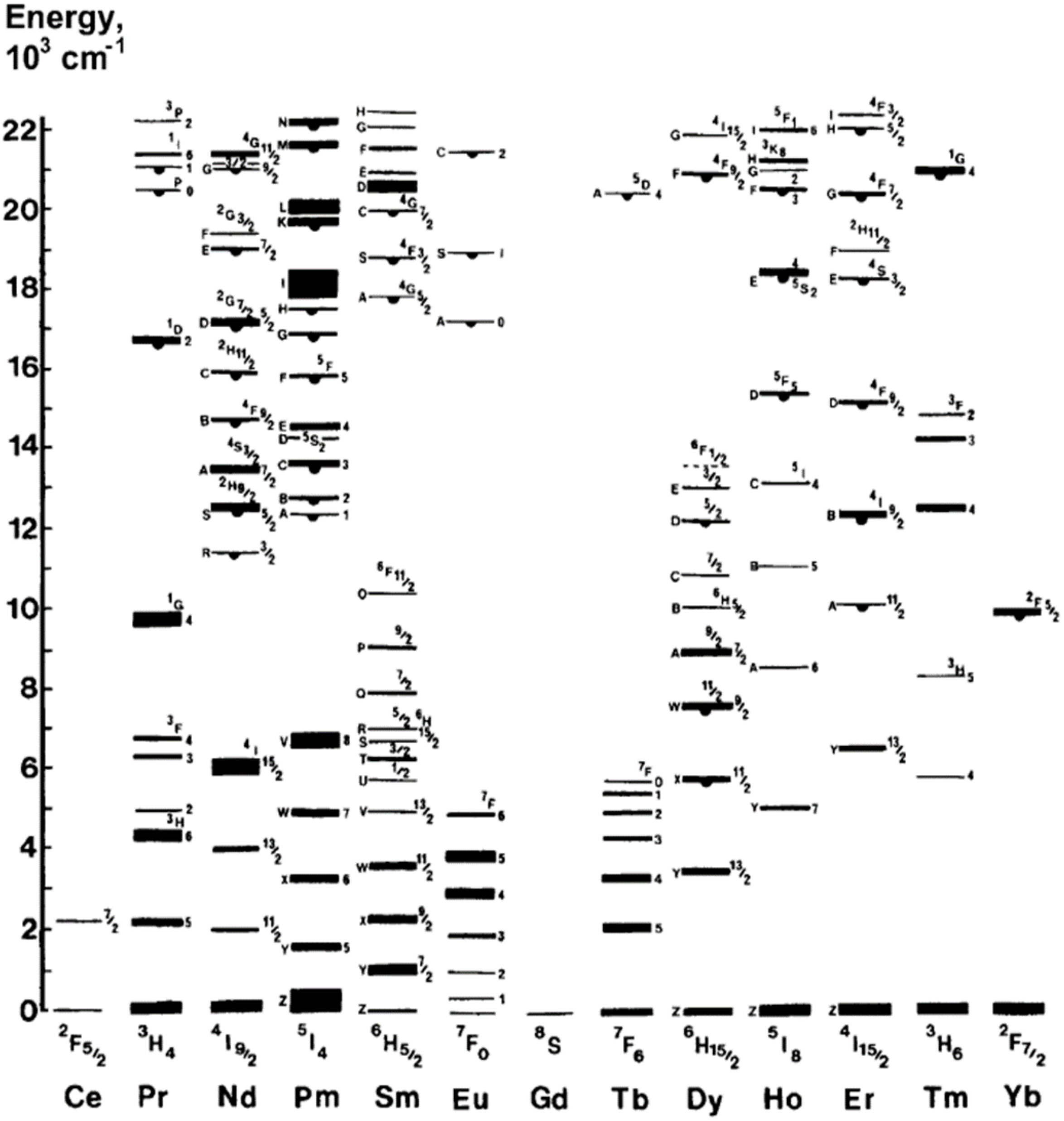

Figure 1.22. Dieke diagram (rare-earth ions in $LaCl_3$) (Sorokina, 2003)

1.7.2 Photoluminescent Properties of Dysprosium (III) (Dy^{3+}) Ion

Among other rare earth metal ions, Dy^{3+} has potential for applications, including white light. Dy^{3+} ion has an emission spectrum with both blue $^4F_{9/2} \rightarrow {}^6H_{15/2}$ band transition and yellow $^4F_{9/2} \rightarrow {}^6H_{13/2}$ band transition. The $^4F_{9/2} \rightarrow {}^6H_{15/2}$ transition, which is associated with magnetic dipole transition, is not affected by its lattice environment; on the other hand, $^4F_{9/2} \rightarrow {}^6H_{13/2}$ transition which emerges due to the electric dipole transitions, can be easily changed by surroundings since they are not parity allowed. The second transition is allowed when Dy^{3+} ions associate with the low symmetry site. (Hussin, Hamdan, Halim, & Husin, 2010) Commonly a white light region is observed from the CIE 1931 diagram from the overlap of blue and yellow regions. In addition, the intensity ratio of yellow to blue can be designated by changing the concentration of rare-earth ion, glass composition, and excitation wavelengths. (Kesavulu & Jayasankar, 2011)(Zulfiqar Ali Ahamed, Madhukar Reddy, & Deva Prasad Raju, 2013)

There are so many studies about Dy^{3+} doped phosphors literature. For instance, in a survey of N.Wazir et al., the emission bands of Dy^{3+} doped lithium calcium borate ae observed as 490, 578, 674 nm with the excitation at 349 nm. In this study, the emission Dy^{3+} in the yellow region is higher than the one in the blue region. Therefore, it is reported that Dy^{3+} may choose the low symmetry site because of the similar radius size of Dy^{3+} and Ca^{2+} in the host matrix. Also, the ratio of the intensity of yellow to blue is used to observe the host material of rare-earth ions. The decrease or increase of the yellow to blue indicates the changes in surroundings. (Neharika et al., 2016)

Another example is the study of Grobelna et al. is gadolinium tungstate, and the most intense peak is around 575 nm, which is the region of yellow emission. (Grobelna, Synak, & Bojarski, 2012) This study shows two intense peaks around 575 nm and 485 nm and a weak peak around 662 nm. These peaks are assigned due to the transitions from $^4F_{9/2}$ to $^6H_{15/2}$ (blue), $^6H_{13/2}$ (yellow), and $^6H_{11/2}$. (**Figure 1.23**)

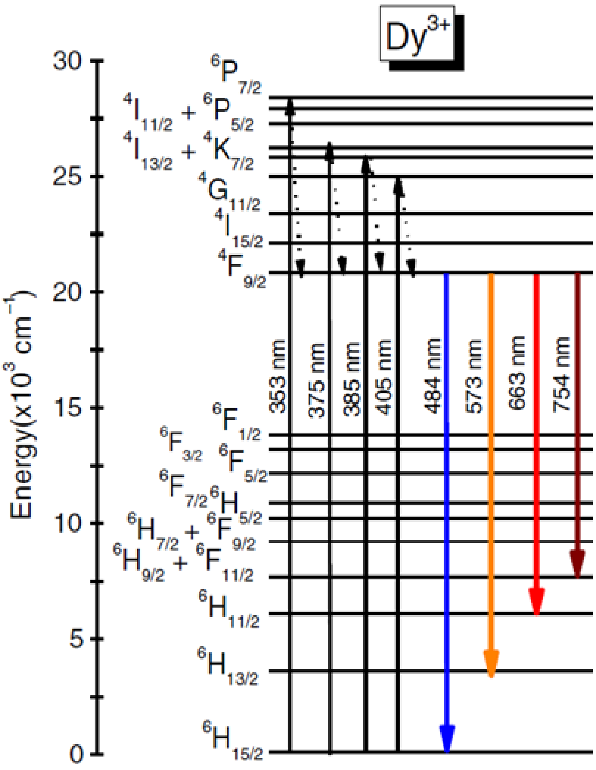

Figure 1.23. Emission wavelengths of Dy^{3+} ion (Alves et al., 2016)

1.7.3 Photoluminescent Properties of Cerium (III) (Ce^{3+}) Ion

From all other rare earth metal ions, Ce^{3+} ions have the lowest 4f to 5d transition energy. On the other hand, the energy difference between 5d^1 state and the closest $^2F_{7/2}$ state is consistently large enough for efficient light emission. Host matrices affect the excited energy levels of Ce^{3+} ions with the help of crystal field splitting of 5d orbitals. Therefore, the energy of the emitted photon is directly related to the structure of the host compounds. (Shang et al., 2014) One of the studies by C.H. Yang indicates that the emission of Ce^{3+} doped phosphors upon 328 nm excitation and for the emission, broadband is centered in the vicinity of 400 nm is according to the transition of 5d$\rightarrow{}^2F_J$ (J=5/2,7/2). The excitation and the emission of the compound are given in spectra (**Figure 1.24**).

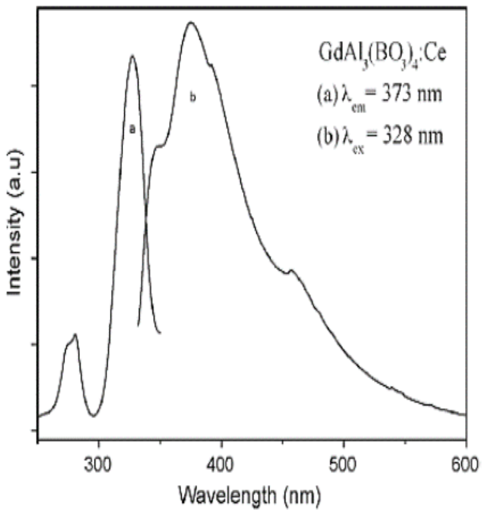

Figure 1.24. Excitation and the emission spectra of Ce^{3+} ions (C. H. Yang, Y. X. Pan and Q. Y. Zhang, 2007.)

In another study by Pauwels et al., the absorption spectrum of the compound shows two broad bands centered at 313 and 355 nm refers to the Ce^{3+} 4f→5d transitions and the emission from these excitation wavelengths is broadband peaking at 380 nm, also in this broadband there is a slight shoulder at 415 nm. The reason why the absorption spectrum is peaking at these values is the crystallographic site, which is a distorted octahedron; thus, it is likely that the 5d levels are divided by the crystal field interaction into two components, e_g and t_{2g}. The peaks in the emission spectrum are referred to as the transitions from the lowest 5d level of the Ce^{3+} ions to the spin-orbit split $^2F_{7/2}$ and $^2F_{5/2}$ levels. The energy difference between the levels $^2F_{7/2}$ and $^2F_{5/2}$ is 2200 cm^{-1}. In addition, a fluorescence excitation spectrum is taken to indicate the two separate excitation wavelengths. The resulting absorption and emission spectra and fluorescence spectrum (under 400 nm emission wavelength) in this study is given in **Figure 1.25** and **1.26**. (Pauwels et al., 2000)

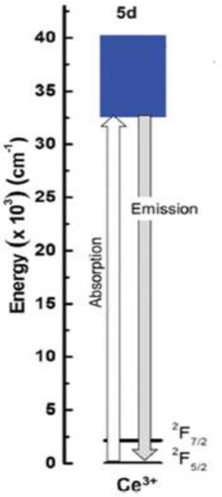

Figure 1.25. Energy level diagram of Ce^{3+} ion (Shrivastava et al., 2017)

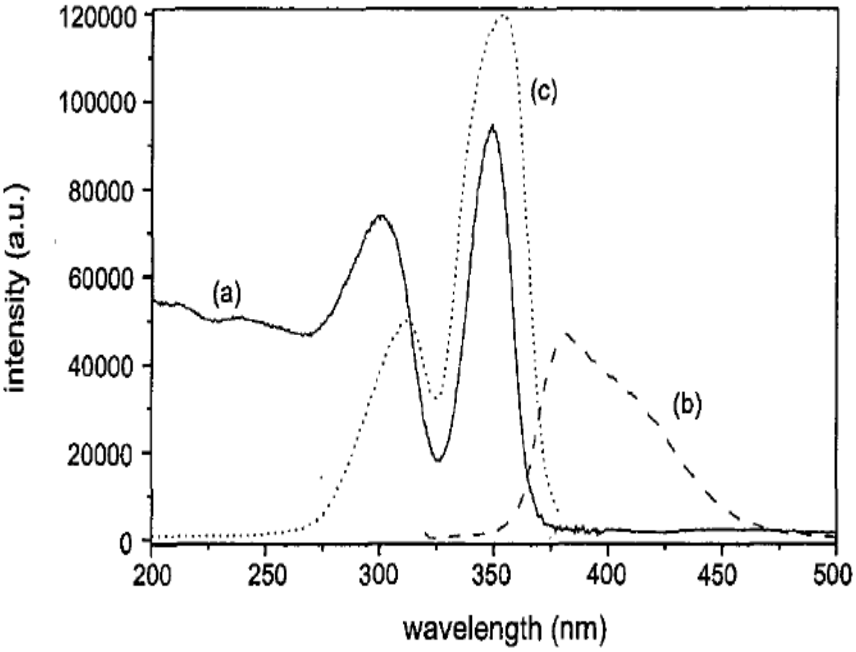

Figure 1.26. Optical characteristics of $Lu_2Si_2O_7$:Ce single crystals: (a) absorption spectrum, (b) emission spectrum, (c) fluorescence excitation spectrum (under 400 nm wavelength)(Pauwels et al., 2000)

1.7.4 Photoluminescent Properties of Europium (III) (Eu^{3+}) Ion

Luminescence properties of Eu^{3+} doped phosphors with various host compounds have been studied for their deep red emissions. Eu^{3+} doped compounds have a wide range of applications, such as plasma display panels, quantum cutting solar cells, bioimaging, solid-state light displays, etc.

In a study by R.G. Nair et al., Eu^{3+} doped phosphors show frequent emissions that result from $^5D_0 \rightarrow {}^7F_1$ (592 nm), $^5D_0 \rightarrow {}^7F_2$ (615 nm) and $^5D_0 \rightarrow {}^7F_4$ (700 nm) transitions, respectively. The first two transitions are purely magnetic and electric dipole allowed. The ratio of $^5D_0 \rightarrow {}^7F_2$ to $^5D_0 \rightarrow {}^7F_1$ transition, which is known as the asymmetric ratio of luminescence, is a sensitive parameter that depends on the extent of the distortion in the local environment around Eu^{3+} ions in a lattice. Higher the asymmetric ratio, the greater will be the extent of the deformity. (Nair, Nigam, Sudarsan, & Rao, 2018)

In another study by G. Jia et al., phosphors doped with Eu^{3+} ion mainly emit light with the wavelengths of 578, 590, 614, 652, and 701 nm, which are from the transitions $^5D_0 \rightarrow {}^7F_J$ (J is varied from 0 to 4). In this study, the host material is $LaBO_3$. It is indicated that the emission band around 590-600 nm is resulted from the magnetic dipole transition $^5D_0 \rightarrow {}^7F_1$ is found as tolerant of the changes in the surroundings of the activator ion. On the other hand, the emission resulting from the electric dipole $^5D_0 \rightarrow {}^7F_2$ transition near 510-630 nm is sensitive to the changes in the environment around the Eu^{3+} ion (**Figure 1.27**). (Jia et al., 2012)

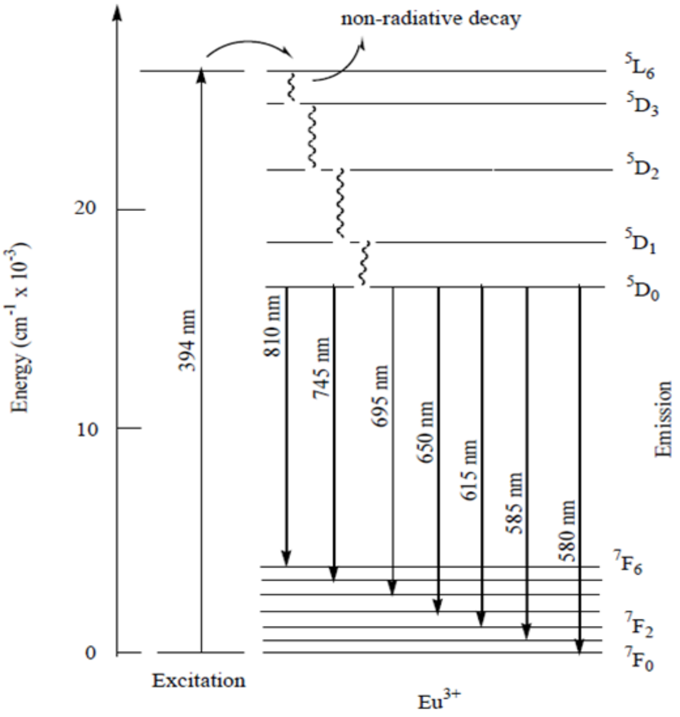

Figure 1.27. Energy level diagram of Eu^{3+} (Nassar et al., 2009)

1.7.5 Photoluminescent Properties of Terbium (III) (Tb^{3+}) Ion

Terbium is the most commonly used ions among the rare earth metals due to the efficient optical properties. Tb^{3+} activated phosphors are used in optical technologies such as plasma display panels(L. Y. Zhou, Wei, Shi, Gong, & Liang, 2008), ultraviolet radiation sensors(Zmojda, Kochanowicz, Miluski, & Dorosz, 2014), mercury-free and fluorescent lamps(Potdevin, Chadeyron, Boyer, Caillier, & Mahiou, 2005). Tb^{3+} has a 4f^8 electronic configuration. It shows a strong clear-cut green emission (545 nm) due to the transition $^5D_4 \rightarrow ^7F_5$ and the Tb^{3+}.(Jung, Kim, & Kang, 2004) Moreover, there are weaker bands in the emission spectrum, which are resulted from the transitions from $^5D_4$ to ^7F_J (J=6,4,3) at the wavelength of 486, 583, and 620 nm. (Song, Guo, & You, 2011) The intensity ratio of blue to green region depends on the host material in two ways. Firstly, the ratio is affected by the phonon induced relaxation resulting from the maximum phonon energy—

higher the maximum phonon energy, the lower the ratio—secondly, the ratio affected by the relative position of the energy levels of $4f^75d^1$ and $4f^8$. An electron is excited to $4f^75d^1$ may drop directly to the $^5D_4$ level, and it ignores the $^5D_3$ and, in the end, produces $^5D_4$ luminescence only.

In a study with $LaBO_3$ in which the ratio of the doped Tb^{3+} is changed in 2.5, 5.7, 10 mole percent, the maximum absorption wavelength was found at 378 nm. In this study, the emission wavelength was kept at 543 nm. (**Figure 1.28**)

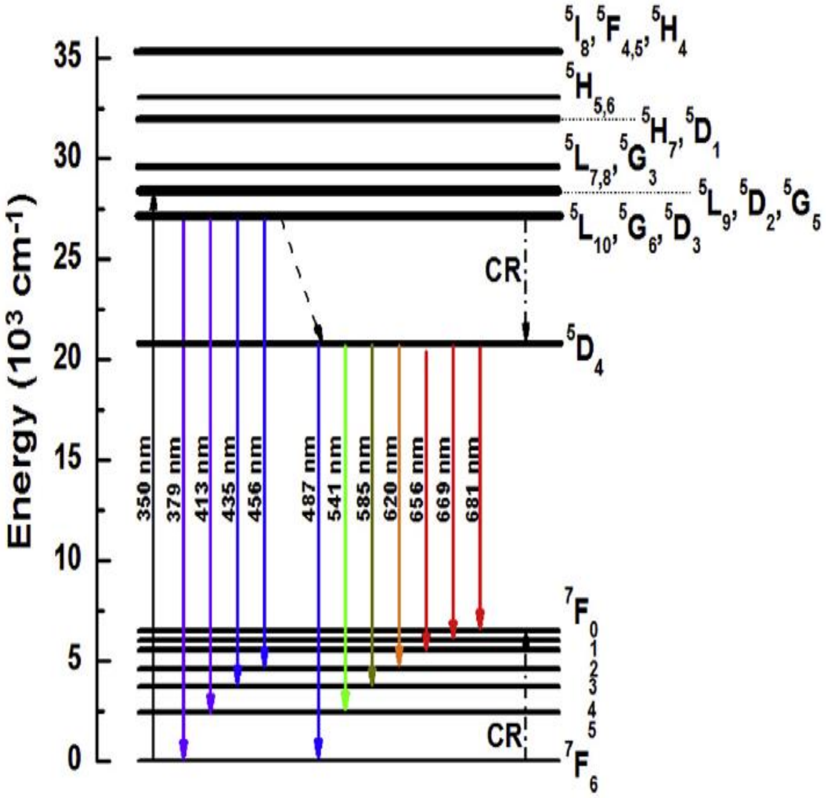

Figure 1.28. Energy level diagram of Terbium ion (Juárez-Batalla, Meza-Rocha, Muñoz, Camarillo, & Caldiño, 2016)

1.7.6 Photoluminescent Properties of Ytterbium (III) (Yb^{3+}) Ion

Some of the rare-earth ions are different from others in terms of luminescence properties. Most of the rare-earth ions emit radiation with a wavelength of larger than the absorbed radiation. However, some of the rare-earth ions such as Yb^{3+} may emit radiation with a wavelength of smaller than the absorbed one. This phenomenon, which is named up-conversion, was explained in the previous chapter. There are various fields of application for these types of materials, such as bio-imaging(J. C. Zhou et al., 2011) (Nyk, Kumar, Ohulchanskyy, Bergey, & Prasad, 2008), targeted drug delivery(Tian et al., 2015), display technologies(Wang et al., 2010), solar cells(Trupke, Shalav, Richards, Würfel, & Green, 2006), etc. Most commonly, the duty of Yb^{3+} ions is absorbing the electromagnetic radiation, and absorbed energy is usually transferred to the activator. Yb^{3+} has an energy band gap of 10^4 cm^{-1}(Prasad, Rao, Gupta, & Prakash, 2018), and this corresponds to 980 nm in terms of wavelength. (**Figure 1.29**)

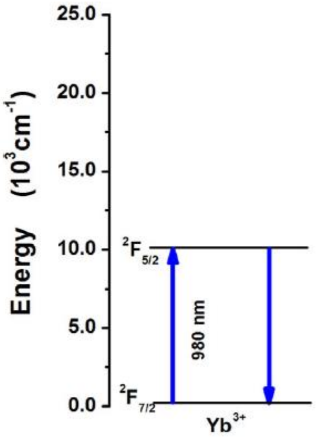

Figure 1.29. Energy state diagram of Yb^{3+} ion (Sun et al., 2014)

In a study by Zhou et al., Tm^{3+} is used as a sensitizer, Yb^{3+}/Tm^{3+} doped compound excited with a 975-nm laser, and then Yb^{3+} transfers its energy toTm^{3+}. The emission spectrum only involves the characteristic emission bands of Tm^{3+} centered at 479, 648, and 800 nm. (Nyk et al., 2008) Another study made by Sun et al., Yb^{3+}, is used for the sensitization of Er^{3+} ion in gadolinium tungstate crystal. Two emission peaks are observed at 370 nm and 520 nm, which are the characteristic lines of Er^{3+} ion. (Sun et al., 2014) On the other hand, Yb^{3+} can be an activator by using its second harmonic generation and cooperative emission property. In a study of Amami et al., Yb^{3+} in $BaTiO_3$ can emit radiation with an excitation wavelength of 938 nm. (Amami et al., 2007) The resulting spectra are shown in **Figure 1.30**.

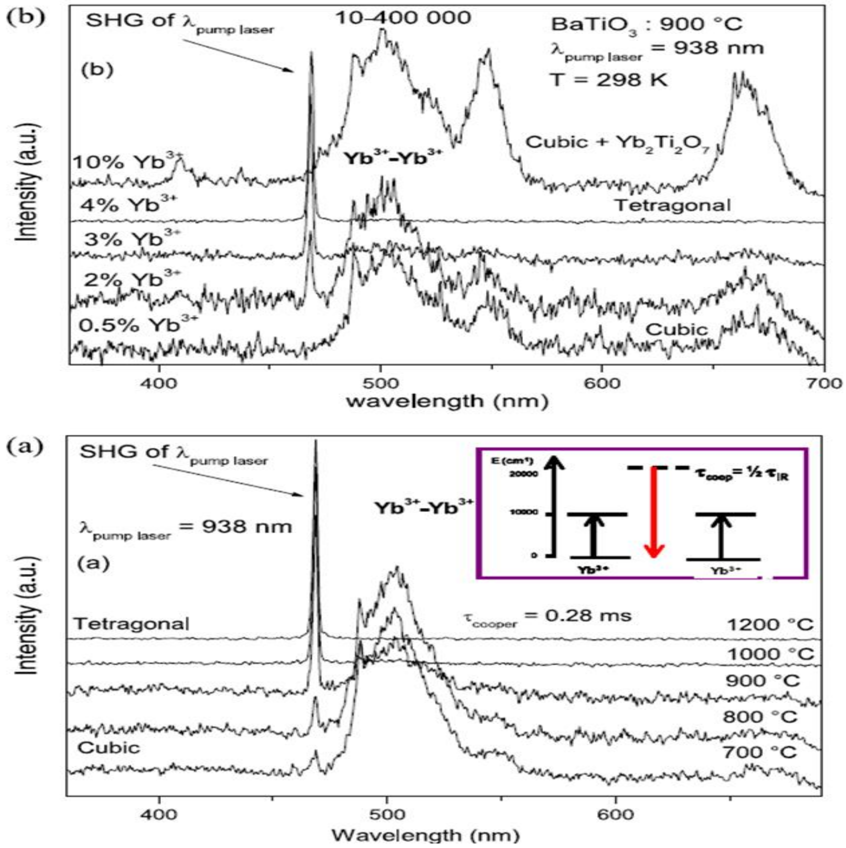

Figure 1.30. Second Harmonic Generation (SGH) signal, the upconversion emission spectrum of rare earth impurities under Yb^{3+} under pumping in the IR and visible cooperative emission spectrum of Yb^{3+} ion pairs at room temperature of (a) 1% Yb^{3+}-doped $BaTiO_3$ nano-crystals heated at different temperatures, (b) $BaTiO_3$ nanocrystals prepared at 900 °C and doped with varying concentrations of Yb^{3+}. (Amami et al., 2007)

In addition to this property, Yb^{3+} can emit radiation by using its downconversion property. This property is mostly used for the utilization of c Si-based solar cells. Yb^{3+} can emit light by sensitization of Ce^{3+} in a study of Fang et al. In this study, yttrium aluminum garnet ($Y_2Al_5O_{12}$ or YAG) doped Yb^{3+} and Ce^{3+} and emission lines of Yb^{3+} can be obtained strongest at 1030 nm and the weaker ones at 942, 970, 1008 nm. (Fang et al., 2014) The spectra of changing the Yb^{3+} ion concentration of compounds are shown in the spectra (**Figure 1.31**).

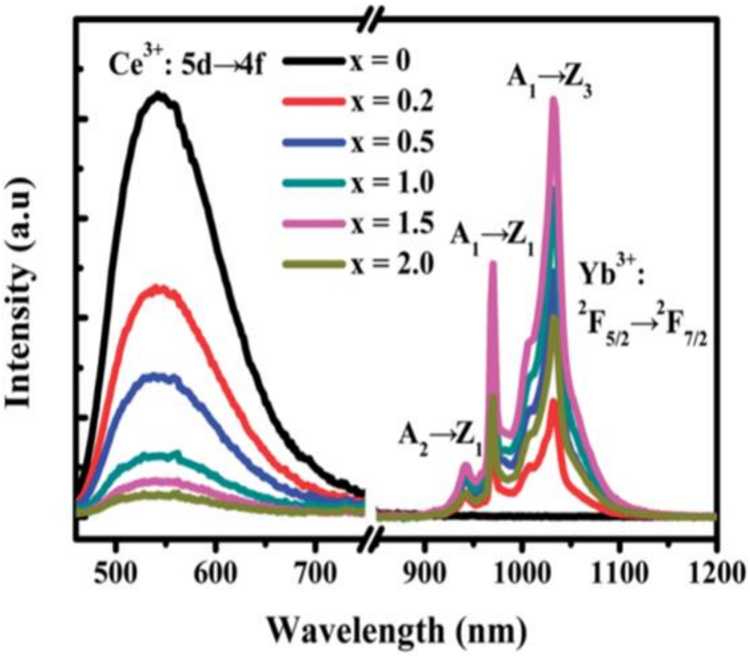

Figure 1.31. Concentration-dependent emission spectra of 0.1 Ce^{3+}-xYb^{3+} codoped glass ceramics (x=0-2.0) (Fang et al., 2014)

1.8 Photoluminescence Decay Lifetime

Luminescence can be characterized by a) luminescence intensity as a function of wavelength, b) quantum yield that is explained in the next section, c) decay lifetime (Berezin & Achilefu, 2011). Decay lifetime measurement is a part of the luminescence studies. Lifetimes of samples are examined by exciting them with the radiation, which has short pulse ranges, for instance, from femtosecond to nanosecond according to materials. Simply, the time consumed during the emission is measured after the excitation. Each emission line may have different decay times, which are affected by the environment of the ion. (Shyichuk, 2015) Decay lifetime is commonly thought as a kinetic parameter and is found as being inversely proportional to the sum of the rate constants of the radiative process k_r and non-radiative process k_{nr}, collectively known as quenching.

$$\tau = \frac{1}{k_f + k_{nr}}$$

The examined decay lifetimes are mathematically equal to the average lifetime during the molecule is excited. This equation is based on which the decay rate equation is first order. (Berezin & Achilefu, 2011) Obtained decay curves of phosphors may fit to single exponential decay equation, which involves initial intensity (I_0) at the time t=0, the luminescence at the time t (I_t), and the decay lifetime (τ). Nonetheless, some of the decay curves may be required to fit by double exponential decay equation. (Abacı, 2017)

Single exponential function for decay time

$$I(t) = I_0 e^{-t/\tau}$$

Double exponential function for decay time

$$I(t) = I_0 e^{-t/\tau_1} + I_0 e^{-t/\tau_2} \qquad \text{so} \qquad \tau = \frac{I_1\tau_1^2 + I_2\tau_2^2}{I_1\tau_1 + I_2\tau_2}$$

In general, single exponential functions are mostly used for the radiative transition of two levels. If the emission lines are produced by the activator ions, measured lifetimes would base on the coordination geometry of these ions. In other words, different lifetimes may be obtained with varied geometries of ions. Therefore, the number of coordination sites of the activators may be disclosed by the quantity of the exponential fit. (Abacı, 2017) (Hızal Abacı, Mete, Esenturk, & Yılmaz, 2019) The decay lifetime is a comparable long-lasting process; therefore, luminescent materials may undergo several processes such as electronic redistribution or reorganization of surroundings. In many cases, the energy gained as a consequence of photon absorption is consumed because of non-radiative processes, collectively called quenching, and inevitably causes a decrease of the decay lifetime. Quenching in the processes is not avoidable, hence the empirical decay lifetime is les than the natural decay lifetime. (Berezin & Achilefu, 2011)

1.9 Quantum Efficiency

Luminescent compound converts the exposed energy into photons, and this process is not efficient as it is expected since several losses emerging resulted from alternative deactivation paths. Therefore, there are two concepts to clarify this efficiency. These are quantum yield and quantum (energy) efficiency. (Devi et al., 2020)Quantum efficiency is about the amount of absorbed energy and emitted energy. The quantum efficiency may be represented mathematically as in below.

$$\eta = \frac{\text{energy output}}{\text{energy input}}$$

Contrary to the quantum efficiency, the quantum yield is the ratio of the excited molecule to the total of the molecules. (Valeur & Berberan-Santos, 2012)

1.10 Chromaticity Coordinates (CIE)

Color is an approach, and as such, it is not available to engineering analysis. However, there has to be a standard for measurement and examination, and CIE is an accepted observer for these measurements. Thus, CIE colorimetry is the metric of the psychophysical color stimulus.

The light sensation is produced by electromagnetic radiation within the wavelength range of 380 nm and 780 nm. The range is not apparent, and the definite limits are dependent on the adaptation state of the eye and the light stimuli surrounding the test object.

Two methods are used for the production of color stimuli, which are additive and subtractive methods. In the additive method, it is thought that the color sensation is produced by mixing the colors three primary colors, which are red, green, and blue. These are found on spots that are so close to each other; however, they are not resolved by the human eye. In addition, different colors may be produced by changing the intensities of primary colors. On the other hand, in the subtractive method, colorants remove some parts of the visible spectrum. Superposing several colorants of different concentrations on each other will change the color of the transmitted light.

For the simplicity of the concept, the additive method is used for colorimetry. In the current approach, there are three empirical rules of additive method:

- Three separate variables are essential and sufficient for the determination of color.
- For an additive mixture of the color stimuli, only their tristimulus values are relevant, not their spectral positions.
- In additive mixtures of color stimuli, when one or more than one piece of the mixture is gradually changed; likewise, the occurred tristimulus values change progressively.

Since these are experimental rules, there are more necessary specifications such as foveal vision (eyesight), field size (2° or 10°)(the field size of 2° represents a diameter of about 1.7 cm at a viewing distance of 50 cm), and color matching functions, which are determined by averaging the results of a large number of observers.

For the sake unit, $x+y+z=1$ and therefore, the equations for x, y, and z are given below.

$$x = \frac{X}{X+Y+Z}$$
$$y = \frac{Y}{X+Y+Z}$$
$$z = \frac{Z}{X+Y+Z}$$

Therefore, the total of the diagram is given below with some specific wavelengths.

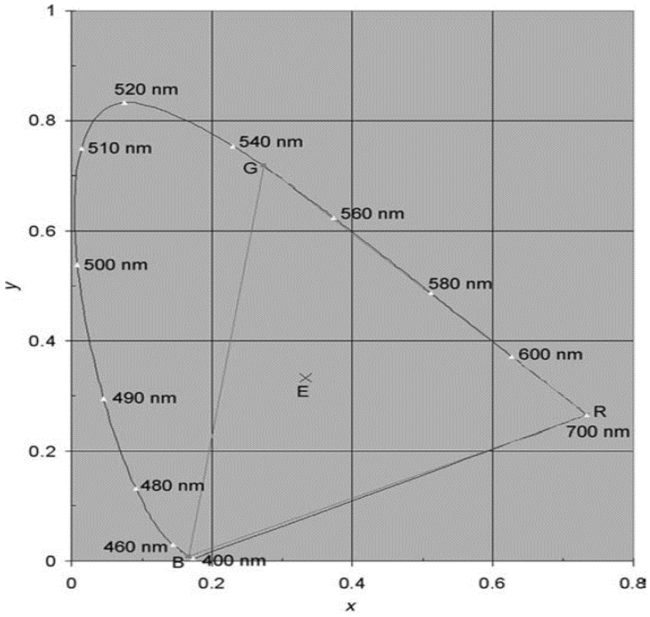

Figure 1.32. x, y chromaticity diagram of the CIE 1931 trichromatic system. The triangle shown refers to the R, G, B primaries put to use to define the CIE trichromatic system.

For this standard observer, red is at 700 nm, green is at 546.1 nm, and blue is at 435.8 nm (**Figure 1.34**). (Scanda, 2007)

1.11 Aim of the Study

In previous studies made by our group, optical properties of Ce^{3+}, Dy^{3+}, Tb^{3+} single doped and codoped $GdBO_3$ with the microwave-assisted solid-state method and Ce^{3+}, Tb^{3+} single doped and codoped $GdBO_3$ with the sol-gel method were investigated. This study aims to examine the effect of the third dopant with different dopant materials and concentrations on the optical properties of $GdBO_3$ crystal. The third dopants were chosen as Eu^{3+} for Ce^{3+}/Dy^{3+} codoped $GdBO_3$ and Yb^{3+} for Ce^{3+}/Tb^{3+} codoped $GdBO_3$. Therefore, the intensity of specific ions will be increased. For the first part of the study, an increase in the intensity of various characterization techniques has been used to examine to explain crystal structure, luminescence properties, colors, and luminescence lifetimes.

CHAPTER 2

MATERIALS AND METHODS

2.1 Materials

Table 2.1 Molecular weights, intended purposes, and labels of the materials

Materials	Molecular Weights	Intended Purposes	Labels
Gd_2O_3	362.5 g/mole	$GdBO_3$ production	Acros Organics
Dy_2O_3	373.0 g/mole	Doping agent	Aldrich 99.9%
$Ce_2(CO_3)_3.xH_2O$	460.27 g/mole	Doping agent	Aldrich 99.9%
Eu_2O_3	351.926 g/mole	Doping agent	Aldrich 99.9%
Tb_4O_7	747.69 g/mole	Doping agent	Aldrich 99.9%
Yb_2O_3	394.09 g/mole	Doping agent	Aldrich 99.9%
HNO_3	63.013 g/mole	Nitritization of metals	Merck 65% (d=1.39 g/mL)
H_3BO_3	61.83 g/mole	Borate source	Merck
EDTA ($K_2C_{10}H_{14}N_2O_8$)	368.4g/mole	Capping agent	Merck
PEG-PPG-PEG ($(C_3H_6O.C_2H_4O)_x$)	5800 g/mole	Surfactant	Sigma Aldrich

2.2 Synthesis Method

All of $Dy_xGd_{1-x}BO_3$, $Ce_yGd_{1-y}BO_3$, $Eu_zGd_{1-z}BO_3$, $Dy_xCe_yGd_{1-x-y}BO_3$, $Dy_xCe_yEu_zGd_{1-x-y-z}BO_3$, and $YbzGd_{1-z}BO_3$ and $Tb_xCe_yYb_zGd_{1-x-y-z}BO_3$ particles were synthesized by using Pechini sol-gel method. Stoichiometric amounts of Gd_2O_3, Dy_2O_3, $Ce_2(CO_3)_3.xH_2O$, Eu_2O_3, Tb_4O_7, and Yb_2O_3 were dissolved in nitric acid and heated to evaporated all extra acid. The resulting rare earth metal salts were dissolved in a sufficient amount of deionized water. In a different beaker, boric acid, EDTA, and PEG solution were prepared. Nitrate salt solutions of rare earth ions were added to this solution dropwise with continuous stirring. This mixture was heated to 80 °C until a homogeneous gel forms. This resulting gel was calcinated for 3 hours. Finally, the white powder of doped $GdBO_3$ occurred. The stoichiometric amounts of precursor compounds are given in **Figure 2.1**. (For all of the samples, there are identical amounts of PEG, EDTA, H_3NO_3, and H_3BO_3.)

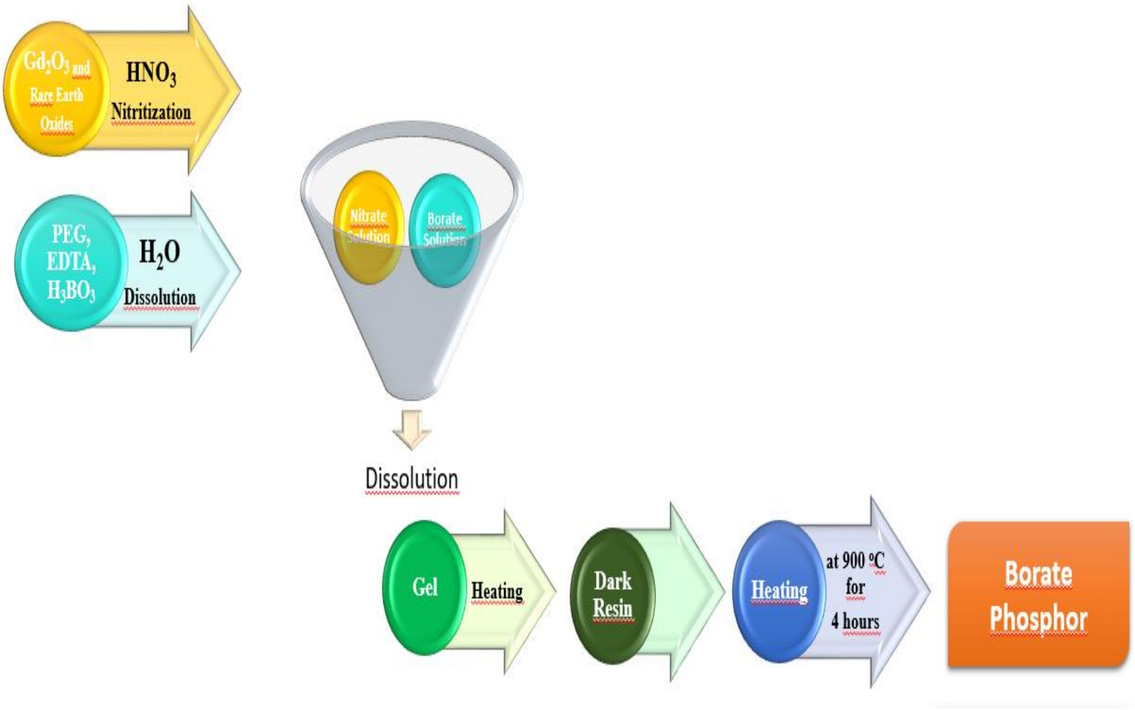

Figure 2.1. Schematic representation of the sol-gel method

For $Dy_xCe_yEu_zGd_{1-x-y-z}BO_3$,

Table 2.2 The stoichiometric amounts of PEG, EDTA, H_3NO_3, and H_3BO_3

PEG	EDTA	H_3NO_3	H_3BO_3
2.68g	0.172g	8mL	0.572g

Table 2.3 Stoichiometric amounts of Gd_2O_3 and Dy_2O_3 for the synthesis of Dy^{3+} doped $GdBO_3$

	Gd_2O_3	Dy_2O_3
$GdBO_3$	1.68g	
$Dy_{0.01}Gd_{0.99}BO_3$	1.66g	0.02g
$Dy_{0.03}Gd_{0.97}BO_3$	1.63g	0.05g
$Dy_{0.05}Gd_{0.95}BO_3$	1.59g	0.09g
$Dy_{0.07}Gd_{0.93}BO_3$	1.56g	0.12g

Table 2.4 Stoichiometric amounts of Gd_2O_3 and $Ce_2(CO_3)_3$ for the synthesis of Ce^{3+} doped $GdBO_3$

	Gd_2O_3	$Ce_2(CO_3)_3$
$GdBO_3$	1.68g	
$Ce_{0.01}Gd_{0.99}BO_3$	1.66g	0.02g
$Ce_{0.03}Gd_{0.97}BO_3$	1.63g	0.06g
$Ce_{0.05}Gd_{0.95}BO_3$	1.59g	0.11g
$Ce_{0.07}Gd_{0.93}BO_3$	1.56g	0.15g

Table 2.5 Stoichiometric amounts of Gd_2O_3 and Eu_2O_3 for the synthesis of Eu^{3+} doped $GdBO_3$

	Gd_2O_3	Eu_2O_3
$GdBO_3$	1.68g	
$Eu_{0.01}Gd_{0.99}BO_3$	1.66g	0.02g
$Eu_{0.03}Gd_{0.97}BO_3$	1.63g	0.05g
$Eu_{0.05}Gd_{0.95}BO_3$	1.59g	0.08g
$Eu_{0.07}Gd_{0.93}BO_3$	1.56g	0.11g
$Eu_{0.10}Gd_{0.90}BO_3$	1.51g	0.16g
$Eu_{0.20}Gd_{0.80}BO_3$	1.30g	0.32g

Table 2.6 Stoichiometric amounts of Gd_2O_3, Dy_2O_3 and $Ce_2(CO_3)_3$ for the synthesis of Dy^{3+}/Ce^{3+} doped $GdBO_3$

	Gd_2O_3	Dy_2O_3	$Ce_2(CO_3)_3$
$GdBO_3$	1.68g		
$Dy_{0.01}Ce_{0.01}Gd_{0.99}BO_3$	1.64g	0.02g	0.02g
$Dy_{0.03}Ce_{0.01}Gd_{0.96}BO_3$	1.61g	0.05g	0.02g
$Dy_{0.05}Ce_{0.01}Gd_{0.94}BO_3$	1.58g	0.09g	0.02g
$Dy_{0.07}Ce_{0.01}Gd_{0.92}BO_3$	1.54g	0.12g	0.02g
$Dy_{0.01}Ce_{0.03}Gd_{0.96}BO_3$	1.61g	0.02g	0.06g
$Dy_{0.03}Ce_{0.03}Gd_{0.94}BO_3$	1.58g	0.05g	0.06g
$Dy_{0.05}Ce_{0.03}Gd_{0.92}BO_3$	1.54g	0.09g	0.06g
$Dy_{0.07}Ce_{0.03}Gd_{0.90}BO_3$	1.51g	0.12g	0.06g
$Dy_{0.01}Ce_{0.05}Gd_{0.94}BO_3$	1.58g	0.02g	0.09g
$Dy_{0.03}Ce_{0.05}Gd_{0.92}BO_3$	1.54g	0.05g	0.09g
$Dy_{0.05}Ce_{0.05}Gd_{0.90}BO_3$	1.51g	0.09g	0.09g
$Dy_{0.07}Ce_{0.05}Gd_{0.88}BO_3$	1.48g	0.12g	0.09g

Table 2.7 Stoichiometric amounts of Gd_2O_3, Dy_2O_3, $Ce_2(CO_3)_3$ and Eu_2O_3 for the synthesis of $Dy^{3+}/Ce^{3+}/Eu^{3+}$ doped $GdBO_3$

	Gd_2O_3	Dy_2O_3	$Ce_2(CO_3)_3$	Eu_2O_3
$GdBO_3$	1.68g			
$Dy_{0.01}Ce_{0.03}Eu_{0.01}Gd_{0.95}BO_3$	1.59g	0.02g	0.06g	0.02g
$Dy_{0.03}Ce_{0.03}Eu_{0.01}Gd_{0.93}BO_3$	1.61g	0.05g	0.06g	0.02g
$Dy_{0.01}Ce_{0.03}Eu_{0.03}Gd_{0.94}BO_3$	1.56g	0.02g	0.06g	0.05g
$Dy_{0.03}Ce_{0.03}Eu_{0.03}Gd_{0.91}BO_3$	1.53g	0.05g	0.06g	0.05g
$Dy_{0.01}Ce_{0.03}Eu_{0.05}Gd_{0.91}BO_3$	1.53g	0.02g	0.06g	0.08g
$Dy_{0.03}Ce_{0.03}Eu_{0.05}Gd_{0.89}BO_3$	1.49g	0.05g	0.06g	0.08g
$Dy_{0.01}Ce_{0.03}Eu_{0.07}Gd_{0.89}BO_3$	1.49g	0.02g	0.06g	0.11g
$Dy_{0.03}Ce_{0.03}Eu_{0.07}Gd_{0.87}BO_3$	1.46g	0.05g	0.06g	0.11g
$Dy_{0.01}Ce_{0.03}Eu_{0.10}Gd_{0.86}BO_3$	1.44g	0.02g	0.06g	0.16g

Table 2.8 Stoichiometric amounts of Gd_2O_3, Tb_4O_7, $Ce_2(CO_3)_3$ and Yb_2O_3 for the synthesis of Tb^{3+}/Ce^{3+}/Yb^{3+} doped $GdBO_3$

	Gd_2O_3	Tb_4O_7	$Ce_2(CO_3)_3$	Yb_2O_3
$GdBO_3$	1.68g			
$Tb_{0.05}Ce_{0.05}Yb_{0.05}Gd_{0.85}BO_3$	1.66g	0.04g	0.11g	0.04g
$Tb_{0.05}Ce_{0.05}Yb_{0.10}Gd_{0.80}BO_3$	1.63g	0.04g	0.11g	0.09g
$Tb_{0.05}Ce_{0.05}Yb_{0.15}Gd_{0.75}BO_3$	1.59g	0.04g	0.11g	0.14g
$Tb_{0.05}Ce_{0.05}Yb_{0.20}Gd_{0.70}BO_3$	1.56g	0.04g	0.11g	0.18g

2.3 Instrumentation

2.3.1 Furnace

Protherm Furnace PLF-130-6, with the capability of heating, up to 1300 ℃, was used for the annealing process of materials

2.3.2 Powder X-Ray Diffractometer (XRD)

X-ray diffraction is the most reliable method for identifying the crystal structures of materials. Powder XRD instruments investigated the crystal structures of produced borate phosphors. Rigaku Minifles X-Ray Diffractometer with CuKα (30 kV, 15 mA, λ=1.54051 Å) source was used. The range of 2theta degree was set between 5^o and 90^o. The scanning speed was 2^o per minute. The resolution of scanning was set to 0.01. The diffraction pattern of gadolinium borate was obtained from the International Centre for Diffraction Database (ICDD) with card number 13-0483.

2.3.3 Fourier Transform Infrared (FTIR) Spectrometer

FTIR spectra of produced materials were recorded with Bruker IFS 66/S spectrometer collected with ZnSe crystal at an incident angle of 45^o. The spectra ware obtained between 4000-550 cm^{-1} with a resolution of 4 cm^{-1}.

2.3.4 Photoluminescence Spectrometer

Varian Cary Eclipse Fluorescence Spectrometer was used for the investigation of photoluminescence properties of materials. Measurements were carried on powder form of samples with solid sample holder equipment of the instrument. The position of the sample holder was set for optimum signal collection. Emission spectra were collected in the range of 400-700 nm with 100 nm per minute scanning speed. Both excitation and emission were arranged to 5 nm for most of the samples. Moreover, a 240-395 nm bandpass filter was used as an excitation filter, and a 430-1100 nm bandpass filter was used as an emission filter.

2.3.5 SEM Images

SEM images were taken in METU Central Laboratory. The instrument is QUANTA 400F Field Emission SEM, and it is a high-resolution microscope with 1.2 nm resolution.

2.3.6 Luminescence Lifetime Measurement

Luminescence lifetimes were recorded with a hand-made instrument available in the Physics Department of METU (Prof. Dr. Enver Bulur, P212). The device was equipped with a UV-365 pulsed LED (Prismatix model blcc-02) that was coupled with fiber. A monochromator (Newport-78025), a photomultiplier tube (Oriel-70680), and Scott (GG420) long-pass filter with 3mm thickness and 25 mm radius were utilized for data collection. A multichannel scaler (Stanford Research Systems SR430) recorded decay curves. Measurements were made with pellets of pure compounds.

2.3.7 Quantum Efficiency Measurement

Quantum efficiency measurements were made with handmade instrument. The source of the instrument is a 365-nm light source with fiber optics. The detector is used with an integrating sphere.

CHAPTER 3

RESULTS AND DISCUSSION

In this part of the study, X-Ray diffraction patterns, FTIR spectra, photoluminescence measurements, decay lifetimes, quantum yields, and lastly, SEM images will be discussed in two types of the triple doped compound were examined in this study; all of the sections split into two parts.

3.1 X-Ray Diffraction (XRD) Patterns

In this part of the study, XRD patterns were used for the determination of different phases if there existed. Also, the (h k l) values of pure $GdBO_3$ in the JCPDS card 13-0483. For each of the sets, different $GdBO_3$ were synthesized for random error.

3.1.1 XRD Patterns of $Dy_xCe_yEu_zGd_{1-x-y-z}BO_3$

To determine the crystal structure of single doped and co-doped whether the crystal structure is compatible with pure $GdBO_3$ structure, XRD patterns were examined, and they are matched with pure the pattern of pure $GdBO_3$ phosphor. Moreover, some patterns are given for the other peaks in patterns in order to be compared. $CeBO_3$ is not provided since this compound is observed with particular conditions. Since there was so much boric acid in the sol-gel synthesis method (1:2 ratios in terms of mole fraction), it was not considered remaining Dy_2O_3 and Gd_2O_3. In addition, each (h k l) values are assigned if they were matched with the pure compound.

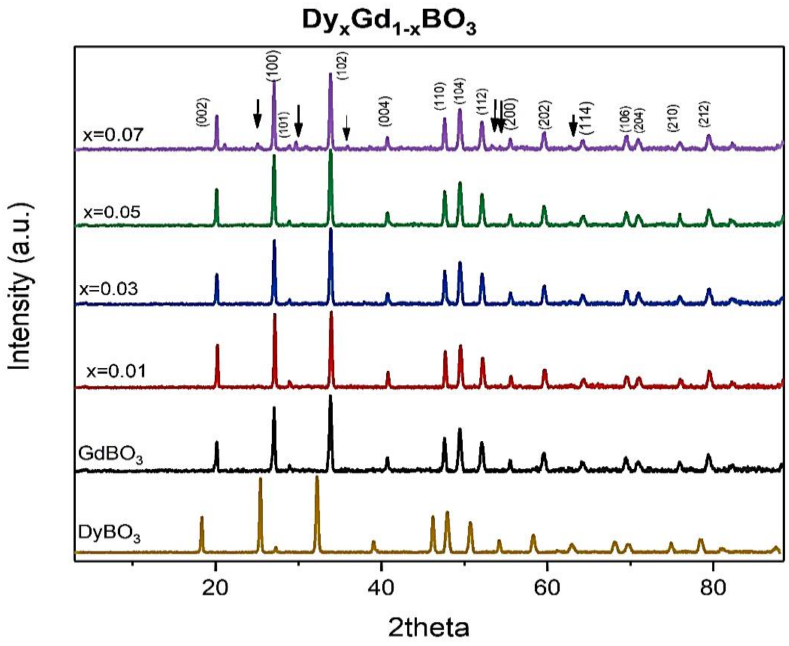

Figure 3.1. XRD patterns of Dy^{3+} doped $GdBO_3$ (x for Dy^{3+})

As it is seen in **Figure 3.1**, doping Dy^{3+} and changing the concentration of dopant were affecting the crystal structure of $GdBO_3$. Only peaks at approximately 64 degrees and 21 degrees (2 theta) are seen in all of the patterns, but the other unknown peaks are seen only in the highest concentration of Dy^{3+} doping. They can be mostly about $DyBO_3$, Dy_2O_3, or Gd_2O_3. Besides, for identification, $DyBO_3$ synthesized by our group was used; however, the crystal structure of $DyBO_3$ and $GdBO_3$ are the same, and they only differ by means of unit cell parameters of their crystal structures. Moreover, the extra peaks in 7 percent doped $GdBO_3$ did not fit with $DyBO_3$ pattern.

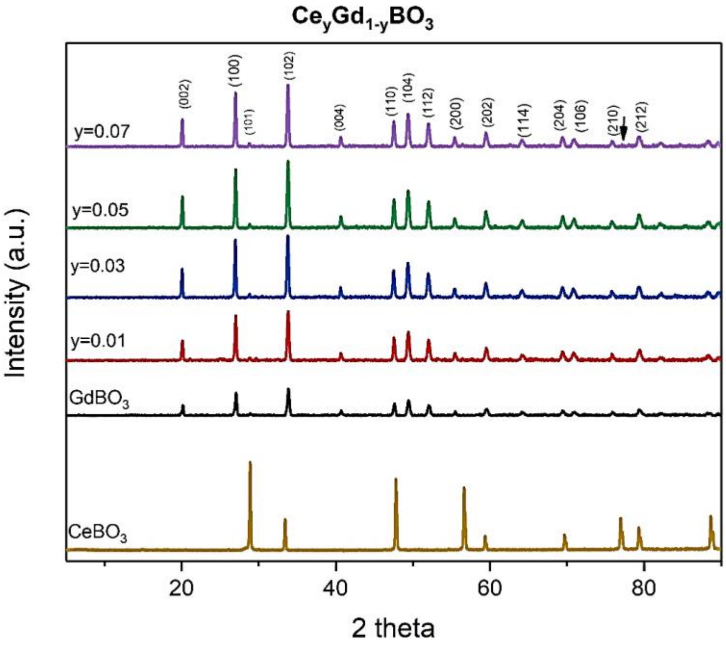

Figure 3.2. XRD patterns of Ce^{3+} doped $GdBO_3$ (y for Ce^{3+})

With these patterns in **Figure 3.2**, it was examined the effect of doping Ce^{3+} in $GdBO_3$ and changing the concentration of dopant on the crystal structure of the compound. The patterns of the pure compound and doped phosphors were inspected in case of the presence of different phases, and they are the same. XRD pattern of $CeBO_3$ synthesized by our group, and there was no substantial evidence of the existence of these crystals. Since the excess amount of H_3BO_3 was used for the production of doped and undoped $GdBO_3$, oxide precursors were not in the resulting product.

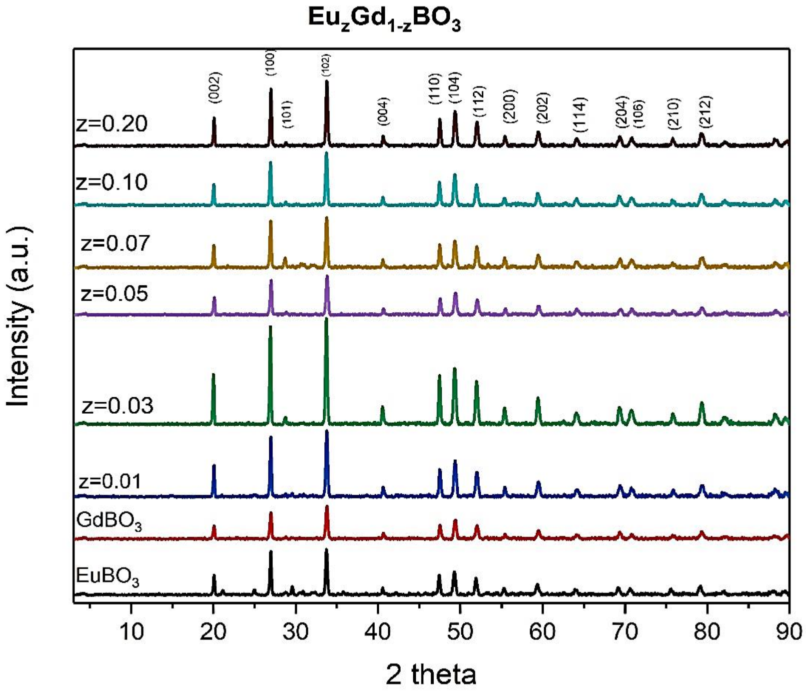

Figure 3.3. XRD patterns of Eu^{3+} doped $GdBO_3$ (z for Eu^{3+})

As it is observed in **Figure 3.3**, patterns of the doped compounds are very similar to each other, and the pure compound. Some tiny peaks are extra for 3% Eu^{3+} and 7% Eu^{3+} doped $GdBO_3$, and the reason for that the background subtraction method (or very thick sample holder: sample holder affects the background signal, and this affects the whole pattern for the compound). Besides, these peaks are checked for the belonging to $EuBO_3$, whether a $EuBO_3$ phase after dopant concentration of 10% (mole percentage), but they are not compatible with $EuBO_3$. Furthermore, XRD patterns cannot be used to differentiate different phase identification because XRD patterns of $EuBO_3$ and $GdBO_3$ are very similar.

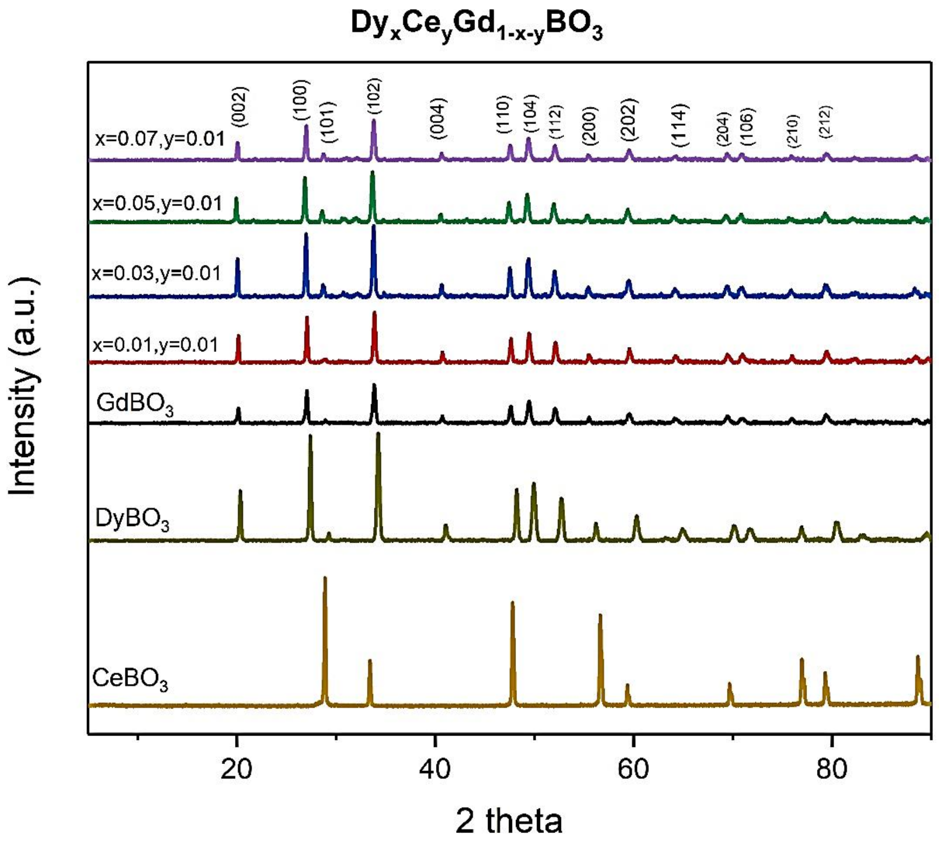

Figure 3.4. XRD patterns of phosphors have 0.01 Ce^{3+} and changing the concentration of Dy^{3+} (x for Dy^{3+} and y for Ce^{3+})

In these patterns (**Figure 3.4**), it is seen that the crystal structures were compared with pure $GdBO_3$, $DyBO_3$, and $CeBO_3$.Structures are the same with pure $GdBO_3$. The increasing concentration of Dy^{3+} ion did not affect the crystal structure of the host until the mole concentration of seven percent.

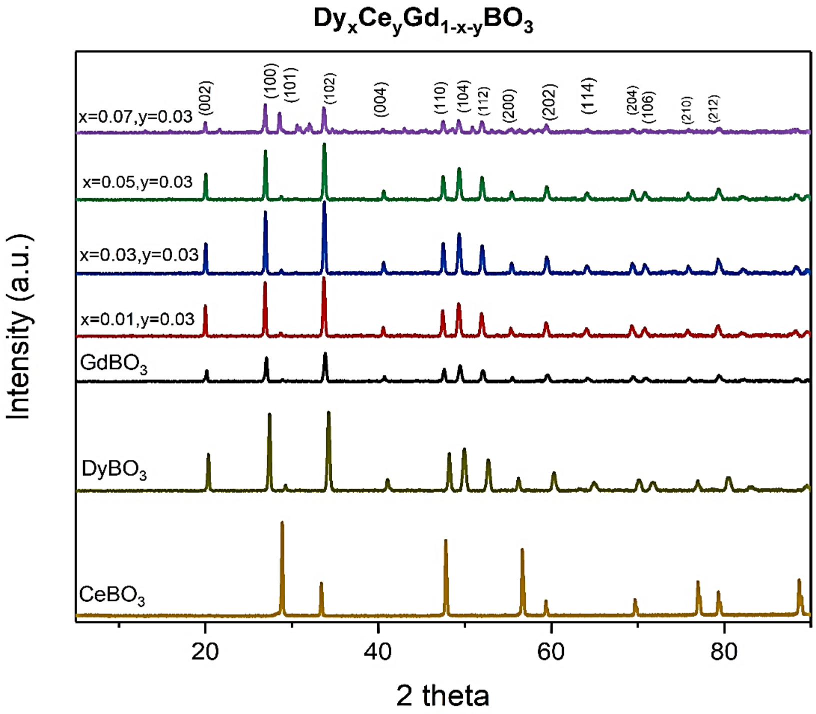

Figure 3.5. XRD patterns of phosphors have 0.03 Ce^{3+} and changing the concentration of Dy^{3+} (x for Dy^{3+} and y for Ce^{3+})

In these patterns (**Figure 3.5**), as it is seen, the crystal structures of the doped compounds agree with pure $GdBO_3$. Only different peaks around 40° - 60°, which are observable, exists the pattern, which was belonging to the concentrations of 3% Ce^{3+} and 7% Dy^{3+}. In these patterns, the same trend was available, which was Dy^{3+} affects the structure at 7% doping concentration.

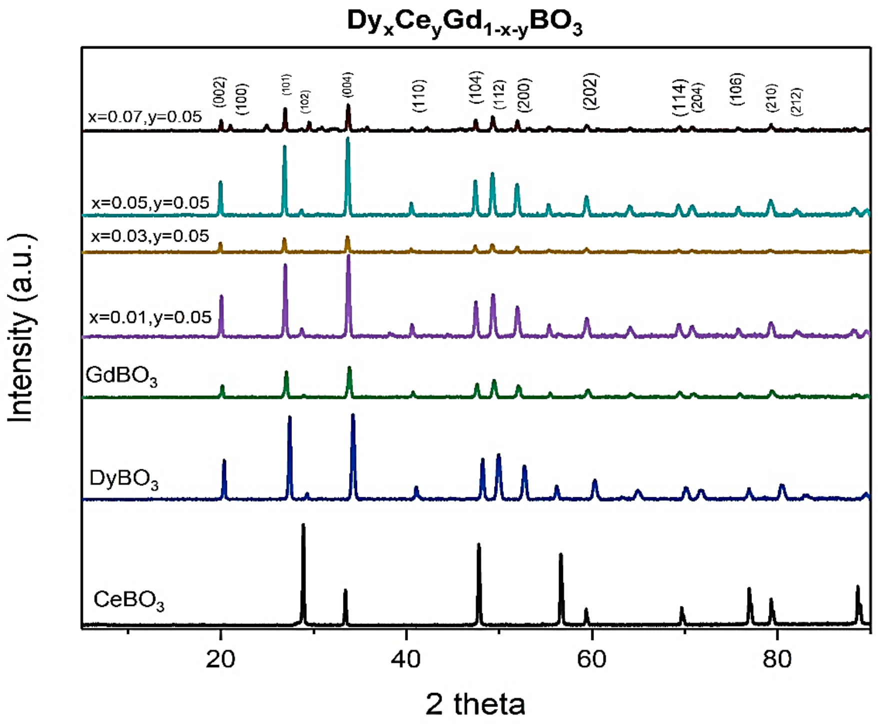

Figure 3.6. X-ray diffraction pattern of compounds have 5% Ce^{3+} (mol%) and changing concentration of Dy^{3+} (x for Dy^{3+} and y for Ce^{3+})

In **Figure 3.6**, according to the patterns of single Dy^{3+} doped and Ce^{3+}/Dy^{3+} codoped phosphors, after 7% percent doping concentration of Dy^{3+}, some structural disorders occurred. Because of that reason, the patterns were checked for the presence of the Dy_2O_3 phase, and the patterns were compared with JSPCD Card with number 26-0591 for checking the existence of the Dy_2O_3 phase in the structures. The XRD patterns of synthesized compounds are given for triple doped compounds in **Figure 3.7** and **Figure 3.8**.

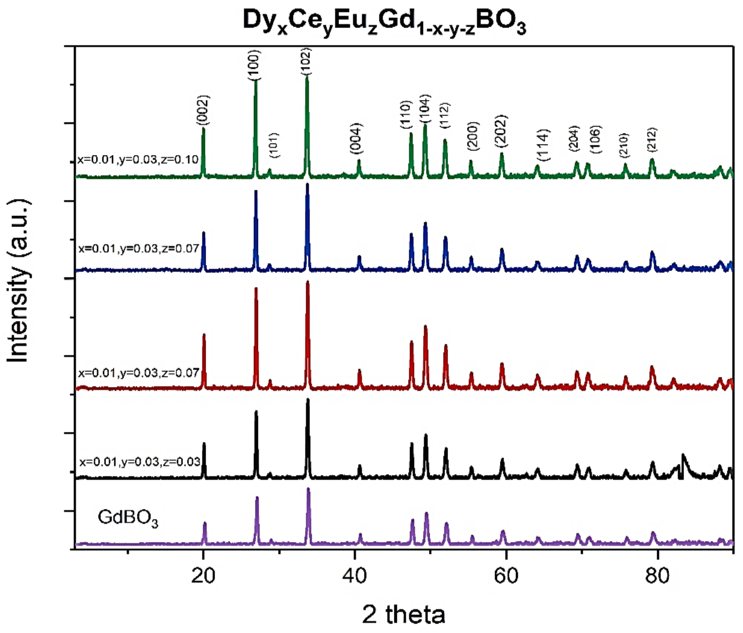

Figure 3.7. XRD patterns of GdBO3 with fixed Ce^{3+} and Dy^{3+} concentration and changing Eu^{3+} concentration

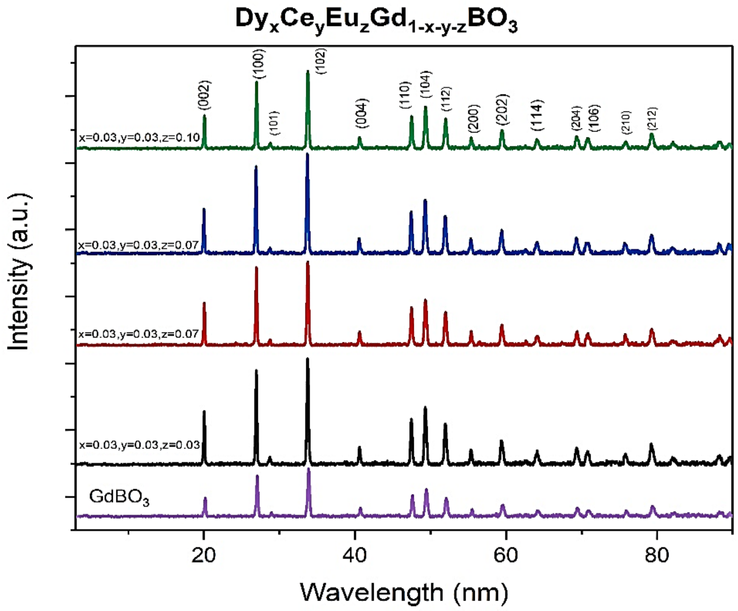

Figure 3.8. XRD patterns of GdBO3 with fixed Ce^{3+} and Dy^{3+} concentration and changing Eu^{3+} concentration

Figure 3.7 and **Figure 3.8** show the XRD patterns of triple doped $GdBO_3$, which have 1% Dy^{3+}-3% Ce^{3+} and 1% Dy^{3+}-3% Ce^{3+} with changing Eu^{3+} concentration are given. According to these patterns, it was achieved that all synthesized compounds were in the same phase with pure $GdBO_3$.

3.1.2 XRD Patterns of $Tb_xCe_yYb_zGd_{1-x-y-z}BO_3$

X-Ray studies for single doped Ce^{3+} were made for Dy-Ce-Eu doped $GdBO_3$ phosphors, and this study shows successful doping by means of Ce^{3+}. Tb^{3+} doped and Ce^{3+}/Tb^{3+} doped compounds were studied by a different paper in our group, and there was no additional phase identification (Akman, Ulusan, Banerjee, & Yılmaz, 2020). Moreover, Ce^{3+} co-doped Tb^{3+} compounds were studied in this thesis work. In this part, only Yb^{3+} single doped $GdBO_3$ compounds will be given. For clarification, the structures of the compounds are set as $Tb_xCe_yYb_zGd_{1-x-y-z}BO_3$.

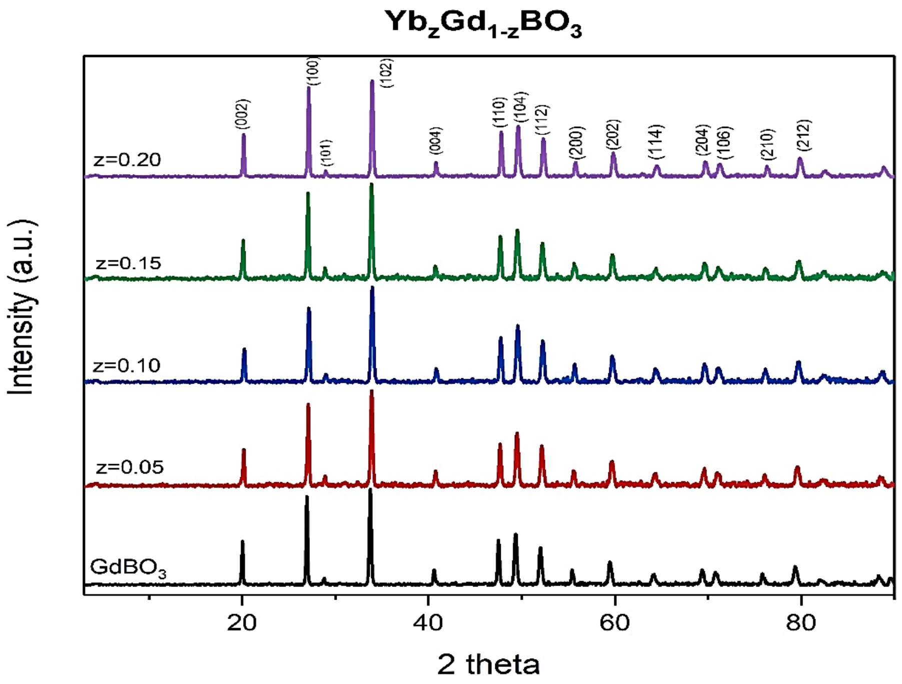

Figure 3.9. Single doped $GdBO_3$ with changing Yb^{3+} concentration (z=5%, 10%, 15%, 20%)

As seen in the patterns in **Figure 3.9**, there was no specific different phase in each of the samples. Every sample was compatible with $GdBO_3$ phase.

In this part of the study, XRD patterns of triple doped compounds will be given.

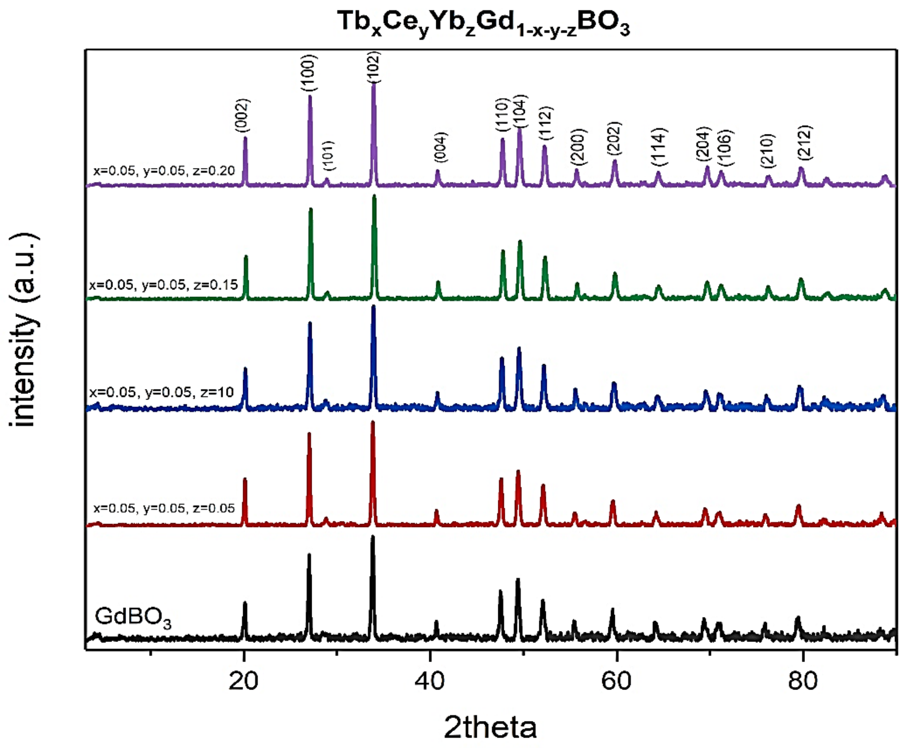

Figure 3.10. XRD patterns of $GdBO_3$ with fixed Ce^{3+} and Tb^{3+} concentration and changing Yb^{3+} concentration

Figure 3.10 shows that triple doping does not affect the crystal structure of the desired product, and they were available for further investigation.

3.2 Infrared Spectroscopy Studies

In this part of the study, the examination of the compound's doping was made to understand to synthesize the desired products by using the bonding properties of the products. For Infrared studies, several peaks are used for the determination, and they are related to the bending and stretching of B-O groups. These groups are given for the assignment of the main peaks on all of the spectra.

When the peaks in spectra are examined, there are peaks at 1373, 1376, and 1322 cm^{-1}, and they are assigned as stretching vibrations of trigonal BO$_3$ units only since 1176–1500 cm^{-1} is the result of B−O stretching vibrations of trigonal BO$_3$ groups only (Edukondalu, Srinivasu, Rahman, Sathe, & Kumar, 2014). Other peaks such as, at ∼1320–1470 B−O symmetric stretching vibrations of varied borate groups in BO$_3$ units B−O$^-$ symmetric stretching vibrations of diverse borate groups in BO$_2$O$^-$ (Balachander, Ramadevudu, Shareefuddin, Sayanna, & Venudharc, 2013), at 816 and 920 cm^{-1} stretching of (BO$_3$)$^{3-}$ (Dobretsova, Borovikova, Boldyrev, Kurazhkovskaya, & Leonyuk, 2014) and at ~3400 cm^{-1} peak occurs due to the presence of water molecules in KBr pellet. (Dobretsova et al., 2014) A different representation of the main borate groups, which can occur in rare earth borates, are given in **Figure 3.11**.

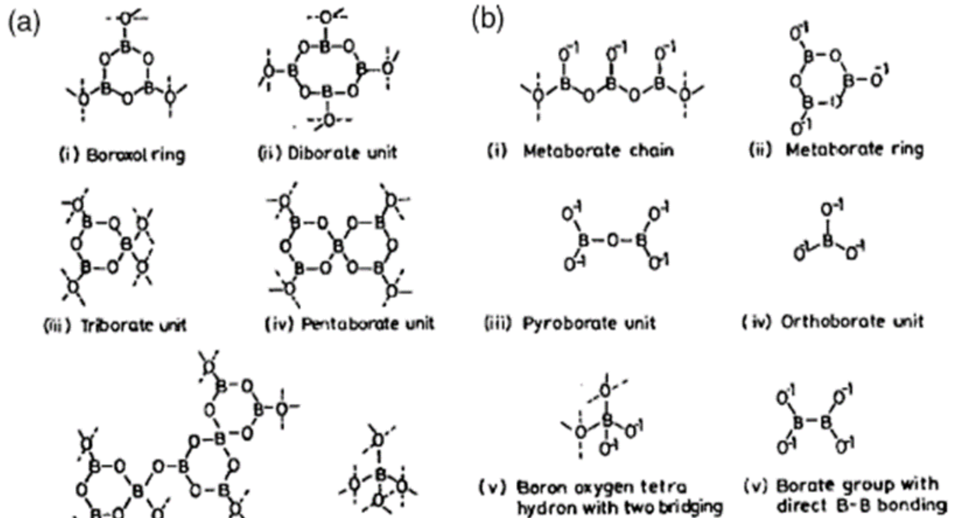

Figure 3.11. Some borate groups (Edukondalu et al., 2014)

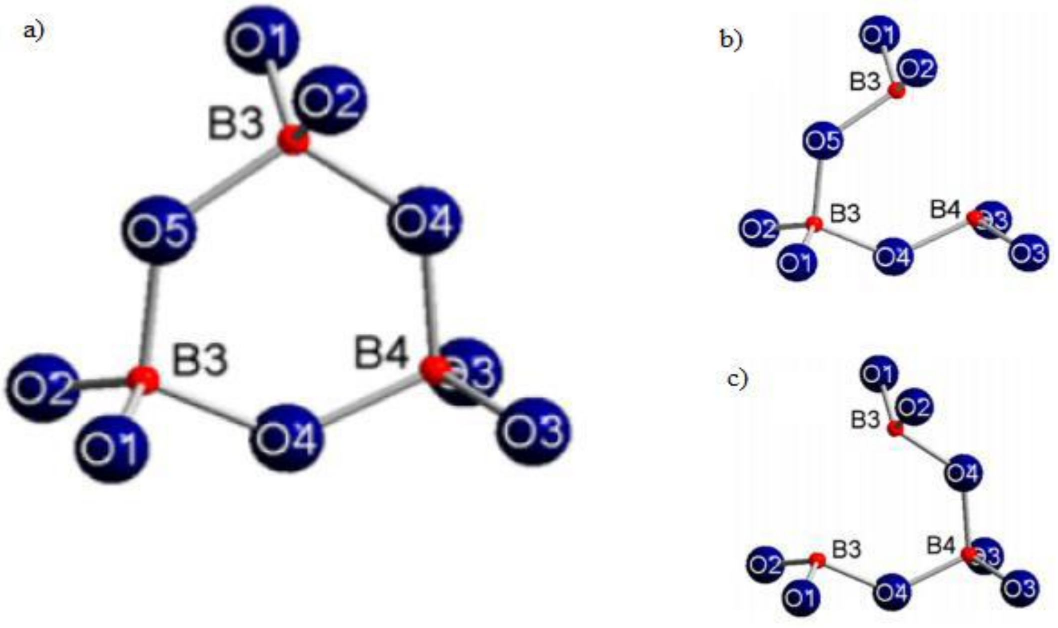

Figure 3.12. a) $B_3O_9^{9-}$ ring (b and c) coordination spheres of the B cations without one O4 or O5

Mainly, the crystal structure of $GdBO_3$ consists of $B_3O_9^{9-}$ group, and FTIR evidence of these groups are peaks between 900-1050 cm^{-1} (BO_4^- groups in the construction of $B_3O_9^{9-}$ group). (Ren et al., 1999) However, with the help of the synthesis method, isolated BO_3^{3-} groups are observed. (Z. J. Zhang et al., 2015) **Figure 3.12** represents the $B_3O_9^{9-}$ group and BO_3^{3-} group resulted from ring-opening.

3.2.1 FTIR Spectra of $Dy_xCe_yEu_zGd_{1-x-y-z}BO_3$

To the specification of the groups in the synthesized compounds, Infrared Radiation (IR) spectroscopy is used, and some of the vibrations are IR active. These modes are observed clearly in given spectra, and they are assigned according to literature values. IR analysis is semi-quantitative characterization; therefore, some of the peaks were not observable according to the amount of the analyzed sample. For each of the sets, different $GdBO_3$ were synthesized for avoiding error.

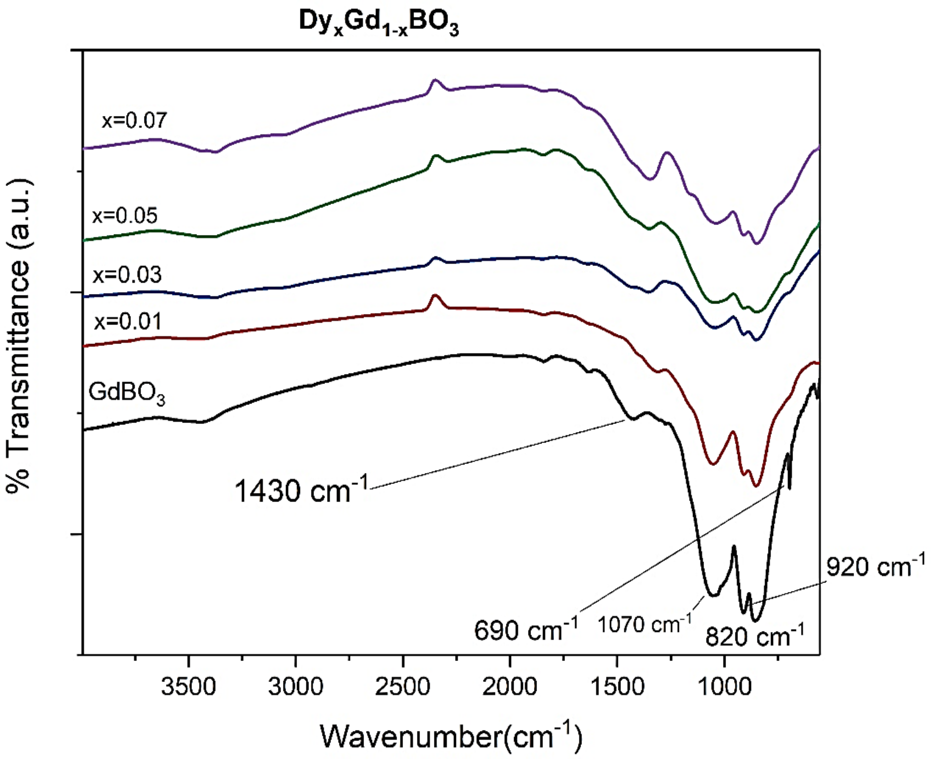

Figure 3.13. FTIR spectra of Dy^{3+} doped phosphors with changing concentration of Dy^{3+} (x for Dy^{3+})

These spectra in **Figure 3.13** show the effect of doping Dy^{3+} ion to $GdBO_3$ by means of bonding. The bonding properties of doped and undoped compounds were the same, and it means that the different phases that occurred in XRD patterns for

Dy^{3+} doped compounds could not be confirmed. The main peaks of the spectra are coherent with the pure compound. However, there is a difference at 1500 cm^{-1} because of the ring-opening property of BO_3 groups with doping. **Figure 3.14** gives the FTIR spectra of Ce^{3+} doped $GdBO_3$ with changing Ce^{3+} concentration. The peak around 1840 cm^{-1} is the CO_2 band, and because of the background subtraction method, the peak was lost in some of the spectra given.

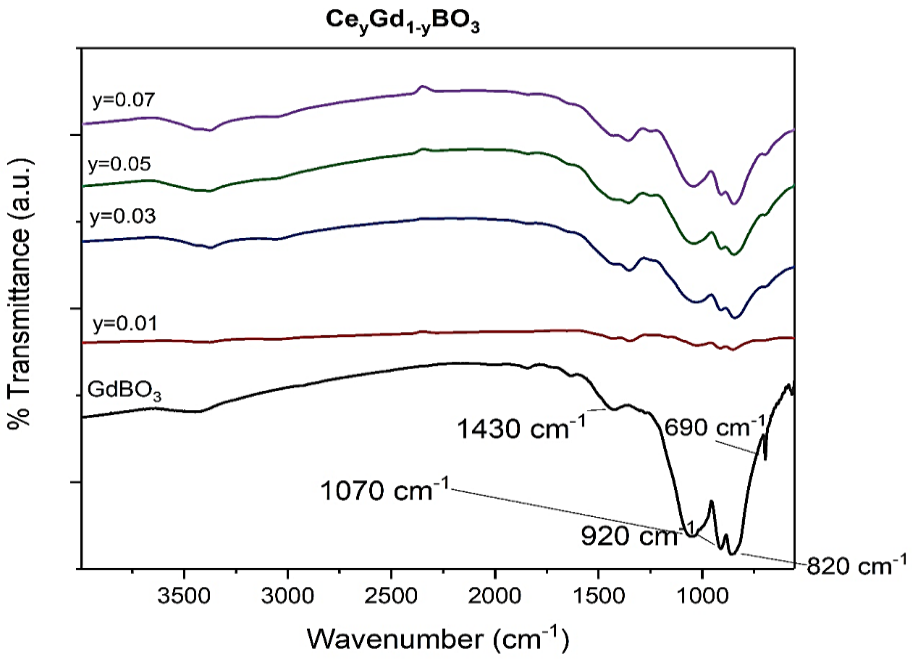

Figure 3.14. FTIR spectra of Ce^{3+} doped compounds with changing concentration of Ce^{3+} (y for Ce^{3+})

All of the synthesized compounds had the same bonding structure as pure compound as it was expected. At ~3400 cm^{-1} peak occurs due to the presence of water molecules in KBr pellet. (Dobretsova et al., 2014)

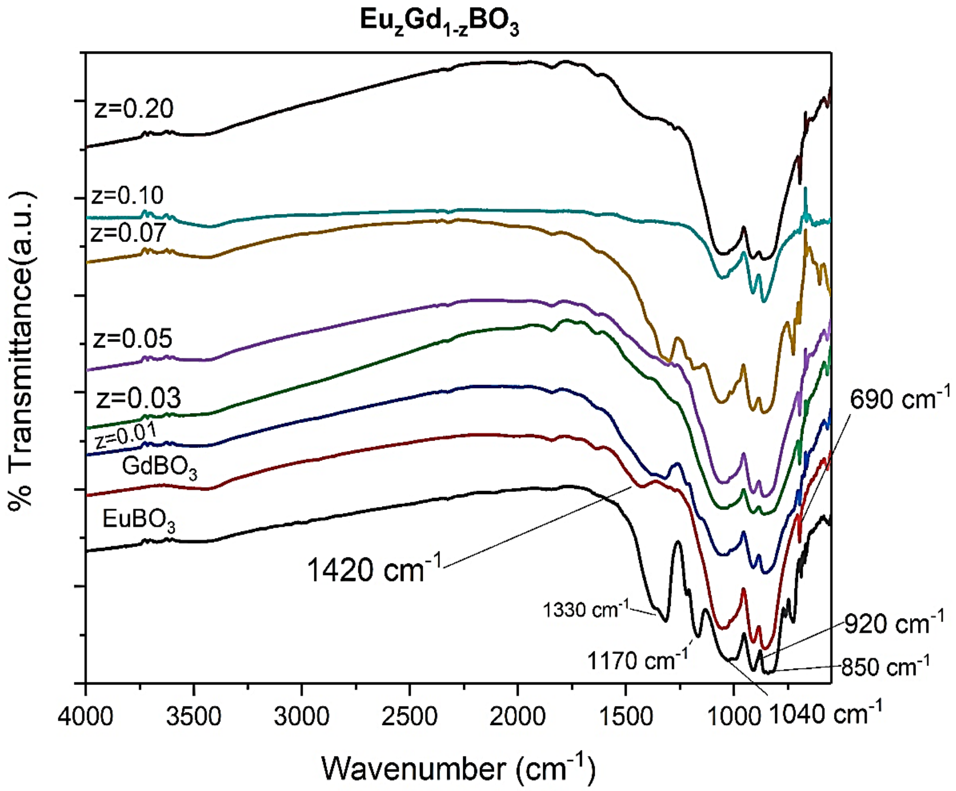

Figure 3.15. FTIR spectra of Eu^{3+} doped compounds with changing Eu^{3+} concentration (z for Eu^{3+})

Firstly, the spectra in **Figure 3.15** show that bonding types of $GdBO_3$ and $EuBO_3$ differ from each other, and we can estimate whether the $EuBO_3$ phase occurs or not. There is a peak around 1170 cm^{-1}, it can be helpful for the determination of that phase, and we can observe this at 7% Eu^{3+} doping causes emerge of $EuBO_3$ phase. Since the crystal structures of $EuBO_3$ and $GdBO_3$ are the same, this different phase could not be observed in XRD patterns.

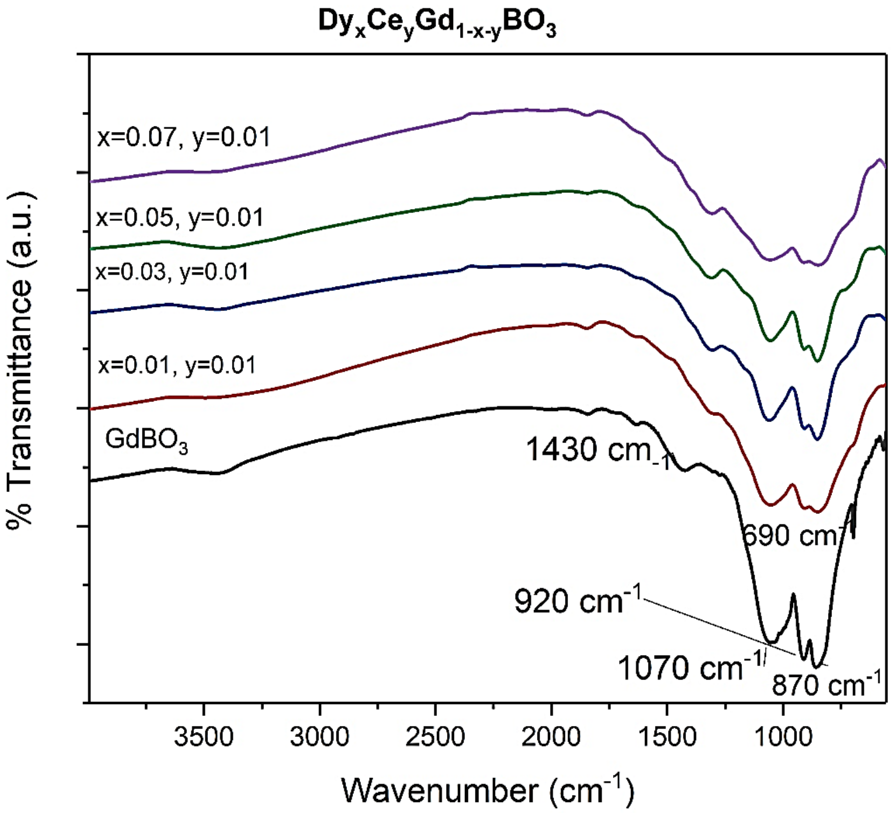

Figure 3.16. FTIR spectra of phosphors have 0.01 Ce^{3+} and changing the concentration of Dy^{3+}(x for Dy^{3+} and y for Ce^{3+})

In these spectra (**Figure 3.16**), the IR measurements of the 0.01 mole percentage of Ce^{3+} doped with changing Dy^{3+} doped compounds were given. Doped compounds are very similar to pure GdBO$_3$. However, there was a shift for the peak at 1420 cm^{-1} because of the changing bond strength resulting from dopants. At ~3400 cm^{-1} peak occurs due to the presence of water molecules in KBr pellet. (Dobretsova et al., 2014)

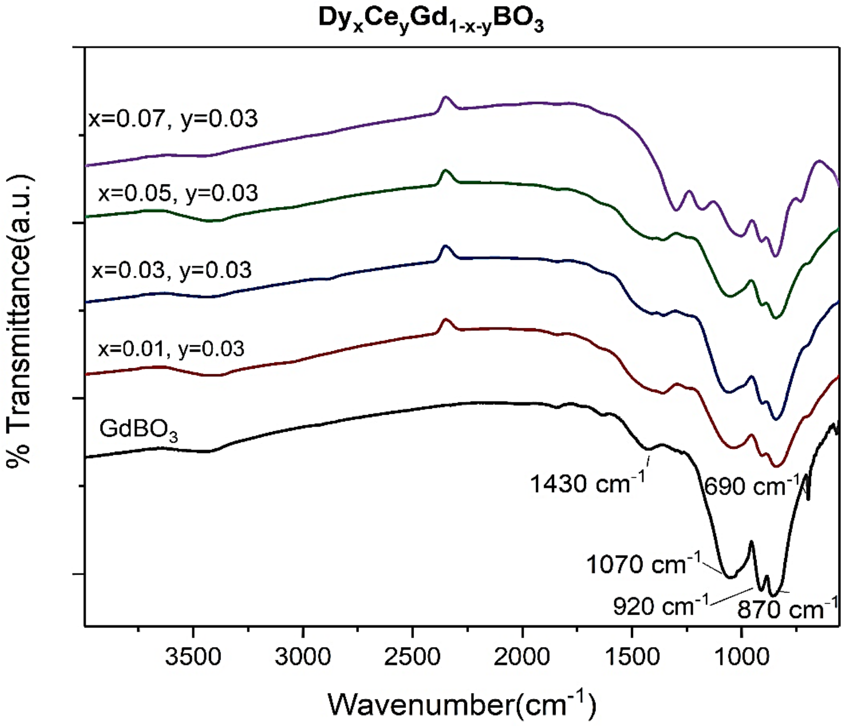

Figure 3.17. FTIR spectra of compounds have 0.03 Ce^{3+} and changing the concentration of Dy^{3+}(x for Dy^{3+} and y for Ce^{3+})

The spectra (**Figure 3.17**) show the IR measurements of 0.03 mole percentage Ce^{3+} doped with changing Dy^{3+} doped $GdBO_3$. According to these measurements, although there is no difference observable in XRD, a significant difference is seen between 3% (mole) Ce^{3+}, 7% (mole) Dy^{3+} doped, and pure $GdBO_3$. The reason for this result is that the crystal structure of $DyBO_3$ and $GdBO_3$ is the same.

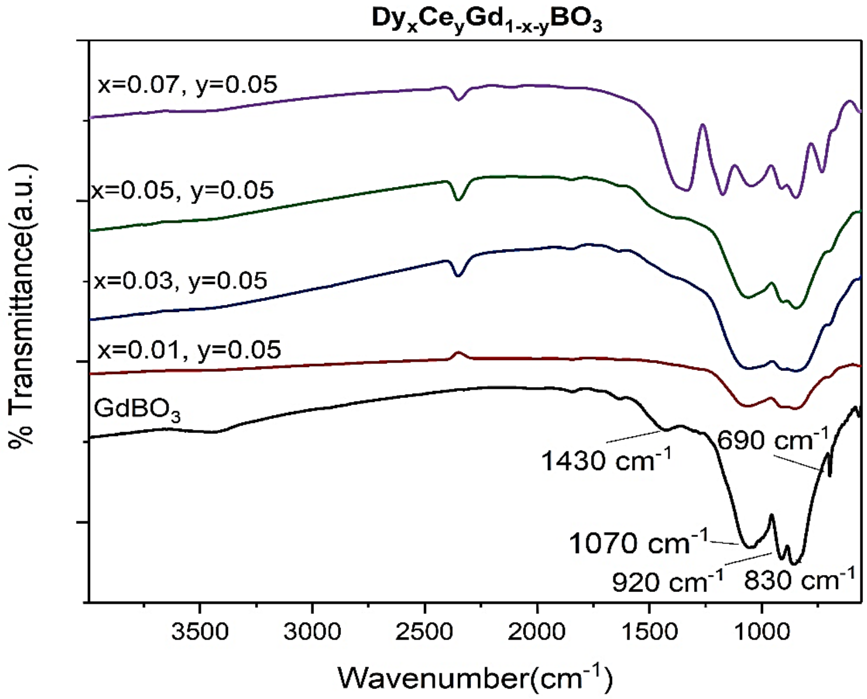

Figure 3.18. FTIR spectra of compounds have 0.05 Ce^{3+} and changing the concentration of Dy^{3+}(x for Dy^{3+} and y for Ce^{3+})

Therefore, due to these results in **Figure 3.18**, after 7% percent of dysprosium doping, doped compounds have different phases or phases. XRD results give evidence for this phase, and it was Dy_2O_3. **Figure 3.19** and **Figure 3.20** provide the FTIR with results of triple doped compounds, and it is clearly seen that bond opening property and the same structure between the pure compounds exist. As it was explained before, the peak around 1840 cm^{-1} was an instrumental error caused by the background.

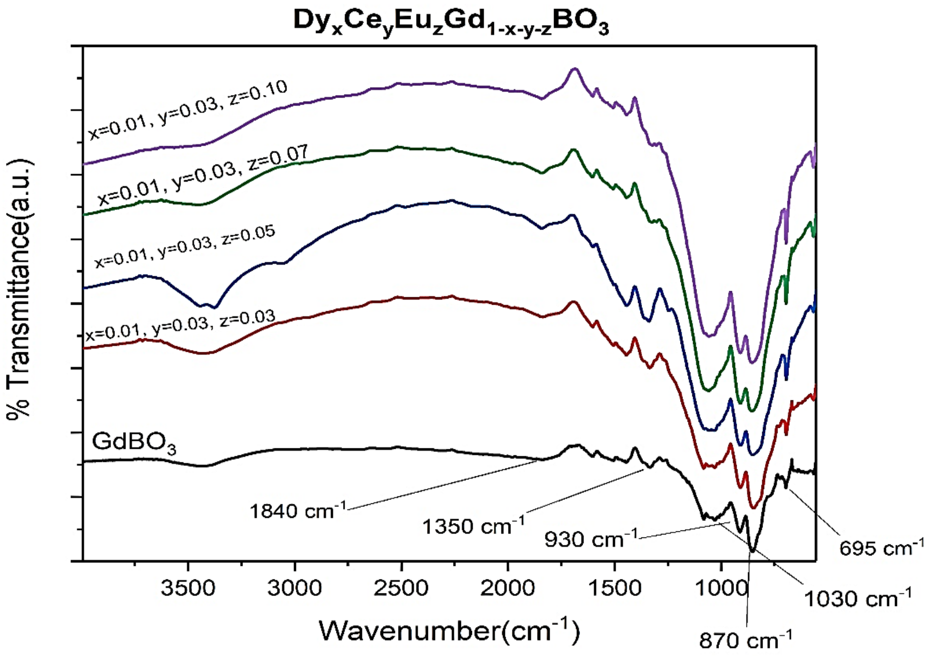

Figure 3.19. FTIR spectra of $GdBO_3$:0.01Dy, 0.03Ce with changing Eu^{3+} concentration

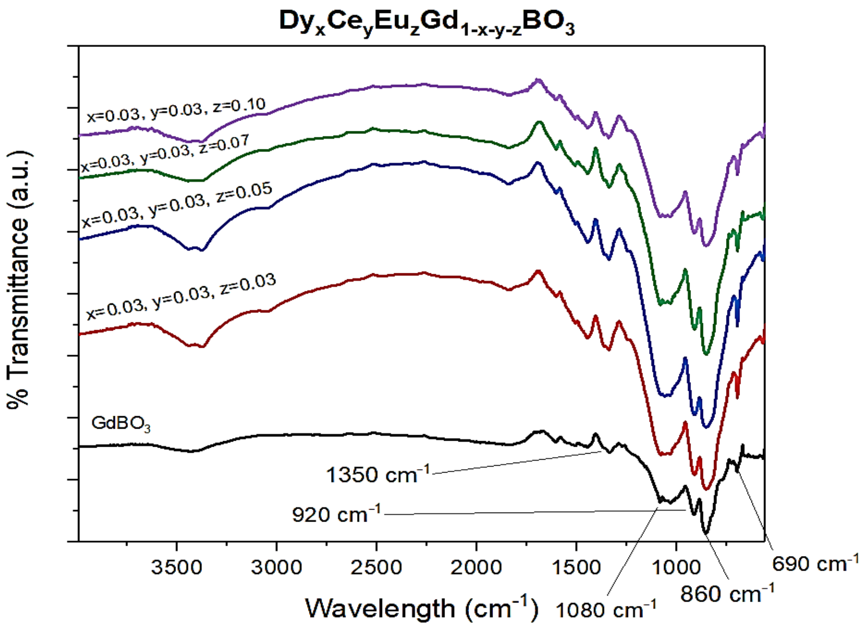

Figure 3.20. FTIR spectra of $GdBO_3$:0.01Dy, 0.03Ce with changing Eu^{3+} concentration

In Figure 3.20 and Figure 3.19, the FTIR spectra of triple doped compounds were given. The synthesized compounds and the pure compound have the same bonding properties. At ~3400 cm^{-1} peak occurs due to the presence of water molecules in the KBr pellet. (Dobretsova et al., 2014) As was mentioned before, the background subtraction method could cause errors.

3.2.2 FTIR Spectra of $Tb_xCe_yYb_zGd_{1-x-y-z}BO_3$

IR studies were made for single doped Yb^{3+} and triple doped compounds for the investigation of whether if different bonding types for doped compounds. The measurements were made for the wavenumber range of 500-4000 cm^{-1} for all of the compounds. For single doped compounds, IR studies were made, except for Yb$^{3+,}$ and this result was given in **Figure 3.21**.

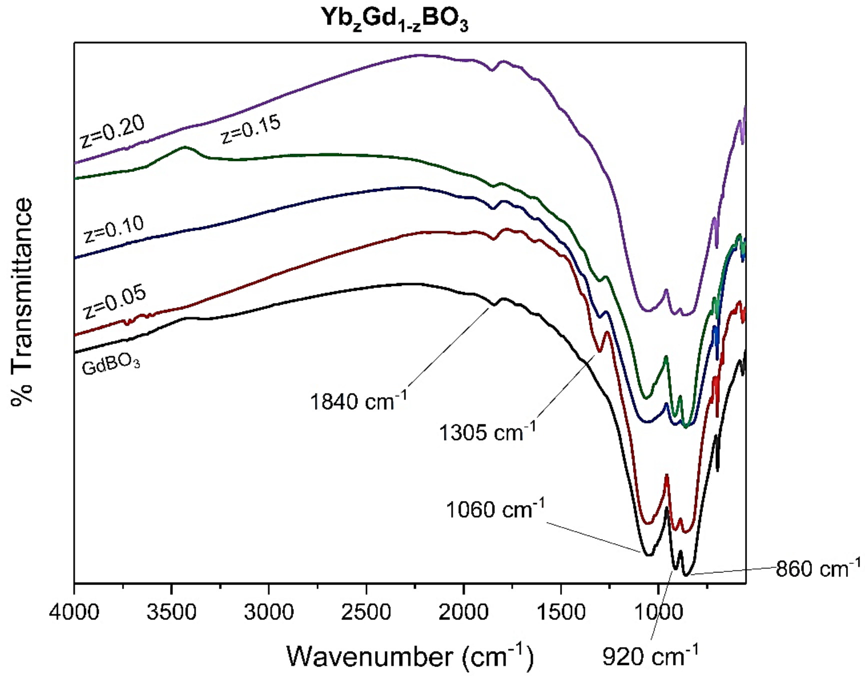

Figure 3.21. FTIR spectra of $GdBO_3$ with changing Yb^{3+} concentration

As it is seen in the figure, there was no bonding type different from the pure compound. The assignment of peaks in the spectra was made in the other part of the study. For comparison of the doped compound with pure compounds, another different compound synthesized with these doped ones was used to avoid changing the parameter of the synthesis method as it was made in the XRD study.

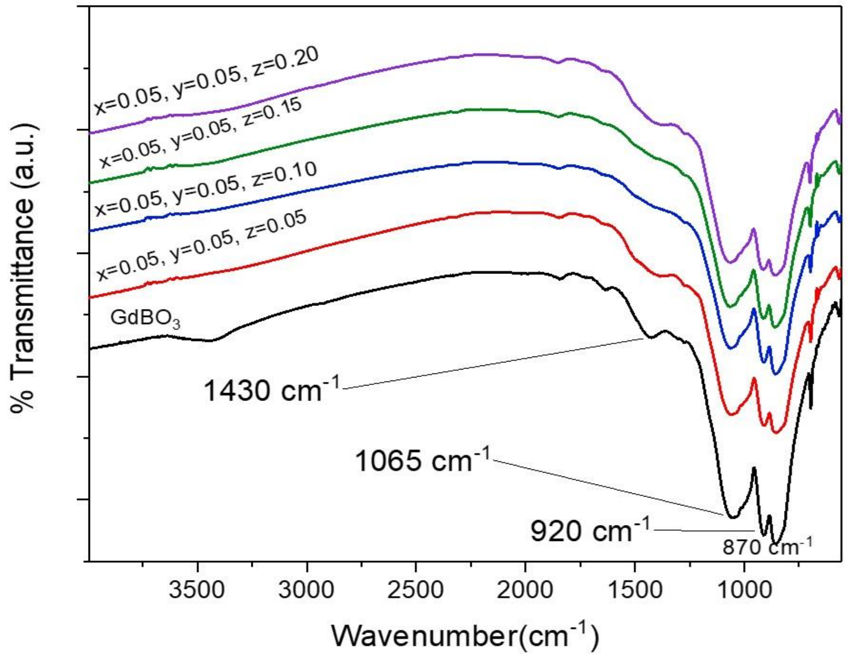

Figure 3.22. FTIR spectra of $GdBO_3$:0.05Tb, 0.05Ce with changing Yb^{3+} concentration

As it is seen in **Figure 3.22**, there was no bonding type different from the pure compound. The assignment of peaks in the spectra was made in the first part of the study. For comparison of the doped compound with pure compounds, another different compound synthesized with these doped compounds was used in order to avoid the effect of changing the parameter of the synthesis method as I was made in the XRD study.

3.3 SEM Images

With the help of SEM images, particle sizes and morphologies of desired products were determined. Some of the products which have the best luminescence activity examined.

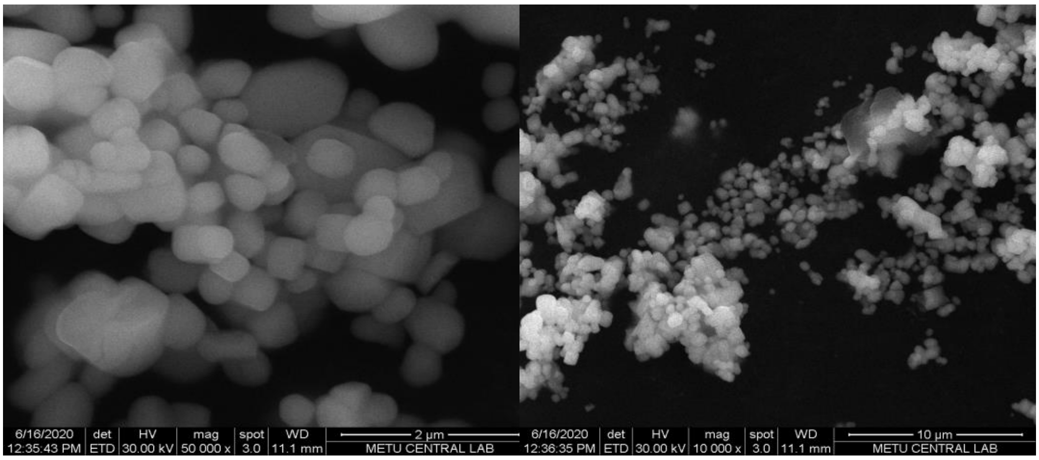

Figure 3.23. SEM images of Ce^{3+} doped $GdBO_3$

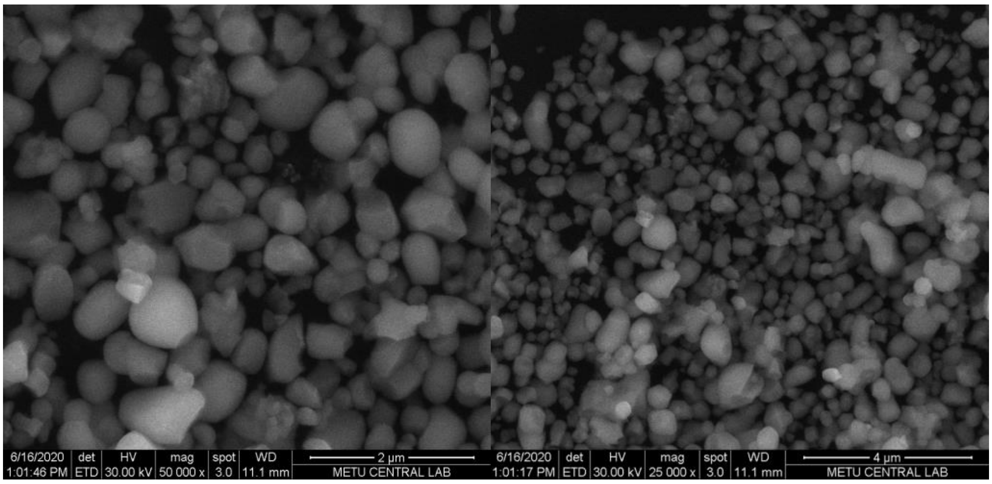

Figure 3.24. SEM images of Ce^{3+}/Dy^{3+} doped $GdBO_3$

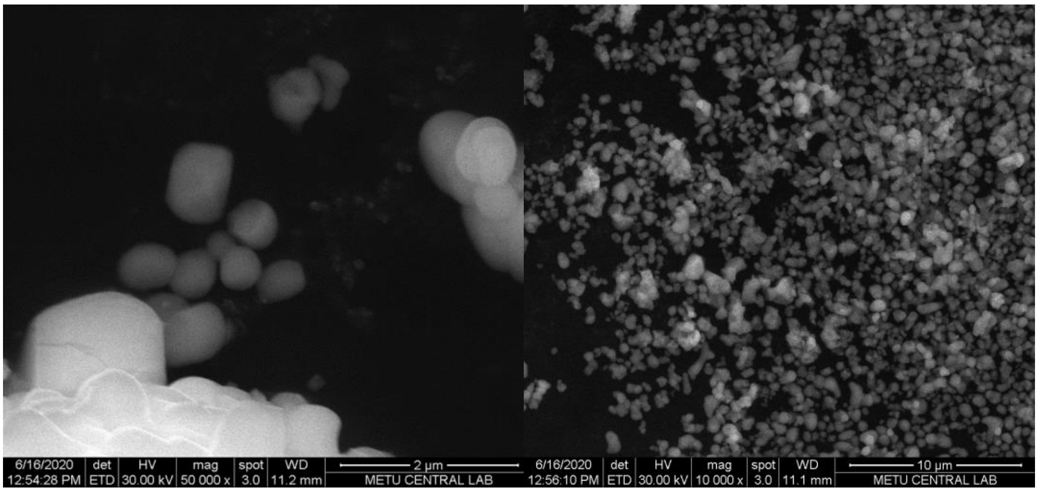

Figure 3.25. SEM images of Eu^{3+} doped $GdBO_3$

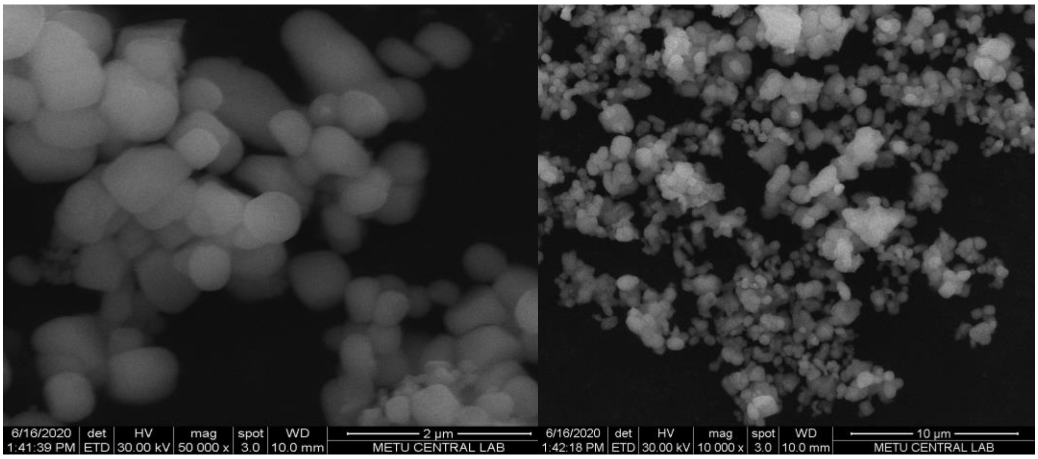

Figure 3.26. SEM images of Ce^{3+}/Dy^{3+}/Eu^{3+} doped $GdBO_3$

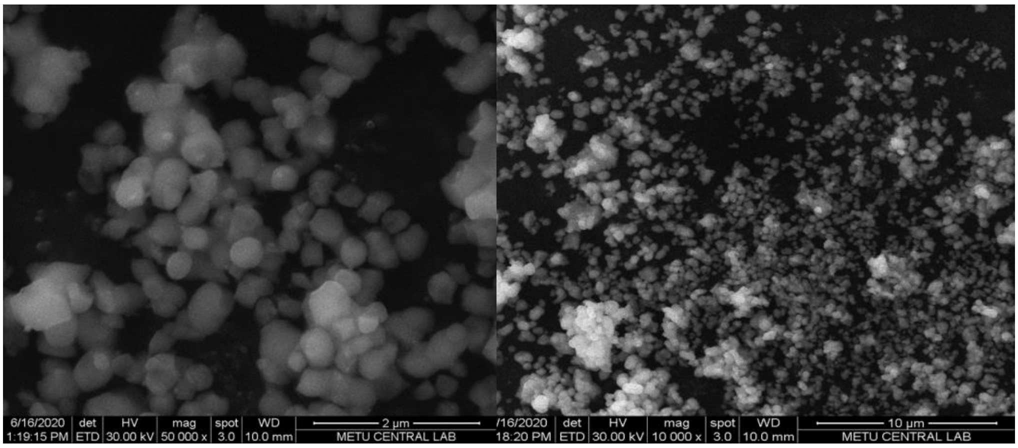

Figure 3.27. SEM images of Yb^{3+} single doped $GdBO_3$

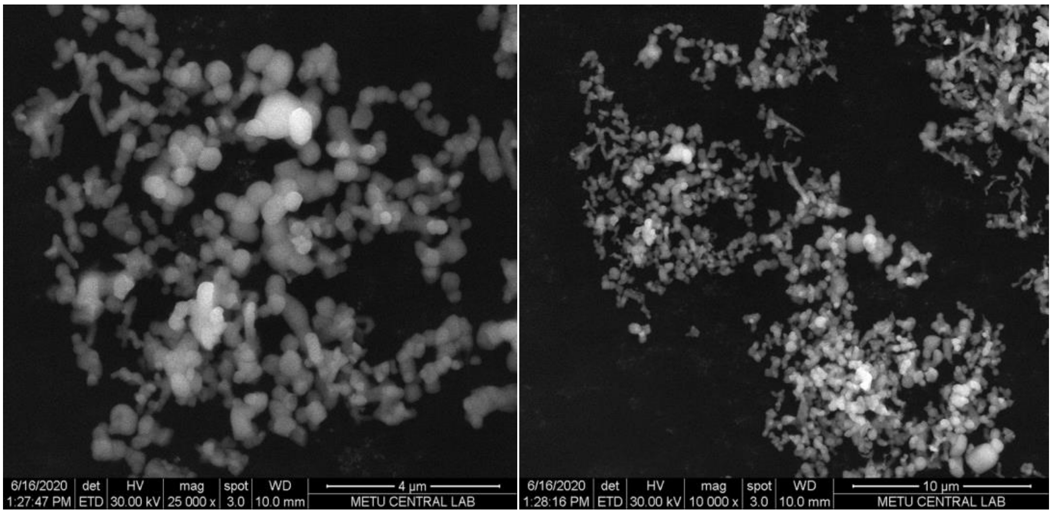

Figure 3.28. SEM images of Ce^{3+}/Tb^{3+}/Yb^{3+} doped $GdBO_3$

SEM images indicate that the morphology of the synthesized compounds does not change with dopant type or dopant concentration. Moreover, particle sizes of them approximately similar.

3.3.1.1 SEM Images of Same Compounds Synthesized with Different Methods

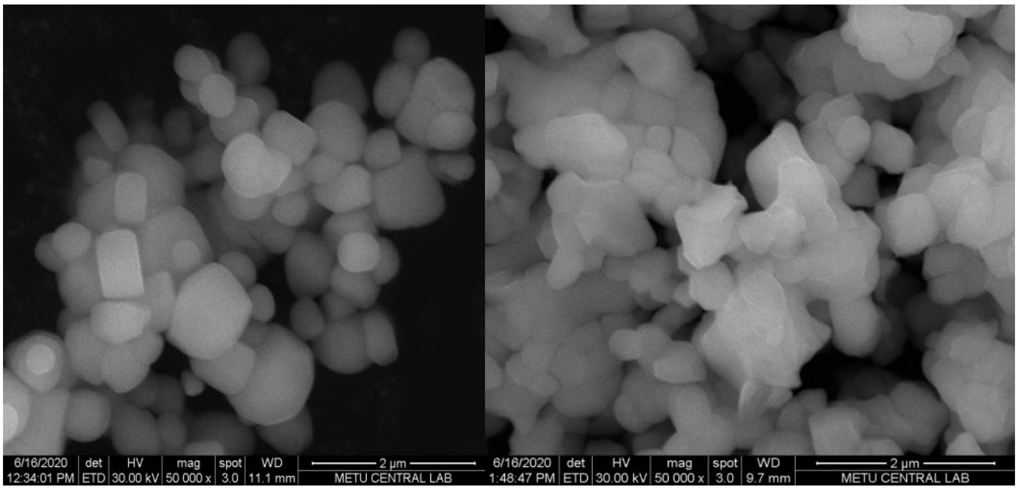

Figure 3.29. SEM images of Sol-Gel synthesized (right) and solid-state synthesized 5% Ce^{3+} doped $GdBO_3$ phosphors

In this part of the study, MW assisted, and sol-gel synthesized particles were used. It is observed in **Figure 3.29** that the solid-state method causes more agglomeration, and particle sizes of the compound are much bigger than sol-gel synthesized ones. Moreover, shapes that are a more regular occurrence with the sol-gel synthesis method. These are very important for the usage of these compounds

3.4 Photoluminescence Studies

In this study, it is expected that triple doped compounds can be excited by lights with different wavelengths and these compounds have both downconversion and upconversion property. Therefore, this part of the study will split into two parts. The first part is the downconversion, and the second part is the upconversion.

3.4.1 Photoluminescence Studies of $Dy_xCe_yEu_zGd_{1-x-y-z}BO_3$

In this part, photoluminescent properties of single Dy^{3+}, $Ce^{3+,}$ and Eu^{3+} doped $GdBO_3$ and Ce^{3+}, Dy^{3+} co-doped, and Ce^{3+}, Dy^{3+}, Eu^{3+} triple doped phosphors with different concentration were examined. All of the doped rare earth metal ions have Downconversion property. Excitation spectra were observed between 300 and 400 nm, which is a small range of ultraviolet light range. Excitation spectra were measured by using the emission wavelengths known in the literature. By utilizing these excitation wavelengths, the emission spectra were taken. As it was mentioned in the ‘Introduction’ part, the energy states of the ions do not change very much. Therefore emission wavelengths can be used for photoluminescence studies.

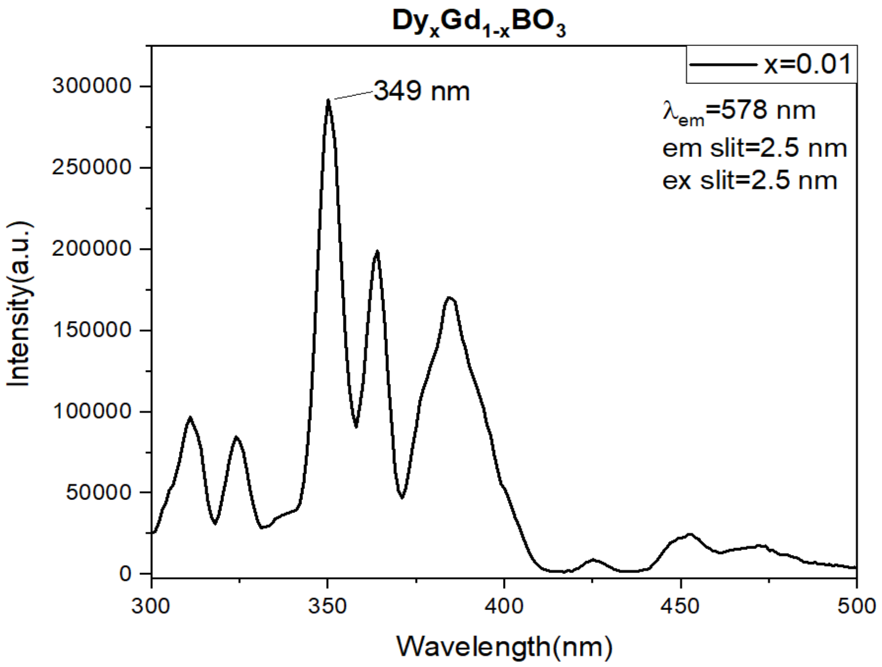

Figure 3.30. The excitation spectrum of Dy^{3+} single doped $GdBO_3$

Moreover, the emission spectra were observed between 400 and 700 nm, which is the visible light range. Besides, the excitation and emission slit width was 5 nm for each. For determination wavelength on of the excitation wavelength of Dy^{3+} single doped phosphors, a value, 575 nm, was used as emitted light wavelength. The excitation spectrum of Dy^{3+} single doped was given below. For the determination of excitation wavelength, the phosphor, which has a doping concentration of 1 percentage, was used (**Figure 3.30**).

When the literature value was used for taking the excitation spectrum and then cross-checked with the emission spectrum with the excitation spectrum, it was determined that 578 nm was the best emission wavelength for taking the excitation spectrum, and it is obviously seen that the excitation spectrum intensity increases from 575 nm to 578 nm. This change is about the changing host material since when the host material changes the electronic and magnetic environment of the dopant change, and this changes the energy gap between the electronic states of dopant. It was determined that the best excitation wavelength of the phosphors was 349 nm. The emission spectrum of Dy^{3+} single doped $GdBO_3$ compounds with changing concentration is given in **Figure 3.24**.

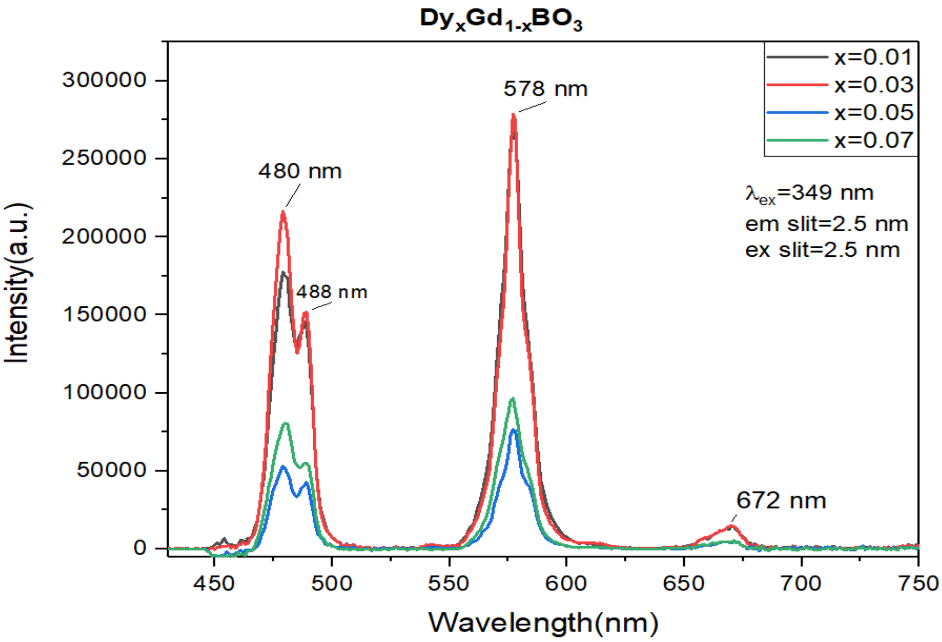

Figure 3.31. Emission spectra of Dy^{3+} single doped $GdBO_3$

Excitation spectra (**Figure 3.31**) of the compound were taken for changing concentration as x= 0.01, 0.03, 0.05, and 0.07 in terms of mole fraction. The peaks shown in the spectra were the result of the transitions from $^4F_{9/2}$ to $^6H_{15/2}$ (488 nm), $^6H_{13/2}$ (578 nm), and $^6H_{11/2}$ (672 nm). As is seen above, the best mole fraction for high intensity is x= 0.03. The light intensity increases from x= 0.01 to 0.03; however, after x=0.03, the light intensity decreases with increasing mole fraction. A decrease in the is probably about increasing mole fraction causes the Dy^{3+} in the crystal closing to each other so much, and this causes non-radiational relaxation.

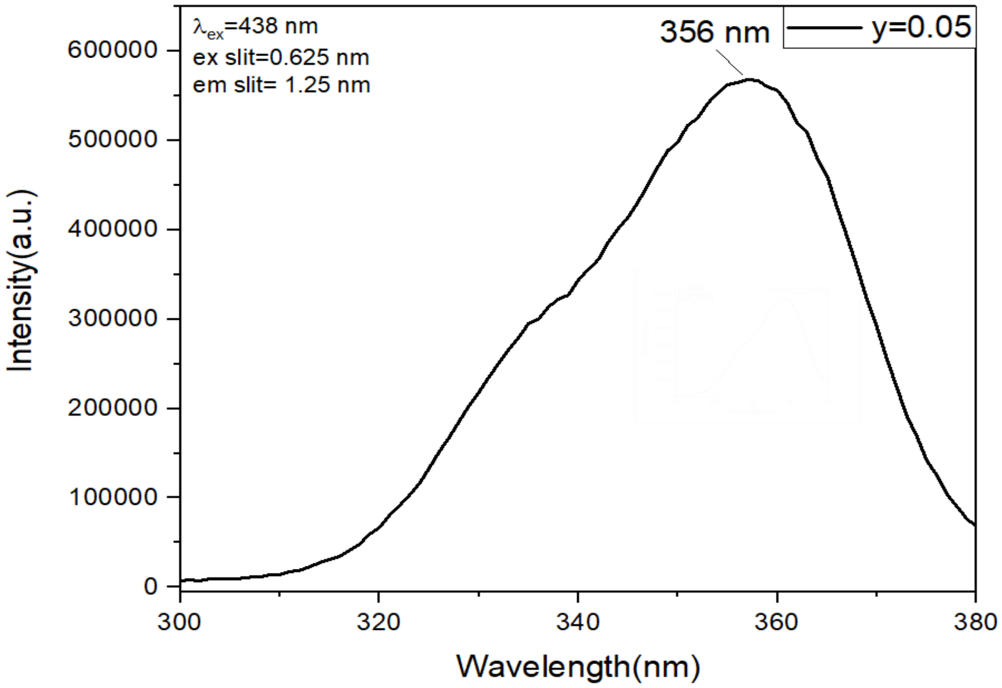

Figure 3.32. The excitation spectrum of Ce^{3+} single doped $GdBO_3$

In addition, only the emission spectrum of Ce^{3+} single doped $GdBO_3$ was observed and is given in **Figure 3.32**. However, the excitation spectrum at 438 nm was taken, and the best excitation wavelength was determined as 356 nm, and also 331 nm, which is the literature value for the excitation of Ce^{3+}, was used for clearance of the best dopant concentration for Ce^{3+} ion. In **Figure 3.33** and **Figure 3.34**, emission spectra of Ce^{3+} doped $GdBO_3$ were given. In these measurements, 438-nm emission was expected as the main emission line, but the taken measurements showed an unexpected situation. In order to clear the emission of Ce^{3+}, the emission filter (450 long-pass) was not used, and the taken spectra were given in the figures.

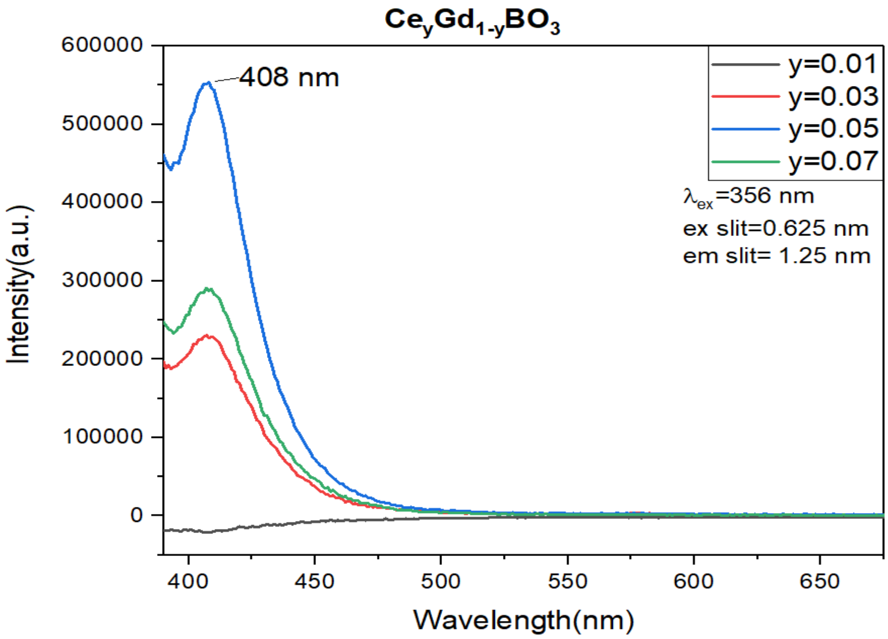

Figure 3.33. Emission spectra of Ce^{3+} single doped $GdBO_3$ at 356 nm without filter

By using this excitation wavelength, the total emission of Ce^{3+} ion could be determined. In most of the publications in the literature, 438 nm is the main emission line for Ce^{3+} ion, but in this study, two emission lines centered at 378 and 408 nm were observed. The reason for that energy states in 5d orbital are not definite. Therefore, emission lines can change according to host material and excitation wavelength. (Bahadur, Dwivedi, & Rai, 2013)(Herrmann et al., 2015) This is also about non-radiative relaxation, which is caused by the closing of Ce^{3+} ions. Since the emission of Ce^{3+} ion continues before 380 nm, the measurements after these emissions were taken with 331 nm, which is the literatüre value for Ce^{3+} excitation.

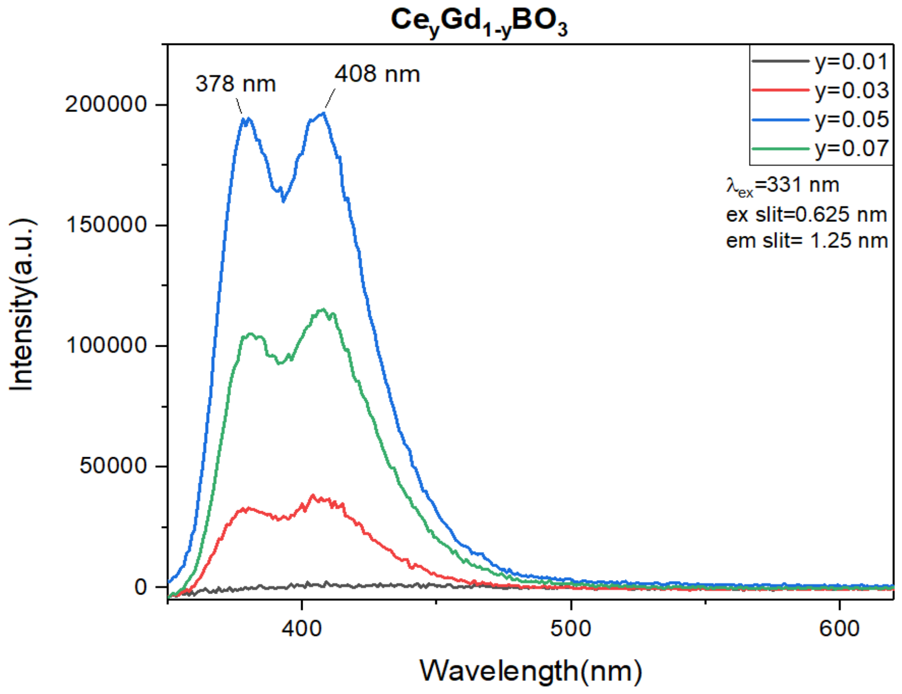

Figure 3.34. Emission spectra of Ce^{3+} single doped GdBO$_3$ with changing concentration at 331-nm excitation without filter

For the clearance of choosing the best concentration, the literature value for excitation of Ce^{3+} ion was used to observe the emission spectra. On these spectra (**Figure 3.34**), the best level for the emission was also 5% Ce^{3+}. For better comparison, another excitation wavelength (331 nm), which is found in literature, was used, and clearly, the best emissive concentration was also observed as 5% Ce^{3+}. As it was explained before, there can be different lines from 438 nm. According to Bahadur et al., these different emission lines provide information that there are two different Ce^{3+} in different electronical environment. (2013) When these results were compared with XRD patterns and FTIR spectra, there was no structural explanation. Also, the measurements made with the emission filter were given in the 'Appendices' part.

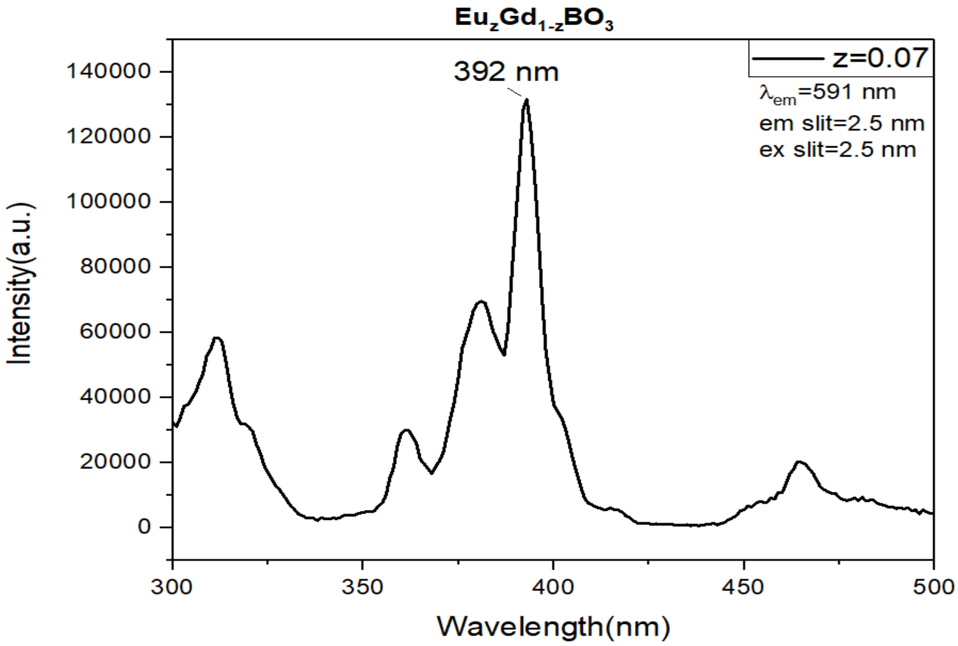

Figure 3.35. The excitation spectrum of Eu^{3+} doped $GdBO_3$

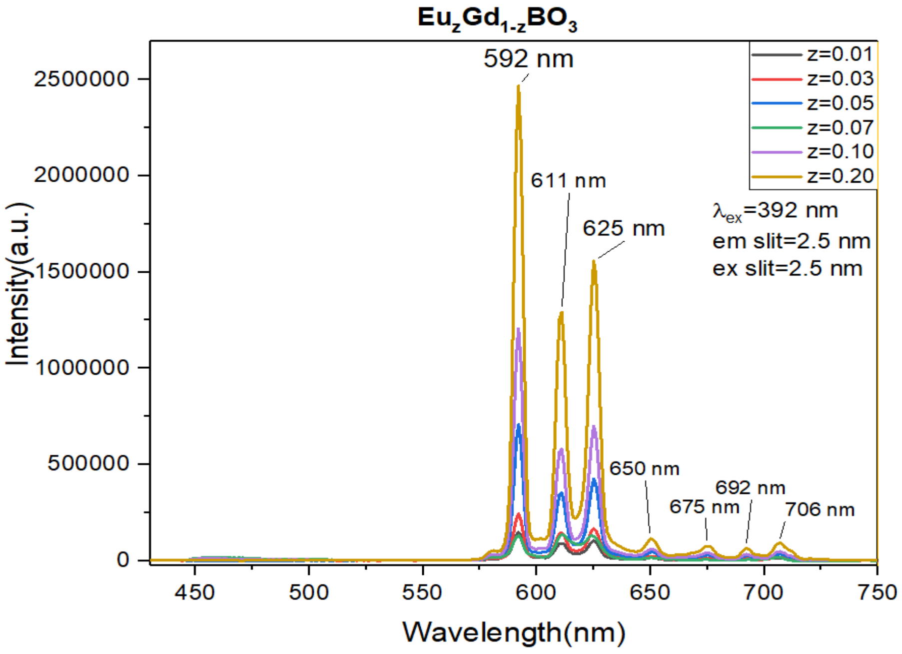

Figure 3.36. Emission spectra of Eu^{3+} single doped $GdBO_3$ at 392 nm

As it was mentioned before, Eu^{3+} emission occurs at three specific wavelengths, which are 592, 610, and 616 nm. Since the most intense line is at 592 nm for most of the Eu^{3+} compounds, the excitation wavelength was chosen as 592 nm, and the concentration of the Eu^{3+} doped phosphor is 20 percent by means of mole. The excitation spectrum is given (**Figure 3.35**).

In **Figure 3.36**, the Eu^{3+} doped $GdBO_3$ phosphors were excited with different wavelengths. Samples show the same trend, and 20% Eu^{3+} doped particles gave the highest intensity emission. However, according to FTIR spectra of Eu3+ doped compounds, there was a $EuBO_3$ in the structures. Therefore the emission after 5 percent of doped compounds resulted from this extra phase.

In order to decide the best concentration for luminescence, single Eu^{3+} doping processes were made with different concentrations, and the best concentration for the emission at 591 nm was 10% Eu^{3+}. The measurement for this emission will be repeated for exact results. However, some approximations can be made. Firstly, this is the literature value for excitation of Eu^{3+}, but the compounds have to be excited with the light that was found in the excitation spectrum. Therefore, emission will increase with a precise light beam. It can also be said that the emitted light from the compounds does not come from $EuBO_3$. In the literature, the most common wavelength for excitation of Eu^{3+} is 392 nm because, for that reason, a second measurement was made for different wavelengths. Eu^{3+} emissions are the results of $^5D_0 \rightarrow {}^7F_1$ (592 nm), $^5D_0 \rightarrow {}^7F_2$ (615 nm) and $^5D_0 \rightarrow {}^7F_4$ (700 nm) transitions. After that, Ce^{3+}, Dy^{3+} co-doped $GdBO_3$ phosphors were examined. Since the excitation wavelength of both, only emission spectra of the compounds were taken. Firstly, y=0.01, and x=0.01, 0.03, 0.05 and 0.07 at 349 nm and 356 nm compounds were given.

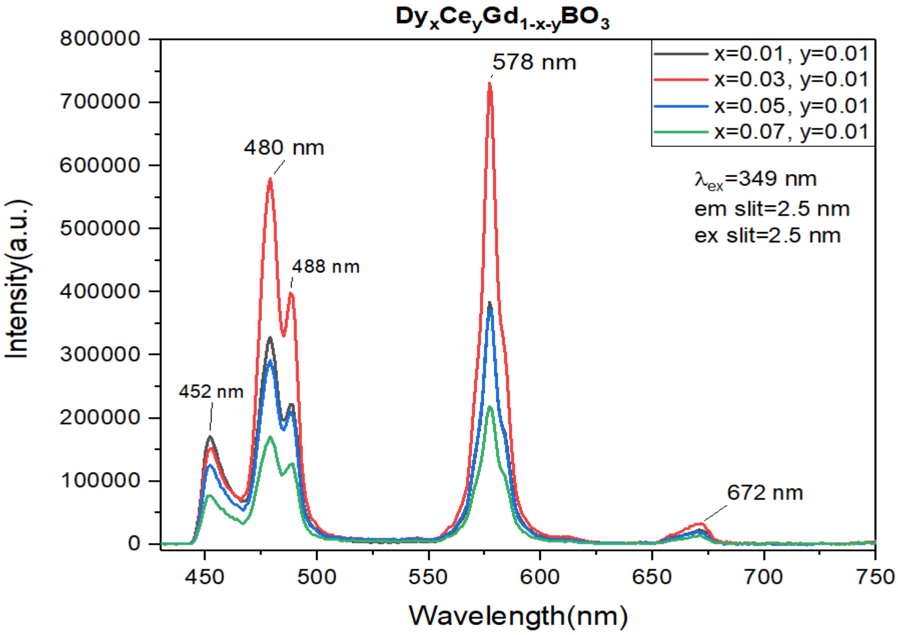

Figure 3.37. Emission spectra of 1% Ce^{3+} fixed and Dy^{3+} doped with changing concentration at 349 nm

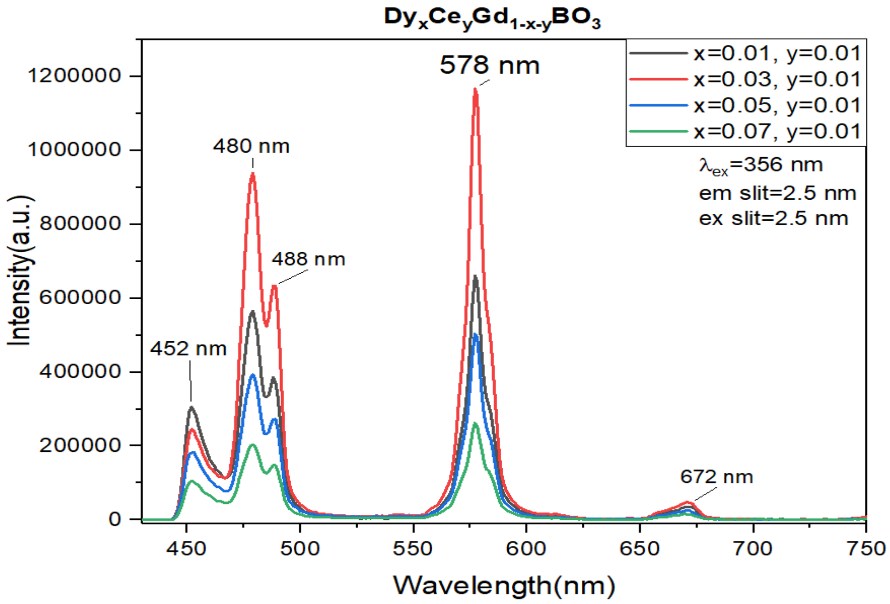

Figure 3.38. Emission spectra of 1% Ce^{3+} fixed and Dy^{3+} doped with changing concentration at 356 nm without filter

As it is seen in **Figure 3.37**, the best for the emission at 438 nm, the best mole fraction is at x= 0.01 and y= 0.01. However, for the emission at 578 nm, x= 0.01, y= 0.03 and x= 0.05, y= 0.01 are very similar so due to easiness of synthesis, the best choice is x= 0.03, y= 0.01. Since the concentration of sensitizer ion was very low in the compounds, emission of Dy^{3+} can be increased, therefore in the next spectra, the concentration of sensitizer.

In these spectra (**Figure 3.38**), the spectra are given without using filter for the clearance of the emissions. The filtered emission was given in the 'Appendices' part. Also, since 356 nm and 349 nm are close to each other for excitation, it can be used for the comparison of emissions. In order to take total emission, 331 nm light was used as an excitation source. According to the measurement, the best choice for both Dy^{3+} and Ce^{3+} ions was x= 0.03, y=0.01.

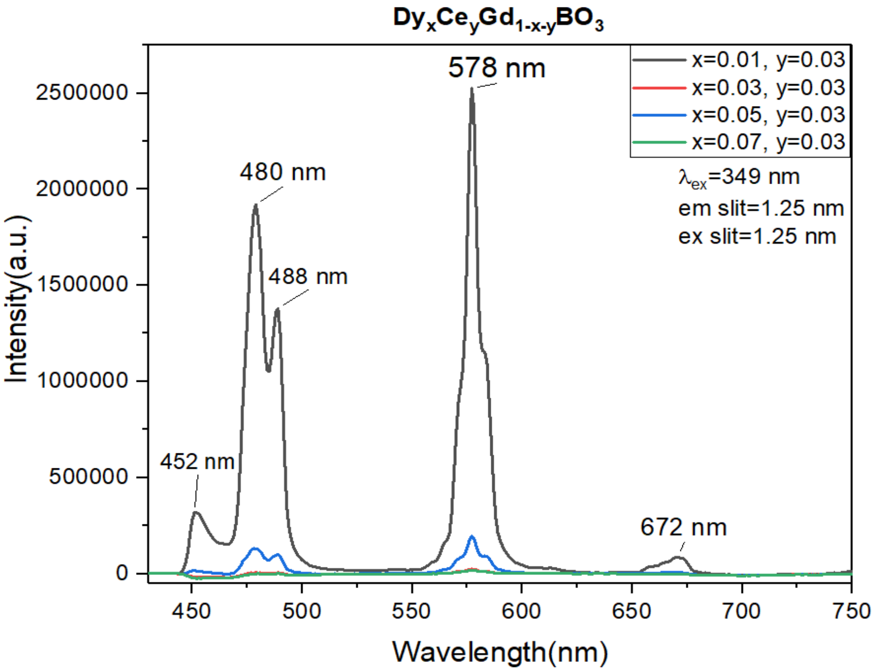

Figure 3.39. Emission spectra of 3% Ce^{3+} fixed and Dy^{3+} doped with changing concentration at 349 nm

As is seen in **Figure 3.39**, for the best emission at 380 and 408 nm, the best mole fraction is at x= 0.01 and y= 0.03 for both of the emitted lines. Therefore, this was the best dopant concentration for Dy^{3+} emission. An increase in the concentration of Ce^{3+} ion affected both of the emission from Ce^{3+} ion and Dy^{3+} ion. Also, the emission at 672 nm is the emission of Dy^{3+} ion. For the comparison of the best emission intensities, filtered measurements were used in order to observe the whole visible range. According to this comparison, the best concentration for both emission and energy transfer is 1%Dy^{3+}-3%Ce^{3+}.

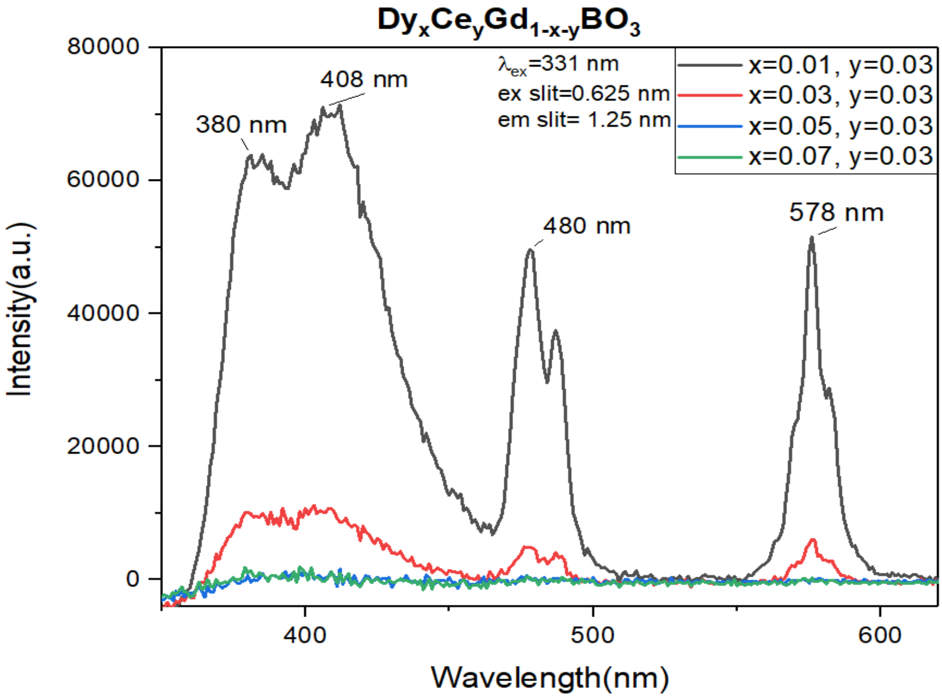

Figure 3.40. Emission spectra of 3% Ce^{3+} fixed and Dy^{3+} doped with changing concentration at 356 nm without filter

In these spectra (**Figure 3.40**), although the wavelength of excitation changed, the best choice for the emission of Dy^{3+} and Ce^{3+} is at the mole fraction of x=0.01, y=0.03. The measurement was taken with filter under 356-nm excitation, and there was no change in the main emission line of Dy^{3+} (‘Appendices’ part). By using these spectra, it could also be seen the Dy^{3+} emission at 672 nm. After these measurements, the emission of both Ce^{3+} and Dy^{3+} ions decreases, so the measurements were only made by using filter.

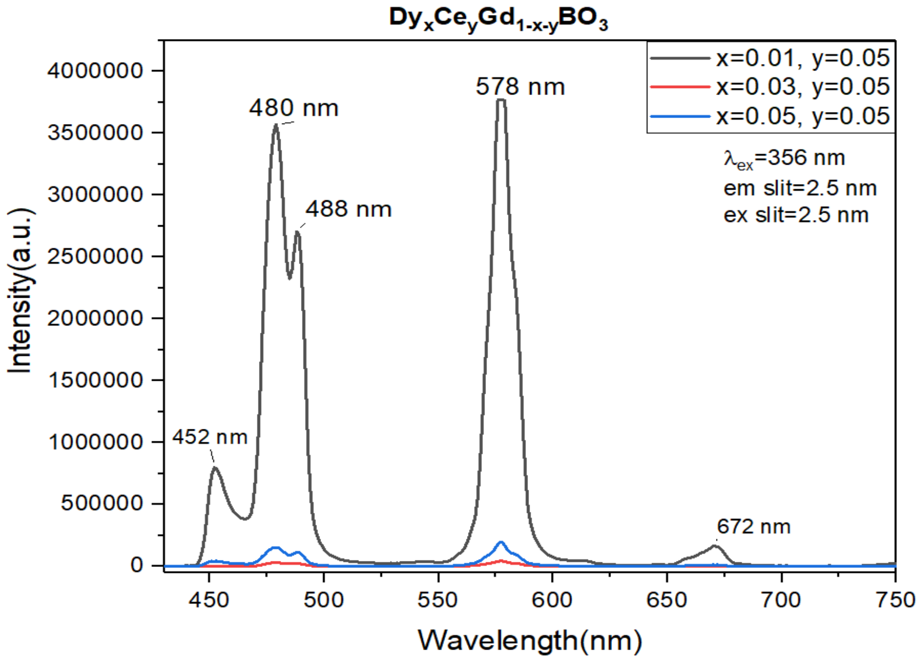

Figure 3.41. Emission spectra of 5% Ce^{3+} fixed and Dy^{3+} doped with changing concentration at 356 nm

Before these concentration studies, it is proved that the excitation at 356 nm gives the best results in terms of photoluminescence intensity. Besides, in this part, 356 nm excitation was only examined. Moreover, the energy transfer between ions was not effective, so the non-filtered measurements were not made. The concentration Ce^{3+} was increased; there is a significant decrease in both of the emissions of Dy^{3+} and Ce^{3+}. (**Figure 3.41**) The main reason for these results is the crystal structure of the $GdBO_3$. The crystal structure is very compact, and the dopant ions can place each other's position. Since the concentration of dopants is shallow in the structures, this changing or a different effect in the structure could not be observable.

It is expected that the most significant emission has to be at a concentration of 5% Ce^{3+} and 3% Dy^{3+}. However, a significant decrease occurred for both of the emission of dopants. Besides, if the compound, which has the most intense emission, is considered, the discharge of Dy^{3+} decreased.

Although a difference emerged for the emission of Dy^{3+}, the same trend was observed with this excitation wavelength. The increase in the concentration of Ce^{3+} caused a decrease in the emission of $Ce^{3+,}$ and it is assumed that the energy transfers between Ce^{3+} and Dy^{3+} are affected by this increase. In this experiment set, as it is seen clearly, the best concentration is 1% Dy^{3+} and %5 Ce^{3+}.

Therefore, if this photoluminescence information is used, the best concentration is 1% Dy^{3+} and 3% $Ce^{3+,}$ and it can be said that the intensity of emission at 578 nm increase by six times by adding three percent of cerium ion. Since the measurements of Dy^{3+} doped and Dy^{3+}-Ce^{3+} codoped compounds were made with different slits, there had to be different calculations for increasing intensity. (In ‘Appendix’ part) After these measurements, the best concentration for Ce^{3+} Dy^{3+} energy transfer was chosen, and another dopant was added to this best combination. The results of these measurements were given in **Figure 3.42**. Since the emission of Ce^{3+} ions did not occur in these measurements, emission filtered before 450 nm in the following measurements.

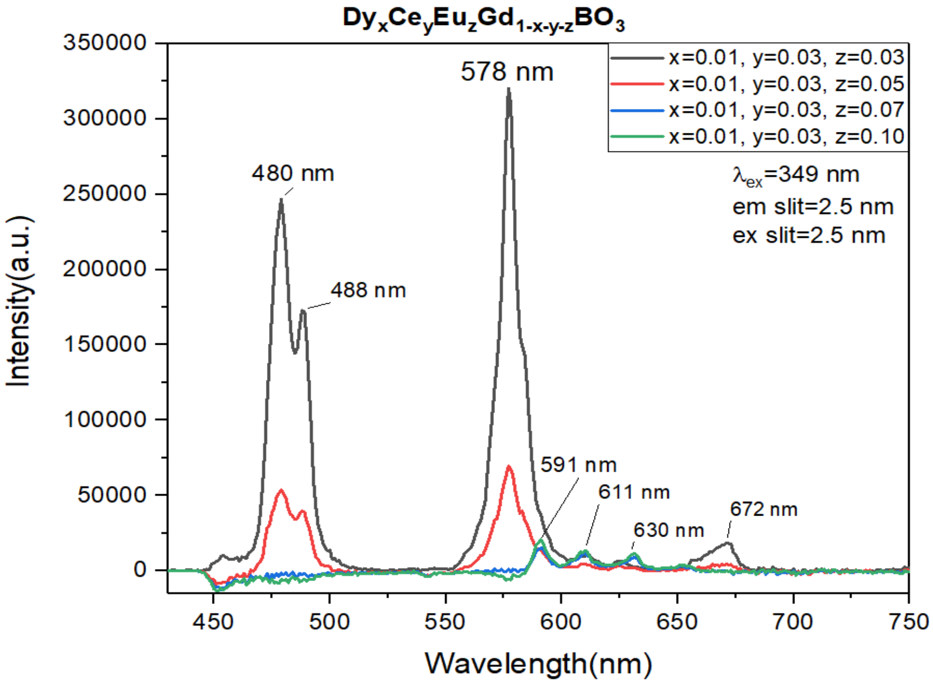

Figure 3.42. Emission spectra of 1% Dy^{3+}, 3% Ce^{3+} doped and Eu^{3+} doped $GdBO_3$ with changing Eu^{3+} concentration at 349-nm excitation

In these spectra (**Figure 3.42**), there was no apparent increase in europium emission, but the emission of europium was seen. For emission increase, Ce^{3+}-Dy^{3+} and Dy^{3+}-Eu^{3+} energy transfers were aimed. Because of that reason, firstly, synthesized compounds were excited with cerium excitation wavelength. On the next spectra, the excitation wavelength of dysprosium was used.

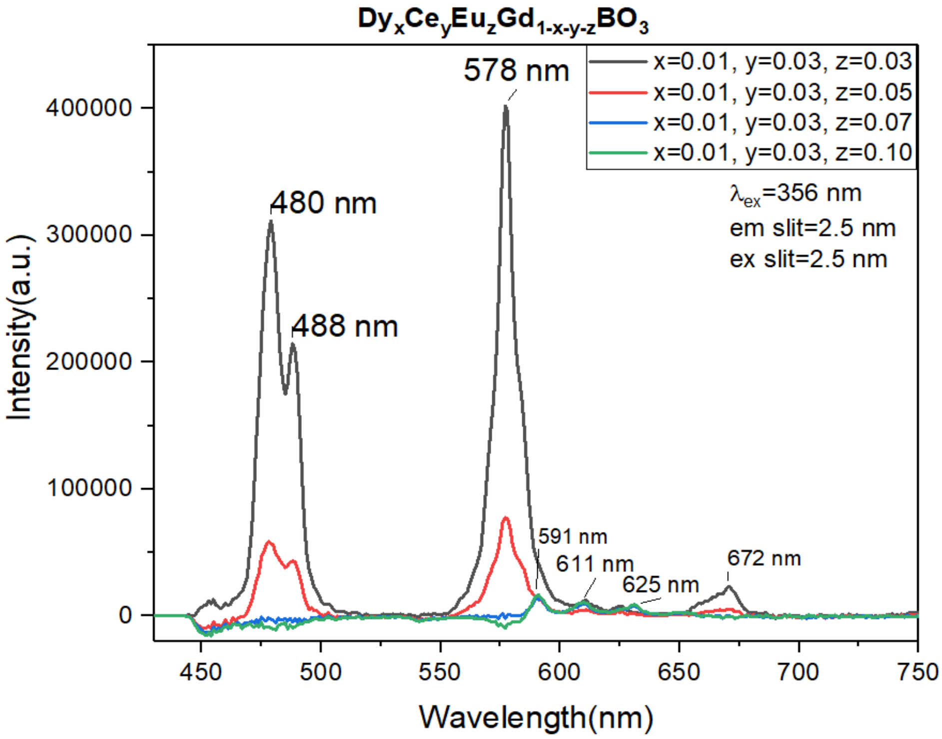

Figure 3.43. Emission spectra of 1% Dy^{3+}, 3% Ce^{3+} doped and Eu^{3+} doped $GdBO_3$ with changing Eu^{3+} concentration at 356-nm excitation

In these spectra (**Figure 3.43**), also, there was no increase in the emission of europium; however, measurable europium emission occurs. It can be said that dysprosium-europium energy transfer emerged, but it was not as effective as expected. Lastly, compounds were excited with 392-nm light, and the results are given.

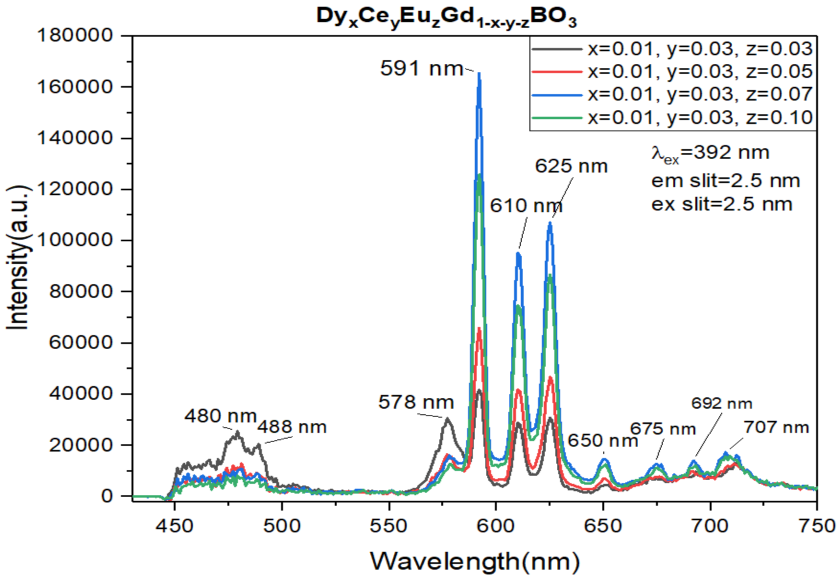

Figure 3.44. Emission spectra of 1% Dy^{3+}, 3% Ce^{3+} doped and Eu^{3+} doped $GdBO_3$ with changing Eu^{3+} concentration at 392-nm excitation

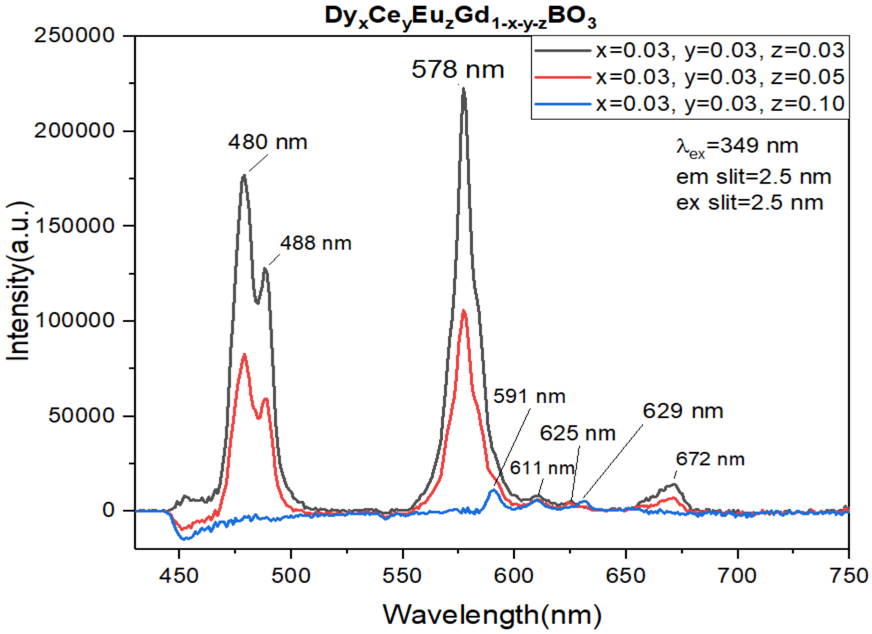

Figure 3.45. Emission spectra of 3% Dy^{3+}, 3% Ce^{3+} doped and Eu^{3+} doped $GdBO_3$ with changing Eu^{3+} concentration at 349-nm excitation

Moreover, a different concentration study was made to increase the effectiveness of dysprosium-europium energy transfer. For this purpose, the concentration of dysprosium increased to three percent, and emission spectra of synthesized compounds were given in **Figure 3.44**.

In **Figure 3.45**, emission of Eu^{3+} was observable only at 3% Dy^{3+}, 3% Ce^{3+} and 10% Eu^{3+} doping. Some of the energy was transferred from Dy^{3+} ions to Eu^{3+}. Predicted emissions were observed.

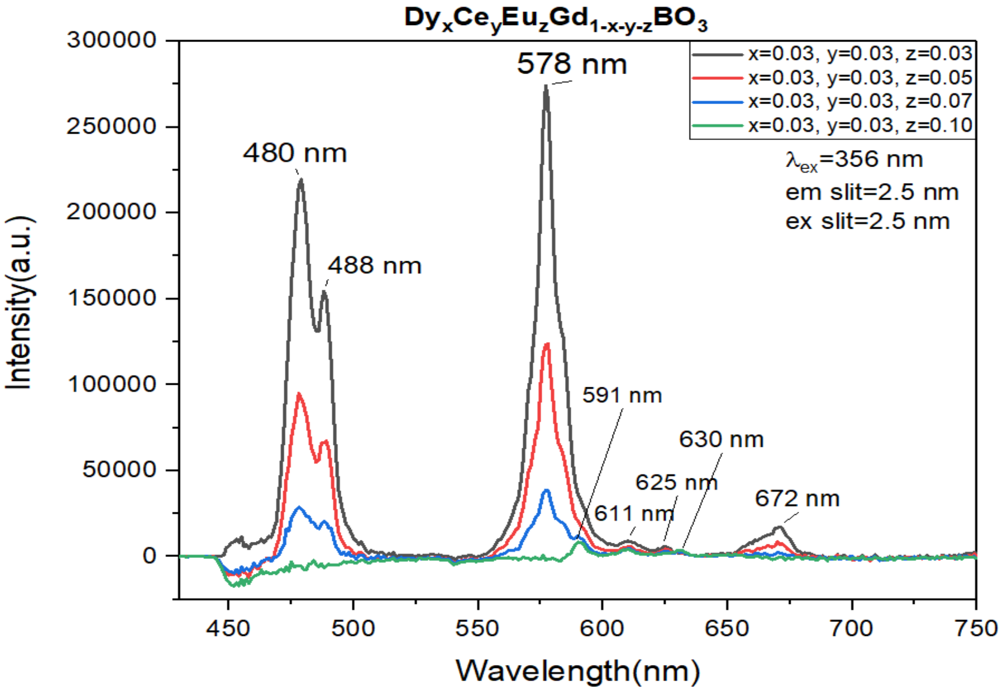

Figure 3.46. Emission spectra of 3% Dy^{3+}, 3% Ce^{3+} doped and Eu^{3+} doped $GdBO_3$ with changing Eu^{3+} concentration at 356-nm excitation

With these measurements given in **Figure 3.46**, it was aimed to observe Ce^{3+}-Dy^{3+}-Eu^{3+} energy transfer, and only some amount of energy was transferred to the last dopant. The effect of the transferred energy can be observed at 3% Dy^{3+}, 3% Ce^{3+}, and 10% Eu^{3+} doping. However, energy transfer was not as effective as desired.

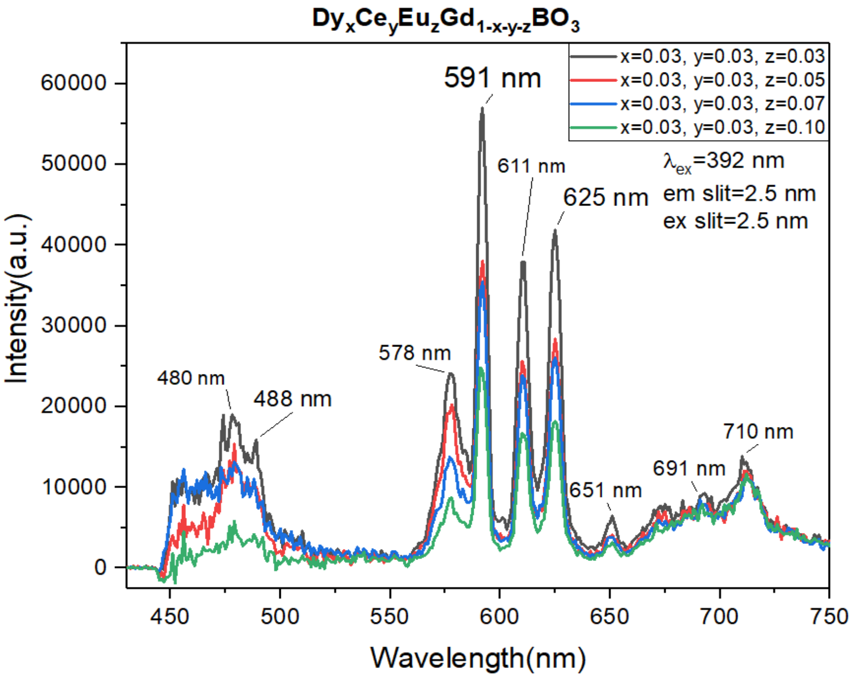

Figure 3.47. Emission spectra of 3% Dy^{3+}, 3% Ce^{3+} doped and Eu^{3+} doped $GdBO_3$ with changing Eu^{3+} concentration at 392-nm excitation

In these spectra shown in **Figure 3.47**, the effect of triple doping in Eu^{3+} emission and Eu^{3+} emission was decreased with the addition of other dopants. Since it was found that the best energy transfer between Ce^{3+} and Dy^{3+} at % Dy^{3+}-3%Ce^{3+}, the concentration of Eu^{3+} decreased to 1% in terms of molar percentage. The measured spectra of pure $GdBO_3$, 1% Eu^{3+} doped, and triple doped compound with 1% Eu^{3+} doped compound were given. For triple doped compound, the excitation wavelength is 356 nm. At high concentrations, the emission of Eu^{3+} could not be increased. The main reason for that is that the host material includes very high concentration dopants, decreasing the energy transfer between the dopants. As it was mentioned for Eu^{3+} single doped compounds, an extra phase affects the emission of the Eu^{3+} ion. It positively affects a single doped compound, but it affects the energy transfer between the other ions.

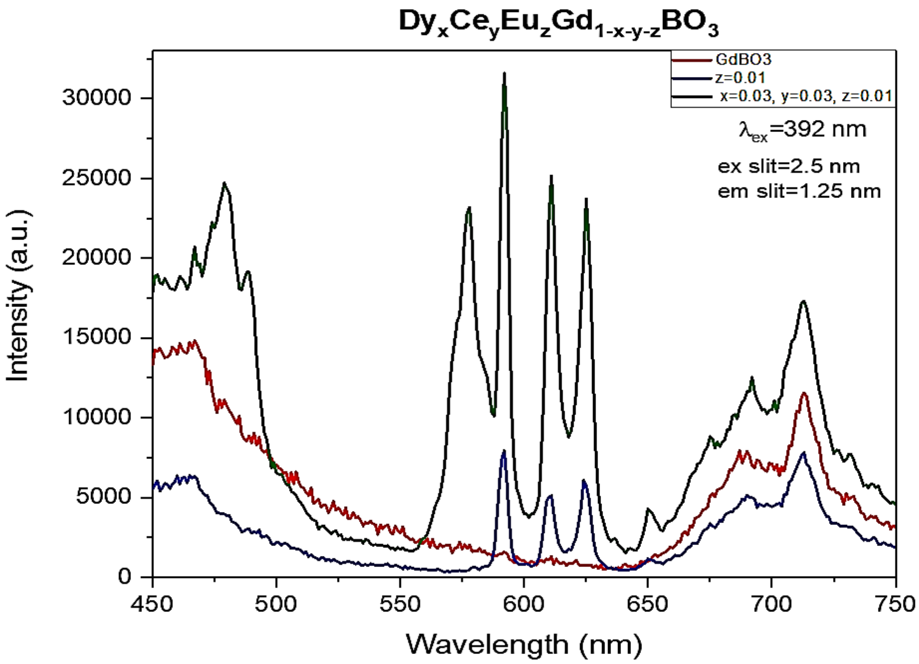

Figure 3.48. Emission spectra of 3% Dy^{3+}, 3% Ce^{3+} doped and 1% Eu^{3+} doped $GdBO_3$, 1% Eu^{3+} at 356-nm and undoped $GdBO_3$ at 392-nm excitation.

In this spectra (**Figure 3.48**), it may be seen that although the total energy transfer between ions was not appropriately achieved, the emission of Eu^{3+} increased by three-fold by adding cerium and dysprosium dopants at very few concentrations.

For some of the spectra, emission of Ce^{3+} could not be observed by using a 450 nm long-pass filter (emission filter). For that reason, the emission of Ce^{3+} ion was taken by using 331 and 356 nm excitation without a filter. The taken measurements are given in the Appendices section.

3.4.2 Photoluminescent Properties of $Tb_xCe_yYb_zGd_{1-x-y-z}BO_3$

In this part of the study, the desired compounds were predicted as showing two photoluminescent properties: downconversion and upconversion. Therefore, both of the features were given in two separate headings.

3.4.2.1 Downconversion Property

In this part of the study, since Ce^{3+} single doped compounds were examined for the other part of the research and Tb^{3+} doped were examined in the previous research made by our group(Akman et al., 2020), these studies were not given here. In this study, the best concentration for the most intense emission is 5% Ce^{3+} and 5% Tb^{3+}. Therefore, the emission of compounds with changing Yb^{3+} concentration is given in **Figure 3.42**.

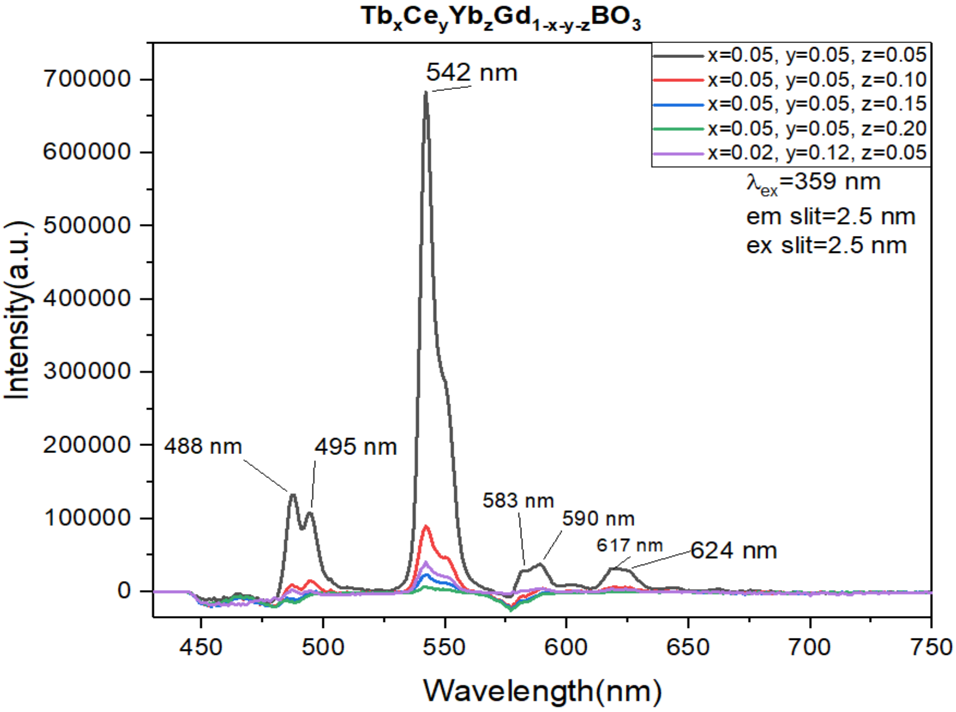

Figure 3.49. Downconversion photoluminescence spectra of triple doped $GdBO_3$

In **Figure 3.49**, the downconversion property of triple doped gadolinium borates is represented. Since the best emissive concentration of Ce^{3+}/Tb^{3+} codoped particles was known according to our group's previous study, only Yb^{3+} doping was examined by changing its concentration. However, the concentration of the ion increased, downconversion property of the doped gadolinium borates was lost. Although the best concentration of codoping is known, a concentration change was made for observing the effect of the amount of terbium. In this trial, also, the downconversion property was lost; therefore, the best concentration for green emission with conversion is still 5% Ce^{3+}, 5% Tb^{3+}, and 5% Yb^{3+}, as represented in these spectra. In the next section, the upconversion property of two synthesized compounds will be given.

3.4.2.2 Upconversion Property

Since the third dopant is Yb^{3+}, it is expected that there has to be an upconversion property of the desired product, and it was studied under the 980-nm laser. The same products were used for the investigation of upconversion property, and the results were given in **Figure 3.40**.

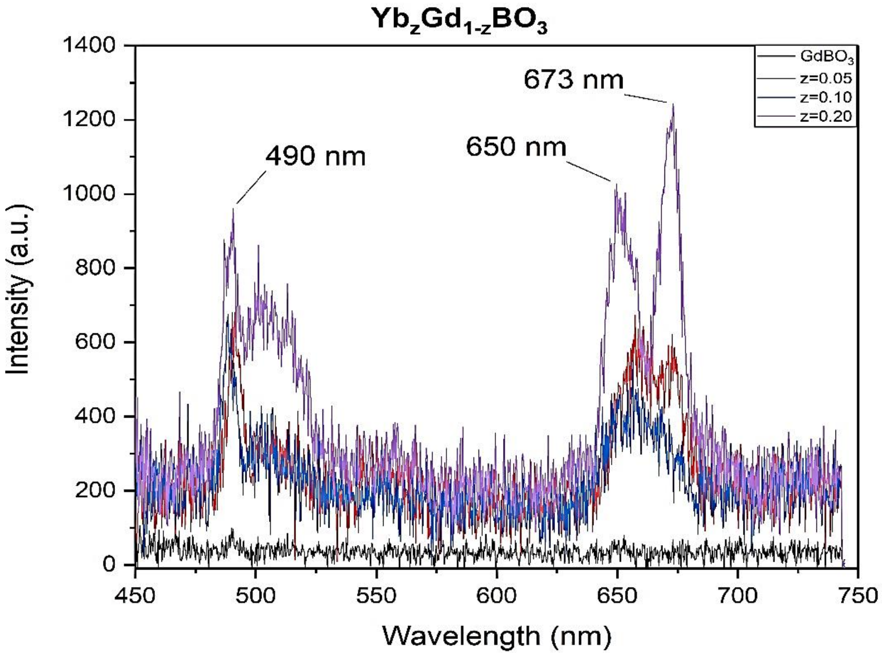

Figure 3.50. Upconversion Photoluminescence spectra of Yb^{3+} with changing concentration

First, single Yb^{3+} doped $GdBO_3$ compounds were measured with the laser, and the spectra were given below. For these measurements, the positions of some of the samples were changed to take better results. This procedure was made because the upconversion measurements were made with a handmade instrument.

As it is observed above, there can be a minimal effect of adding Yb^{3+} to the structure of $GdBO_3$. The emission at 490 nm is the result of the second harmonic generation process, and the other two emissions are because of the virtual states, which were explained in the ‘introduction’ part. 20% mole concentration is the best for the upconversion property; however, it is crucial to observe the downconversion property; therefore, the best concentration to keep both of the features is 5% in terms of mole. (**Figure 3.51**)

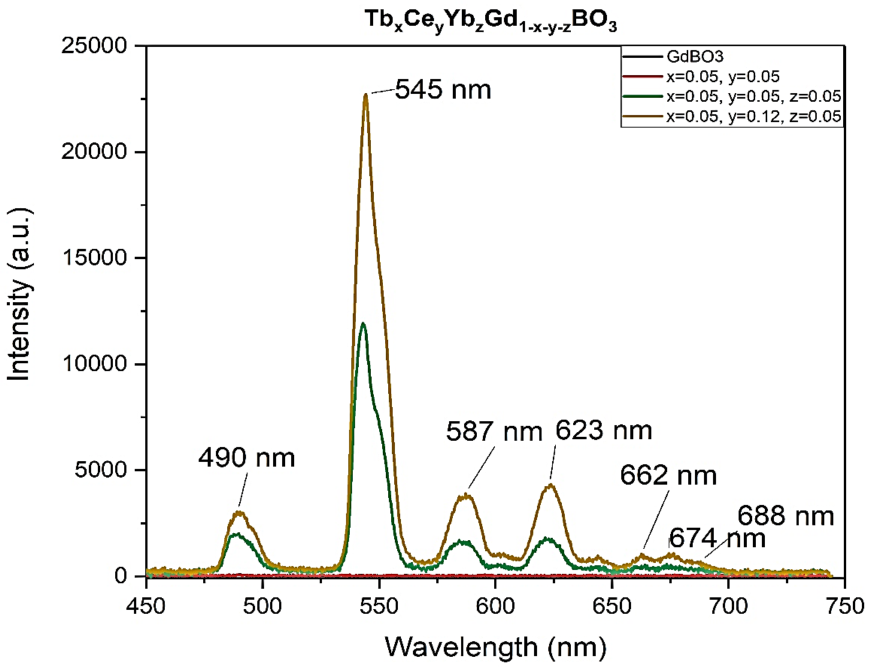

Figure 3.51. Upconversion photoluminescence spectra of triple doped $GdBO_3$

Changing the concentration was useful for upconversion; however, this decreased the downconversion photoluminescence. Therefore, the compound, which has both of the properties, was 5% Ce^{3+}, 5% Tb^{3+}, and 5% Yb^{3+}.

3.4.3 Comparison of Photoluminescence Properties of Gadolinium Borate Phosphors Synthesized with Two Different Methods

For this comparison, the sol-gel method and microwave-assisted solid-state method were used. The sol-gel method was explained in ‘Materials and Methods chapter. The microwave-assisted method is very different from sol-gel. In this method, solid materials were ground and mixed in an agate mortar with solid fuel (in this synthesis urea) for the occurrence of the formation reaction, and the precursors are exposed to microwaves for 5 minutes with the power of 360 W. The resulting mixture was transferred to a crucible, and it was heated to 900 °C for 4 hours.

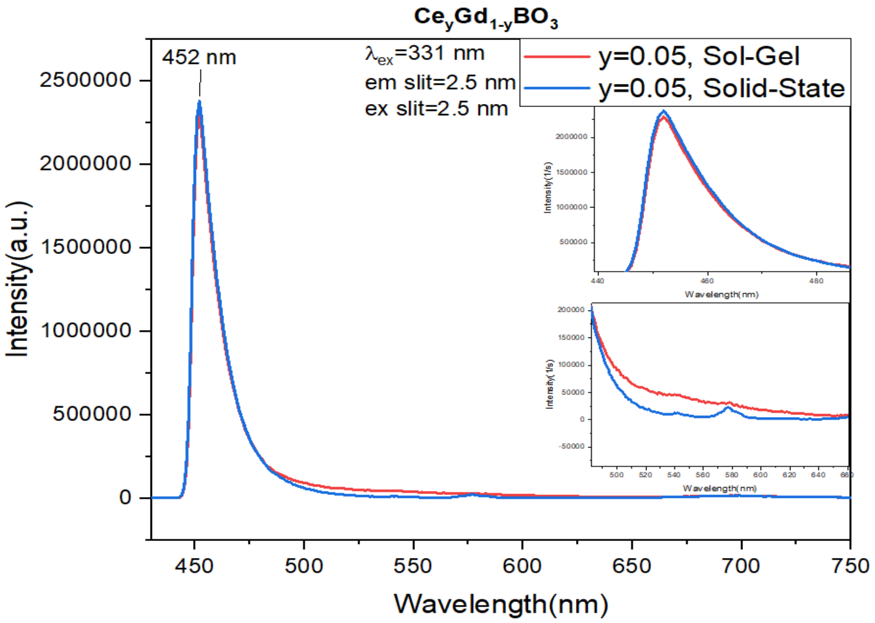

Figure 3.52. Emission spectra of 5% Ce^{3+} doped GBO_3 synthesized with sol-gel and microwave assisted solid-state methods

For this purpose, the compound, which has the highest intensity, was used. 5% Ce^{3+} doped $GdBO_3$ phosphors for the comparison of single doped $GdBO_3$ had the best intensity without considering the wavelength of emitted light. The spectra (**Figure 3.52**) shows that the emission of synthesized does not change with changing synthesis method for the single doped compound.

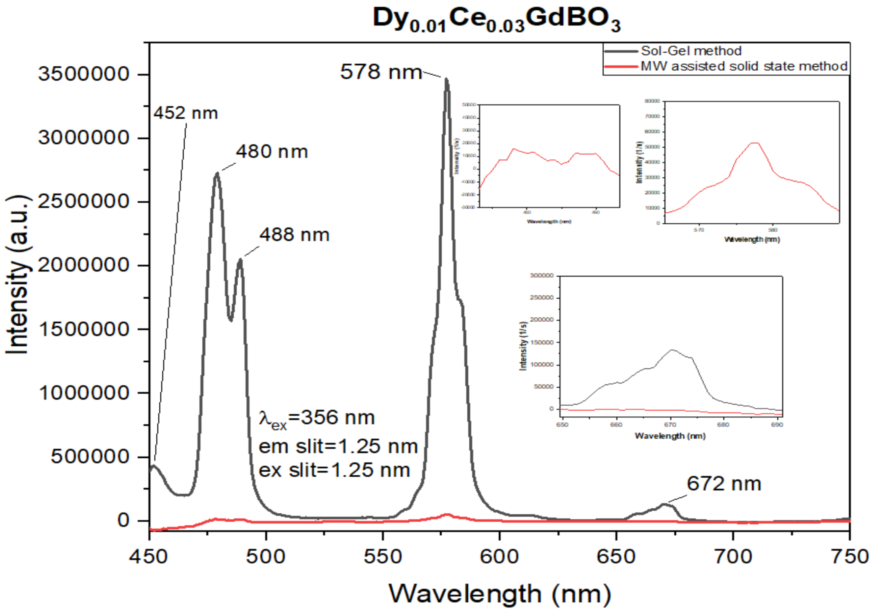

Figure 3.53. Emission spectra of the 1% Dy^{3+}-3% Ce^{3+} codoped $GdBO_3$ synthesized with sol-gel and microwave assisted solid-state method at 356 nm

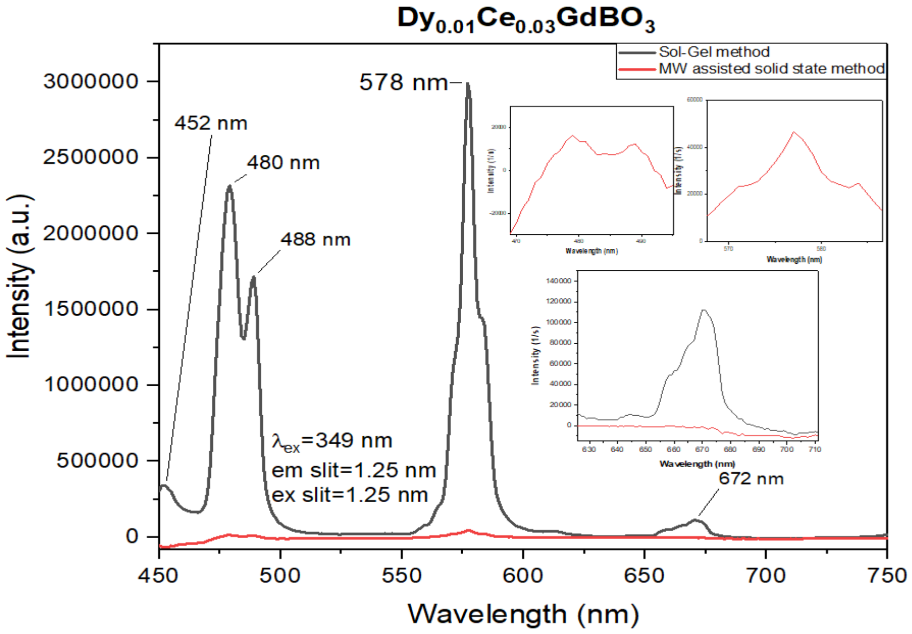

Figure 3.54. Emission spectra of the 1% Dy^{3+}-3% Ce^{3+} codoped $GdBO_3$ synthesized with sol-gel and microwave assisted solid-state method at 349 nm

In these spectra (**Figure 3.53** and **Figure 3.54**), a comparison of two different synthesis methods, which are sol-gel and microwave-assisted solid-state, was presented by means of photoluminescence intensity. These are the spectra of 1%Dy^{3+} and 3% Ce^{3+} codoped compounds. Although there was no difference in the luminescence, the intensity of single doped compounds, for codoped compounds, the sol-gel method synthesized one gives very high intensity. The reason for that result is that energy transfer between activator and sensitizer ions is much more easily than the microwave-assisted method.

3.4.4 Photoluminescence Decay Lifetime Measurements

In this part of the study, as it is mentioned in the ‘Materials and Methods’, the light source of the instrument is only a photon source with a wavelength of 365 nm. Therefore, a lifetime of $Dy_xCe_yEu_zGd_{1-x-y-z}BO_3$ compounds can be made according to their emission intensity. Only the Ce^{3+} single doped $GdBO_3$ was measured in the time interval of 10 ms. The other compounds were examined in the time interval of 40 ms. The results of these measurements are given in the following section.

3.4.4.1 Photoluminescence Decay Lifetime Measurements of $Dy_xCe_yEu_zGd_{1-x-y-z}BO_3$

For calculation of decay lifetimes, both single and double exponential function fitting were used. The valid values for these are chosen with the help of the correlation number (R) of each fitting results. Since the light intensities of Dy^{3+} single doped $GdBO_3$ are very low, the decay lifetime measurement is not applicable to these. Therefore, single doped Ce^{3+} and Eu^{3+} phosphors give measurable values, so only the results of them delivered since a 980-nm laser was needed for the measurement. Then, only Ce^{3+}/Dy^{3+} codoped phosphor is provided since Ce^{3+}/Tb^{3+} was examined by means of decay lifetime in the previous study. For the result of triple doped phosphor $Ce^{3+}/Dy^{3+}/Eu^{3+}$ doped is given on the other hand because of the reason which Yb^{3+} single doped sample was not given, the examined lifetime of Ce^{3+}/Tb^{3+}/Yb^{3+} cannot be granted. Firstly, the decay lifetime result (**Figure 3.48**) of Ce^{3+} doped phosphor is explained.

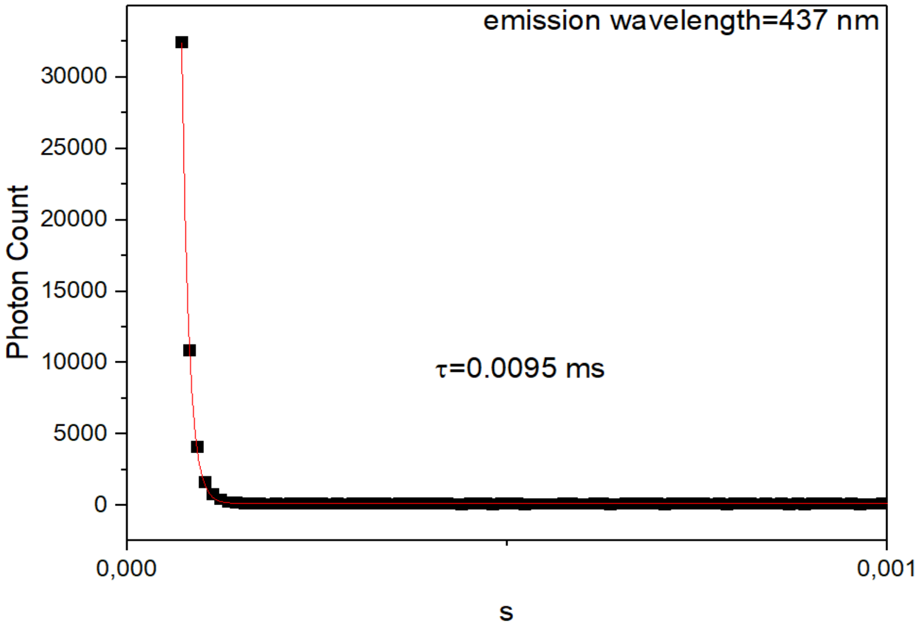

Figure 3.55. Decay curve of 5% Ce^{3+} doped $GdBO_3$

The decay curve was taken with the emission of 437 nm. **Figure 3.55** indicates the decay curve of 5% Ce^{3+} doped $GdBO_3$ with decay time t= 0.09532 ± 1.877x10^{-4} ms. The decay of the compound is well fitted with a single exponential function. This fitting refers to a structure that Ce^{3+} ion occupies one site of the crystal structure. Another factor that affects this result is very fast decay since Ce^{3+} ion is very effective in the $GdBO_3$ structure. Besides, some of the recent studies show that the decay time of Ce^{3+} can change between 30-40 ns (Isokawa et al., 2018)(Y. Wu et al., 2019), and our result shows that the decay time is 95.3 µs. This short decay time is important for some applications, such as scintillators. (Y. Wu et al., 2019)

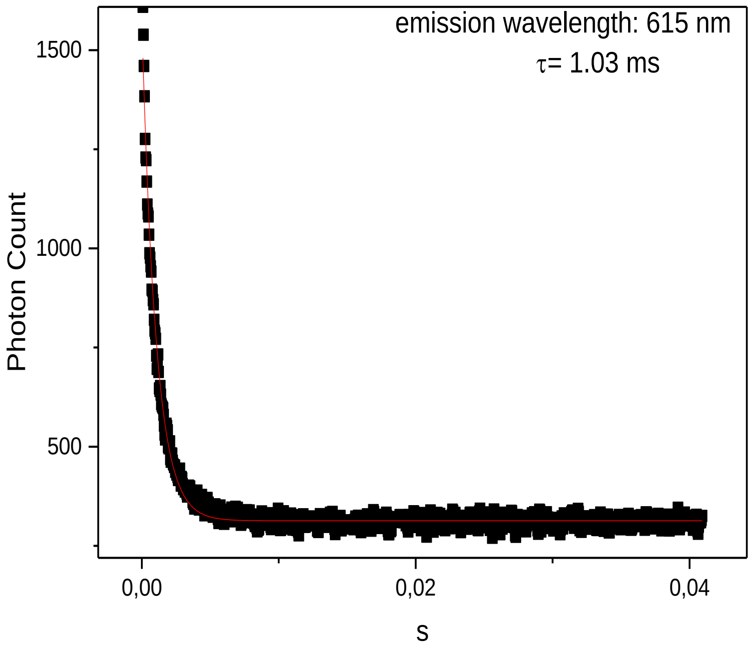

Figure 3.56. Decay curve of 7% Eu^{3+} doped $GdBO_3$

The decay time of the compound was taken with an emission wavelength of 615 nm (**Figure 3.56**). The used phosphor for the measurement is 7% Eu^{3+} doped $GdBO_3$. The reason why 7 mole percentage Eu^{3+} doped $GdBO_3$ was used is that it has the best emission intensity. The decay curve fits with the single exponential function. The decay time of the compounds is $t=1.03 \pm 8.32845 \times 10^{-3}$ ms. In recent studies, most of the decay times were given in the microseconds range (490-560 microseconds) (Lapaev et al., 2020). On the other hand, one of the most extended decay times is 2 ms (Lapaev et al., 2020) and 5.71 ms (Vu, Bondzior, Stefanska, Miniajluk, & Deren, 2020), and this indicates that a significant increase in the decay time of Eu^{3+} ion.

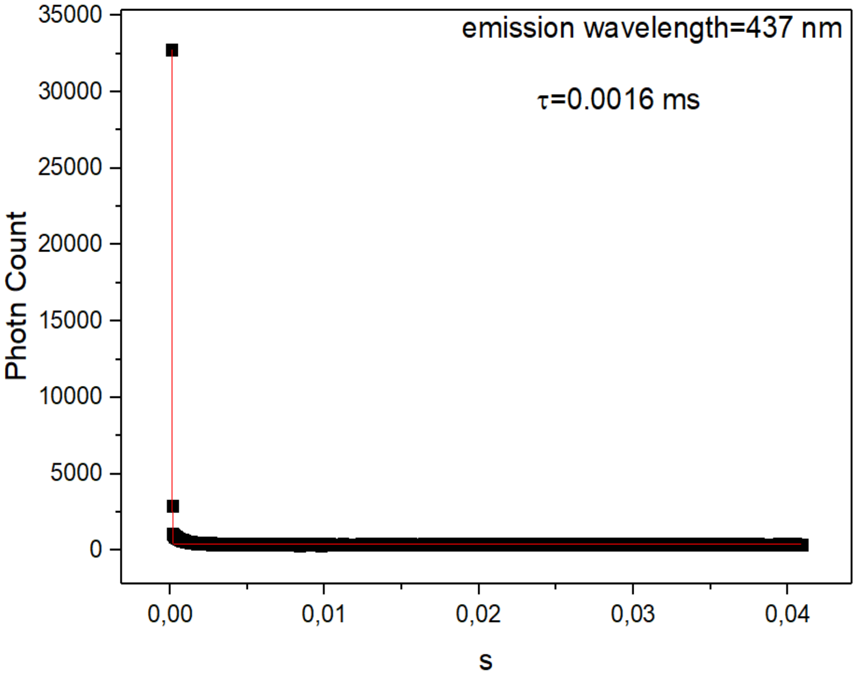

Figure 3.57. Decay curve of 1% Dy^{3+}/3% Ce^{3+} doped $GdBO_3$ at 437 nm

For the observation of the decay curve of Dy^{3+}/Ce^{3+} doped $GdBO_{3,}$ the concentration of Dy^{3+} was chosen as 1%, and the concentration of Ce^{3+} was selected as 3% (mole percentage), which are the best concentration of the emission of the codoped samples (**Figure 3.57**). The first curve is the emission of the sample at the wavelength of 437 nm, and the decay curve at this wavelength was fitted to the single exponential function, and the decay lifetime of the phosphor was found as $t=0.01623\pm 1.56\text{x}10^{-4}$ ms. In addition, it is obviously seen that the decay time increased; on the other hand, the emission intensity decreases by means of photon count. The reason for this is the energy transfer from Ce^{3+} to Dy^{3+} ion, which is the desired result. With the help of this energy transfer, an emission and its decay lifetime can be measured. The decay curve of that emission is given.

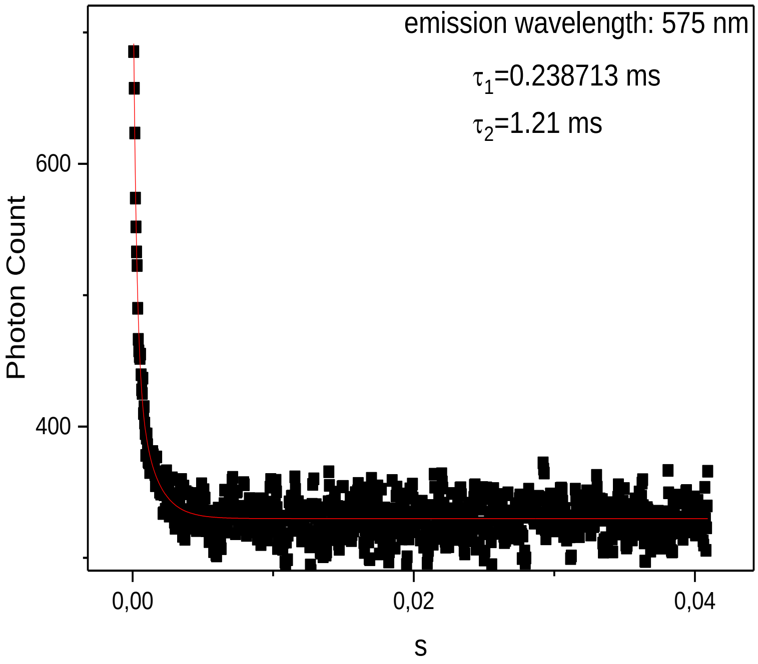

Figure 3.58. Decay curve of 1% Dy^{3+}/3% Ce^{3+} doped $GdBO_3$ at 575 nm

The decay curve of the emission at 575 nm, which is the main emission line of Dy^{3+}, was fitted to the double exponential function, and the fast and slow decay of the sample was calculated as t_1=0.238713±0.032397 ms and t_2=1.21± 0.63 ms (**Figure 3.58**). Therefore the average decay lifetime is 0.72 ms. In the literature, In recent studies, according to Chengaiah et al. (Chengaiah, Kiran Kumar, & Rama Moorthy, 2018), the decay time of Dy^{3+}ion is 0.77 ms in $Na_3Gd(PO_4)_2$ host. According to Khan et al. (Khan et al., 2019), the decay time was observed as 0.72 ms in Li_2O-BaO-Gd_2O_3-SiO_2 host. Therefore, our phosphor gave a comparable result with the literature.

For the triple doped phosphors, the emission intensity significantly decreased for both the emissions of Ce^{3+} ion and Dy^{3+} ion, and there is no measurable value exists for these ions. However, the radiation of Eu^{3+} was still measurable, and the result is given in **Figure 3.52**)

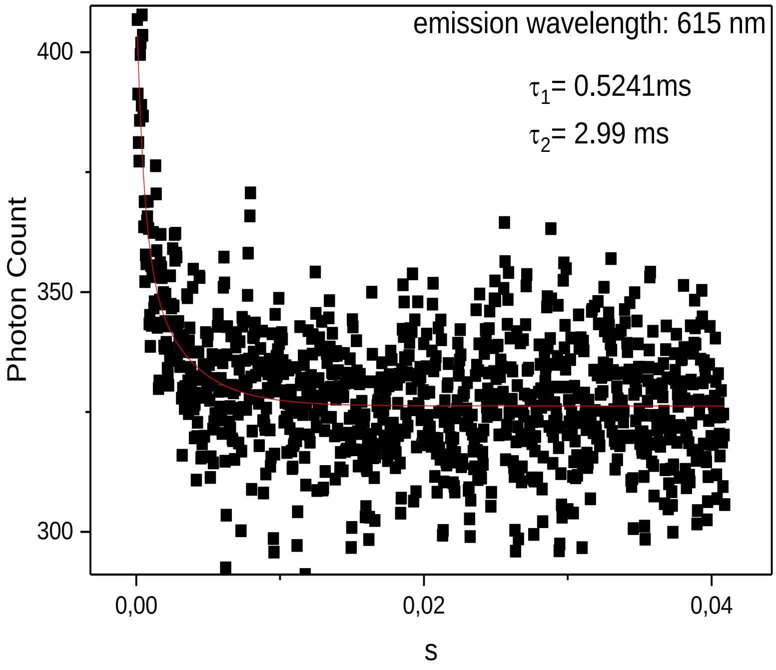

Figure 3.59. Decay curve of 1% Dy^{3+}/3% Ce^{3+}/7% Eu^{3+} doped $GdBO_3$ at the emission wavelength of 615 nm

In the case of triple doped $GdBO_3$, only the decay time of emission at 615 nm, which is the emission of Eu^{3+} ion, can be measured (**Figure 3.59**). The decay curve can be fitted with a double exponential function, and the values for the fast and slow decays are

t_1= 0.5241±0.22304 ms and t_2=2.99±0.82 ms. The average decay time is 1.75ms. Therefore, the decay time decreased at 615 nm. Although the time of decay decreased, it is still compatible with the compounds in the literature.

3.4.5 Quantum Efficiency Measurements

For quantum yield measurements, a handmade setup was used. A 365-nm laser was used as a source, and an integrating sphere is used as an apparatus for a detector. With the help of this apparatus, the absolute quantum yield of some of the synthesized phosphors was measured. The detector of the system was reliable for the range of visible light. Since there was no different source of light, which is a 980-nm light emitter, some of the samples could not be examined.

3.4.5.1 Quantum Efficiency Measurements of $Dy_xCe_yEu_zGd_{1-x-y-z}BO_3$

For gathering information on the quantum yield of samples, they have emitted very intense light at a specific wavelength. Because of that reason, some of the samples were inappropriate for this measurement. There two samples for examination of quantum efficiency measurement: $Ce_{0.05}Gd_{0.95}BO_3$ and $Dy_{0.01}Ce_{0.03}Gd_{0.96}BO_3$ phosphors. The results will be given in the following paragraphs.

For most of the phosphors, quantum yield is calculated smaller or equal to 100 percent; however, for $Ce_{0.05}Gd_{0.95}BO_3$, it is more significant than that value; the reason for this controversial result is that Ce^{3+} ion emits intense radiation in three different wavelengths with the excitation of 365-nm light. Therefore, these emissions have to be separated from each other. After a mathematical process, it was achieved, and these quantum efficiencies were calculated. This mathematical operation is curve fitting. The resulting emission spectrum was fitted to the 'Gaussian' function. The reason for this fitting process was the absorption and emission regions of Ce^{3+} ion overlapped to each other. The total region and separate regions were given in **Figure 3.60**.

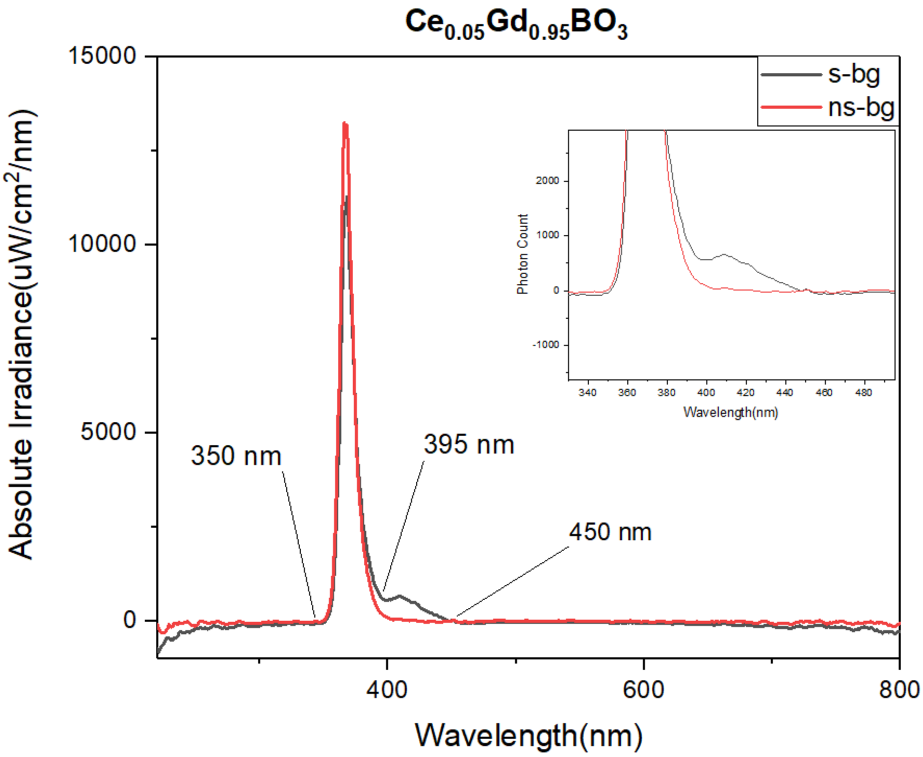

Figure 3.60. Absorption and emission regions used for the calculation of 0.05 Ce^{3+} doped (in terms of mole) doped $GdBO_3$

In calculation 350-395 nm region was used as the absorption region. The difference between the regions of no-sample measurement (ns-bg) and sample (s-bg) gave the absorbed photon for the compound. In order to avoid the background (bg) effect, the measurement of without any light source was used for subtraction because of photons from the experimental environment. This subtraction was also made for the calculation of the codoped compound. Gaussian fitted spectra, and their parameters were given in **Figure 3.61** and **3.62**. As it is seen in the figures, the absorption region spreads to nearly 410 nm when the fitting is used. This region was added to the absorption region and subtracted from the emission region, and the quantum yield was found as 89.2%. Since the emission of Ce^{3+} ion centered at 380 and 408 nm absorption and emission line are gathered, and absorption value decreases. This affects the numerical value of quantum efficiency.

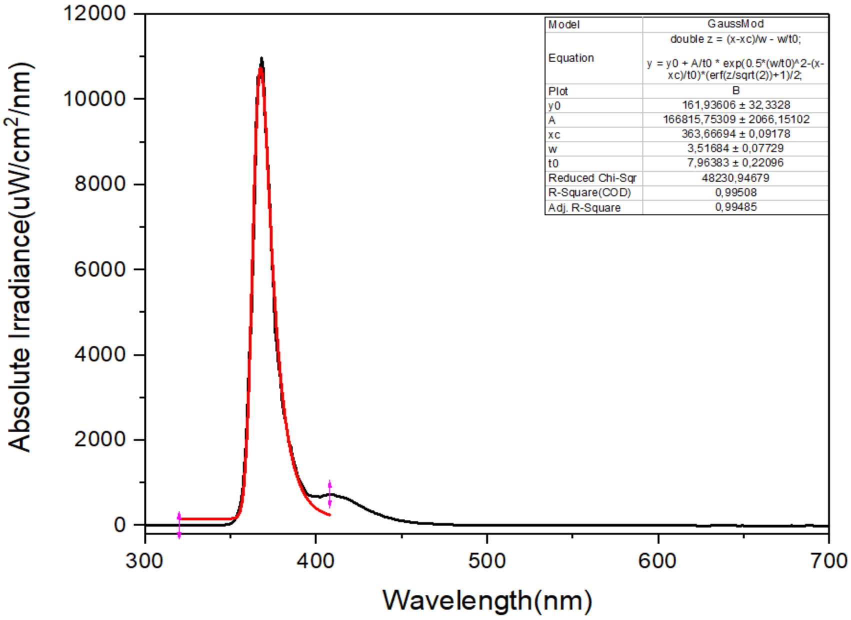

Model	GaussMod
Equation	double z = (x-xc)/w - w/t0; y = y0 + A/t0 * exp(0.5*(w/t0)^2-(x-xc)/t0)*(erf(z/sqrt(2))+1)/2;
Plot	B
y0	161,93606 ± 32,3328
A	166815,75309 ± 2066,15102
xc	363,66694 ± 0,09178
w	3,51684 ± 0,07729
t0	7,96383 ± 0,22096
Reduced Chi-Sqr	48230,94679
R-Square(COD)	0,99508
Adj. R-Square	0,99485

Figure 3.61. Absorption region used for the calculation of 0.05 Ce^{3+} doped (in terms of mole) doped $GdBO_3$

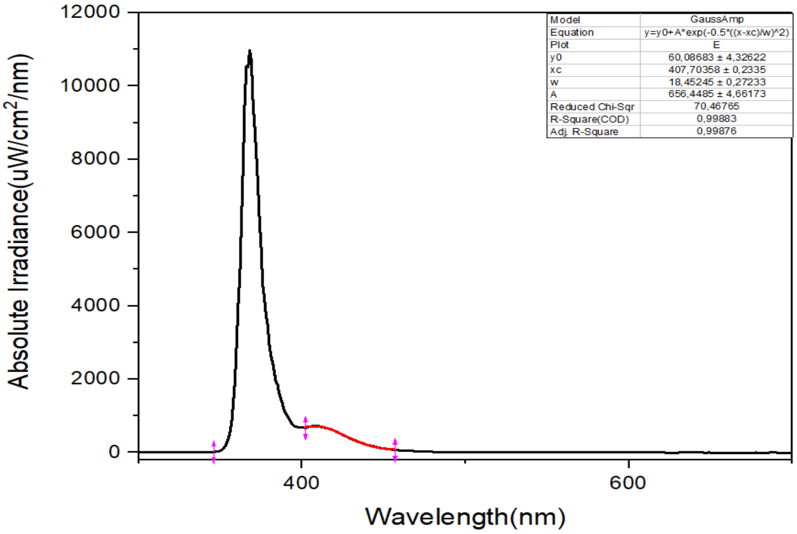

Model	GaussAmp
Equation	y=y0+A*exp(-0.5*((x-xc)/w)^2)
Plot	E
y0	60,08683 ± 4,32622
xc	407,70358 ± 0,2335
w	18,45245 ± 0,27233
A	656,4485 ± 4,66173
Reduced Chi-Sqr	70,46765
R-Square(COD)	0,99883
Adj. R-Square	0,99876

Figure 3.62. Absorption and emission regions used for the calculation of 0.05 Ce^{3+} doped (in terms of mole) doped $GdBO_3$

In addition, 1% Dy^{3+} and 3% Ce^{3+} doped $GdBO_3$ had measurable quantum efficiency. The spectra resulted from this measurement was given. The result was found as 4.3 percent. These results indicate that non-radiative relaxations released most of the radiative energy absorbed by Ce^{3+} ion, and the energy transfer efficiency is very low. The spectra were given in **Figure 3.63**.

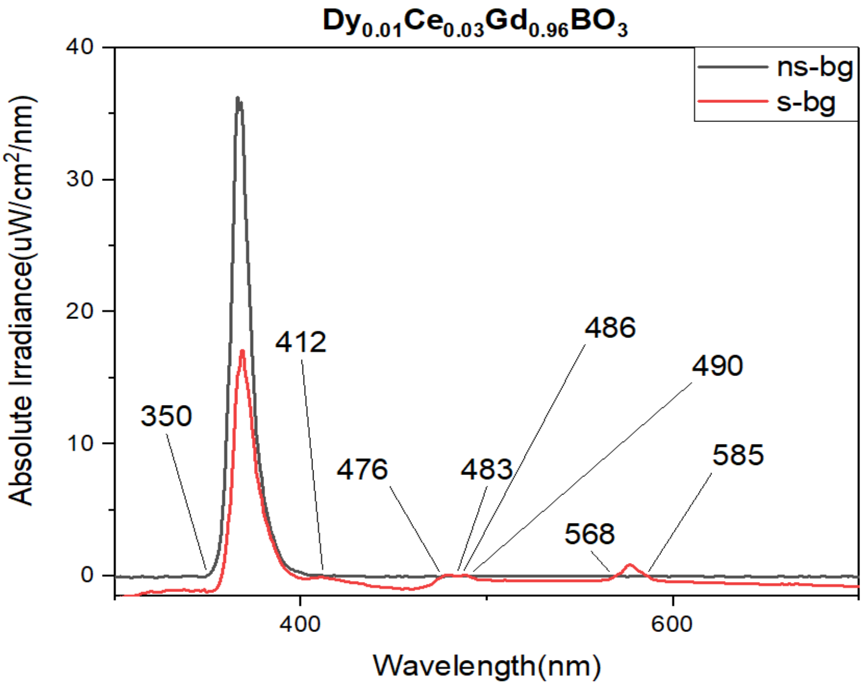

Figure 3.63. Absorption and emission regions used for the calculation of 0.01 Dy^{3+}-0.03 Ce^{3+} doped (in terms of mole)

For this calculation, there was no need for the fitting process. 350-412 nm was used for absorption and the other regions where the emission from the compound. The given quantum yield was the total quantum efficiency for all of the emission from the compound.

3.4.6 CIE Calculations

In this part of the study, the predicted colors of some of the synthesized compounds will be given. As it was mentioned before, CIE calculation was used for determining the color of the sample by an objective observer. For this calculation, a handmade calculation code and MATLAB program were used. Colorimetric calculations were made by using the filtered result of the compounds.

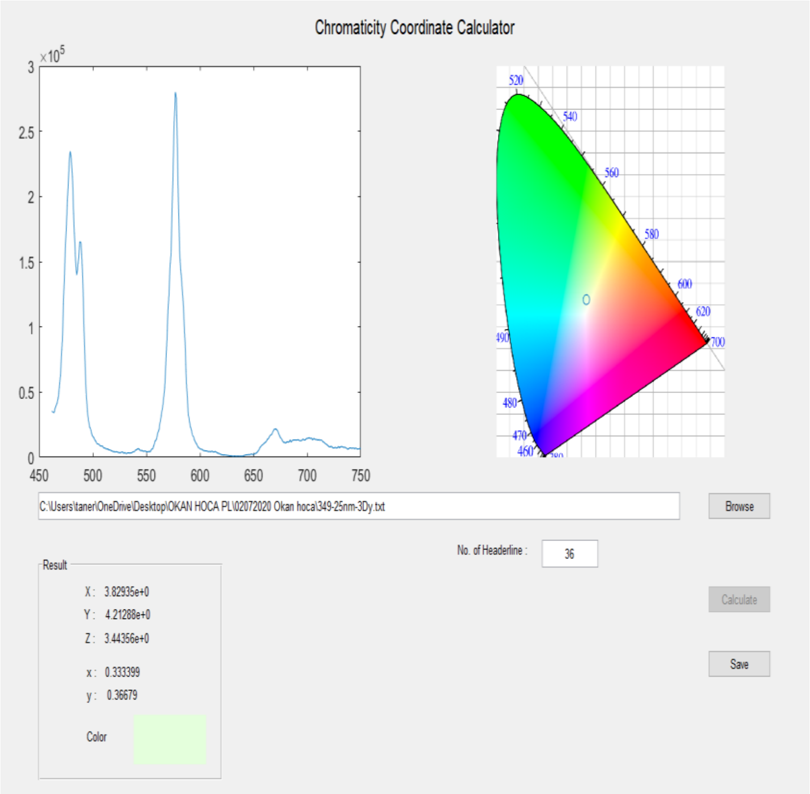

C:\Users\taner\OneDrive\Desktop\OKAN HOCA PL\02072020 Okan hoca\349-25nm-3Dy.txt

No. of Headerline : 36

Result

X : 3.82935e+0
Y : 4.21288e+0
Z : 3.44356e+0

x : 0.333399
y : 0.36679

Color 🟩

Figure 3.64. CIE calculation of 3% Dy^{3+} doped $GdBO_3$

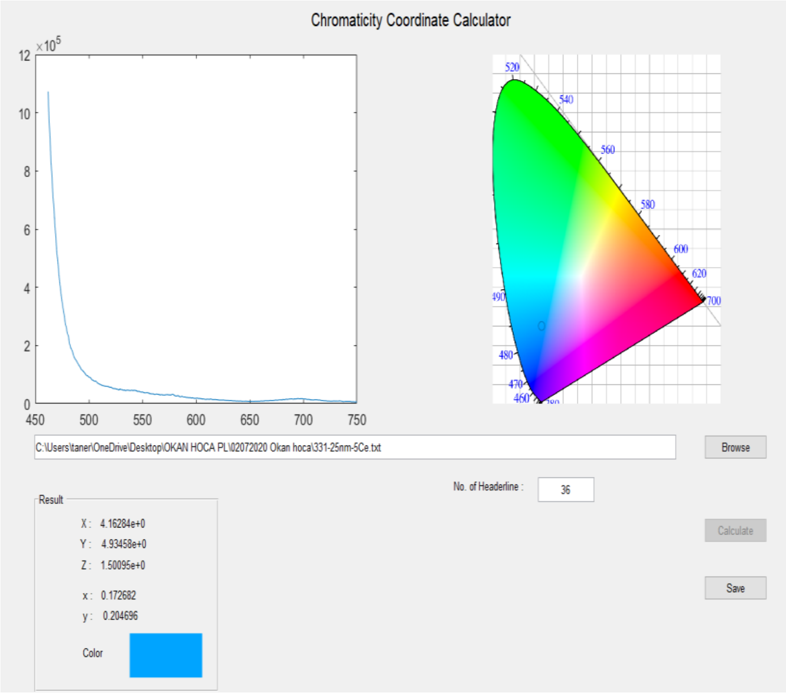

C:\Users\taner\OneDrive\Desktop\OKAN HOCA PL\02072020 Okan hoca\331-25nm-5Ce.txt

No. of Headerline : 36

Result

X : 4.16284e+0

Y : 4.93458e+0

Z : 1.50095e+0

x : 0.172682

y : 0.204696

Color 🟦

Figure 3.65. CIE calculation of 5% Ce^{3+} doped $GdBO_3$

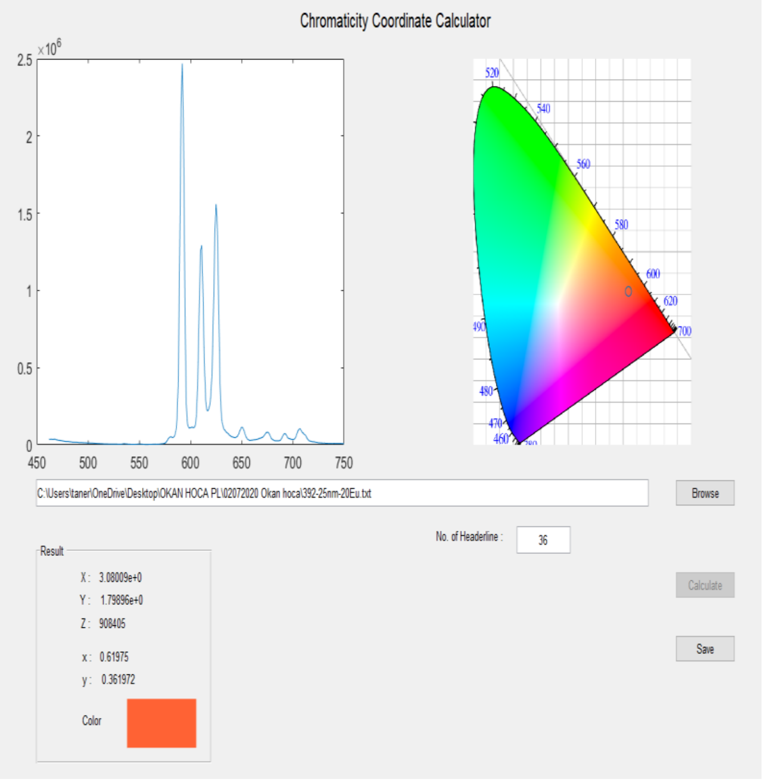

C:\Users\taner\OneDrive\Desktop\OKAN HOCA PL\02072020 Okan hoca\392-25nm-20Eu.txt

No. of Headerline : 36

Result

X : 3.08009e+0

Y : 1.79896e+0

Z : 908405

x : 0.61975

y : 0.361972

Color 🟧

Figure 3.66. CIE calculation of 20% Eu^{3+} doped GdBO3

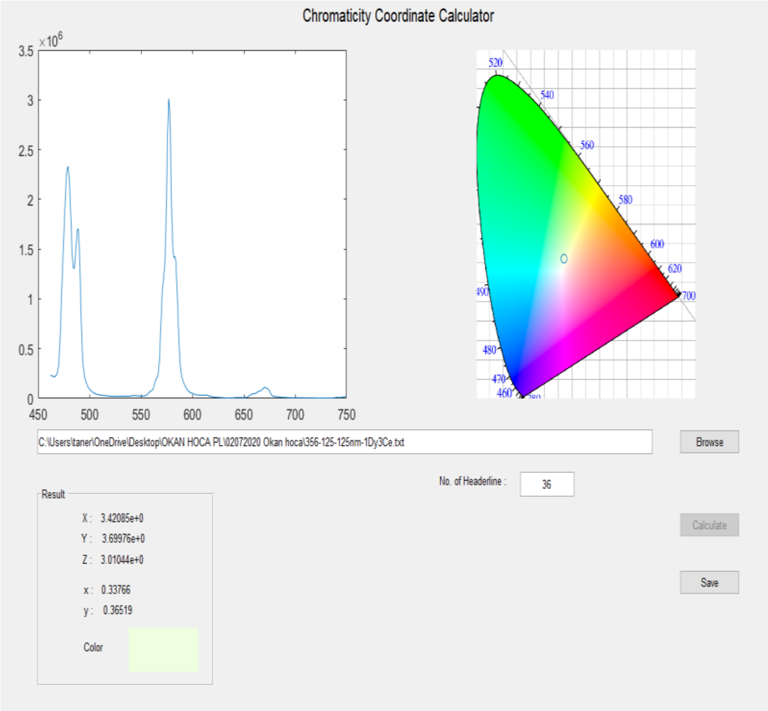

C:\Users\taner\OneDrive\Desktop\OKAN HOCA PL\02072020 Okan hoca\356-125-125nm-1Dy3Ce.txt

No. of Headerline : 36

Result

X : 3.42085e+0
Y : 3.69976e+0
Z : 3.01044e+0
x : 0.33766
y : 0.36519
Color

Figure 3.67. CIE calculation of 1% Dy^{3+}, 3% Ce^{3+} codoped $GdBO_3$

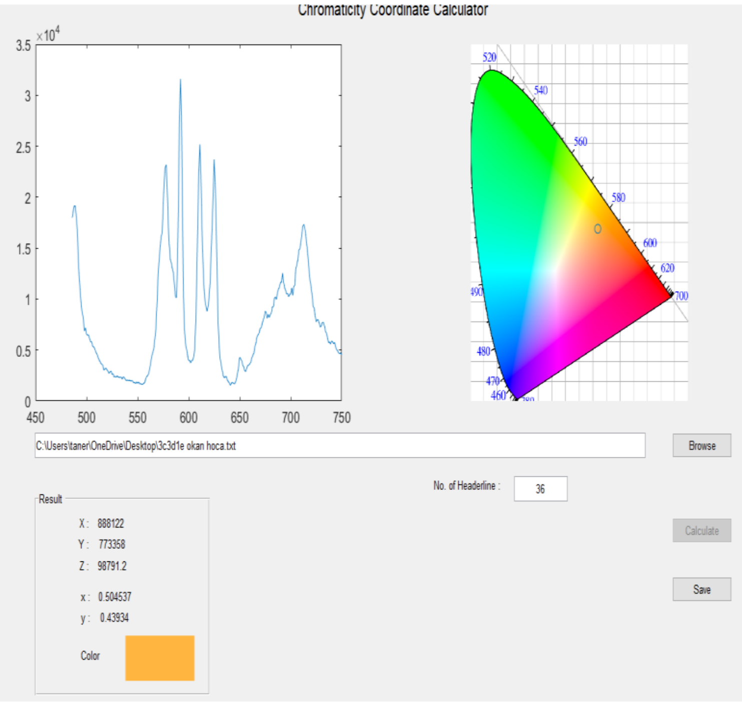

C:\Users\taner\OneDrive\Desktop\3c3d1e okan hoca.txt

No. of Headerline : 36

Result

X : 888122
Y : 773358
Z : 98791.2
x : 0.504537
y : 0.43934
Color

Figure 3.68. CIE calculation of 1% Dy^{3+}, 3% Ce^{3+}, 1% Eu^{3+} triple doped $GdBO_3$

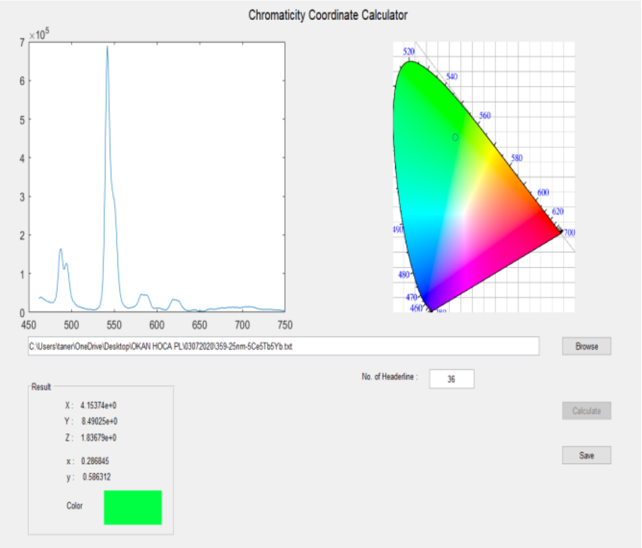

C:\Users\taner\OneDrive\Desktop\OKAN HOCA PL\03072020\359-25nm-5Ce5Tb5Yb.txt

No. of Headerline : 36

Result

X : 4.15374e+0
Y : 8.49025e+0
Z : 1.83679e+0

x : 0.286845
y : 0.586312

Color 🟩

Figure 3.69. CIE calculation of 1% Tb^{3+}, 3% Ce^{3+}, 1% Yb^{3+} triple doped $GdBO_3$ with downconversion

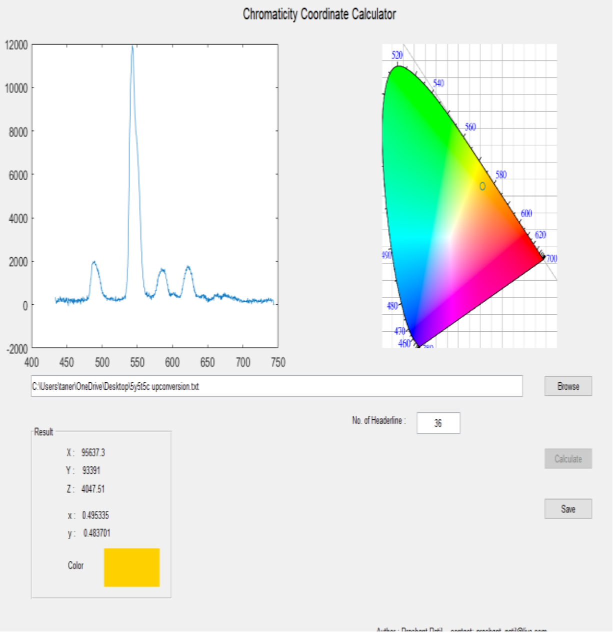

C:\Users\taner\OneDrive\Desktop\5y5t5c upconversion.txt

No. of Headerline : 36

Result

X : 95637.3
Y : 93391
Z : 4047.51

x : 0.495335
y : 0.483701

Color 🟨

Figure 3.70. CIE calculation of 5% Tb^{3+}, 5% Ce^{3+}, and 5% Yb^{3+} triple doped $GdBO_3$ with upconversion

In this part of the study, the colors of the best emissive compounds were given, and in the appendix part, the results of other compounds will be given.

CHAPTER 4

CONCLUSION

In this study, two types of triple doped gadolinium orthoborate phosphors were synthesized. For the production of undoped and doped gadolinium orthoborate phosphors, the sol-gel method was employed.

The observation of desired products was indicated by both X-Ray Diffraction and FTIR measurements. Recorded diffraction patterns of undoped Ce^{3+}, Dy^{3+}, Eu^{3+}, Yb^{3+}, Ce^{3+}/Dy^{3+} doped, $Ce^{3+}/Dy^{3+}/Eu^{3+}$ and $Ce^{3+}/Tb^{3+}/Yb^{3+}$ doped phosphors match well with concentration limitations. The matching JCPDS card number was 13-0483. In FTIR measurements, undoped and all of the doped phosphors were conferred with modes of $B_3O_9^{9-}$ groups.

Photoluminescence results indicated that although Ce^{3+} and Eu^{3+} doped phosphor showed significant emissions, these emissions resulted from transitions: from 5d to $^2F_{7/2}$ and $^2F_{5/2}$ for Ce^{3+} ion and $^5D_0 \rightarrow {}^7F_J$ (J=0,1,2,3,4) for Eu^{3+} ion. Dy^{3+} doped phosphors showed shallow activity in terms of luminescence; moreover, codoping with Ce^{3+} ion increases the emission of Dy^{3+}. With this energy transfer, the emission of Dy^{3+} ion increased six times. Therefore the emission of Dy^{3+} resulting from the transitions, $^4F_{9/2}$ to $^6H_{15/2}$, $^6H_{13/2,}$ and $^6H_{11/2}$, increased. For $Ce^{3+}/Tb^{3+}/Yb^{3+}$ triple doped $GdBO_3$ based phosphor also showed photoluminescence activity. Since the Ce^{3+}/Tb^{3+} doped phosphors were examined by our group previously, Yb^{3+} doped and triple doped phosphors were investigated by means of both downconversion and upconversion. In this part of the study, the emission of Tb^{3+} (transitions of $^5D_4$ to ^7F_J (J=6,4,3)) was concentrated.

Moreover, with the help of CIE calculations, the color of synthesized compounds can be predicted by an objective observer. Some of the compounds had a white color, and they can be used for LED production. Also, by changing the concentration of dopants and the wavelength of excitation light, the color of the resulting compound can be changed. This provides the tunability of the phosphors.

SEM images indicate that all $GdBO_3$ samples have adequate particle size and regular morphology. When the particle sizes of materials are compared, almost all often have similar particle sizes.

Measured luminescence decay lifetimes of samples were recorded to explain energy transfer between the ions. Single and double exponential behaviors were observed according to samples. For Ce^{3+} doped compound, the decay time was long. Relatively slow energy transfer was recorded between Ce^{3+} and Dy^{3+}. In the study, the decay time of 5% Ce^{3+} doped $GdBO_3$ was 0.026 ms. For 1% Dy^{3+}/3% Ce^{3+}, the average of decay lifetime was 0.72 ms.

Quantum efficiency calculations were made for the characterization of emissions by means of photon count. There was a significant value for quantum efficiency as 89.2% from Ce^{3+} single doped $GdBO_3$ phosphor, which related to four strong emissions centered at 403, 407, 415, 420 nm, and the quantum yield for Ce^{3+}/Dy^{3+} codoped phosphor was 4.3%.

APPENDICES

A. Photoluminescence Measurement of Ce^{3+} Doped $GdBO_3$ under 356 nm

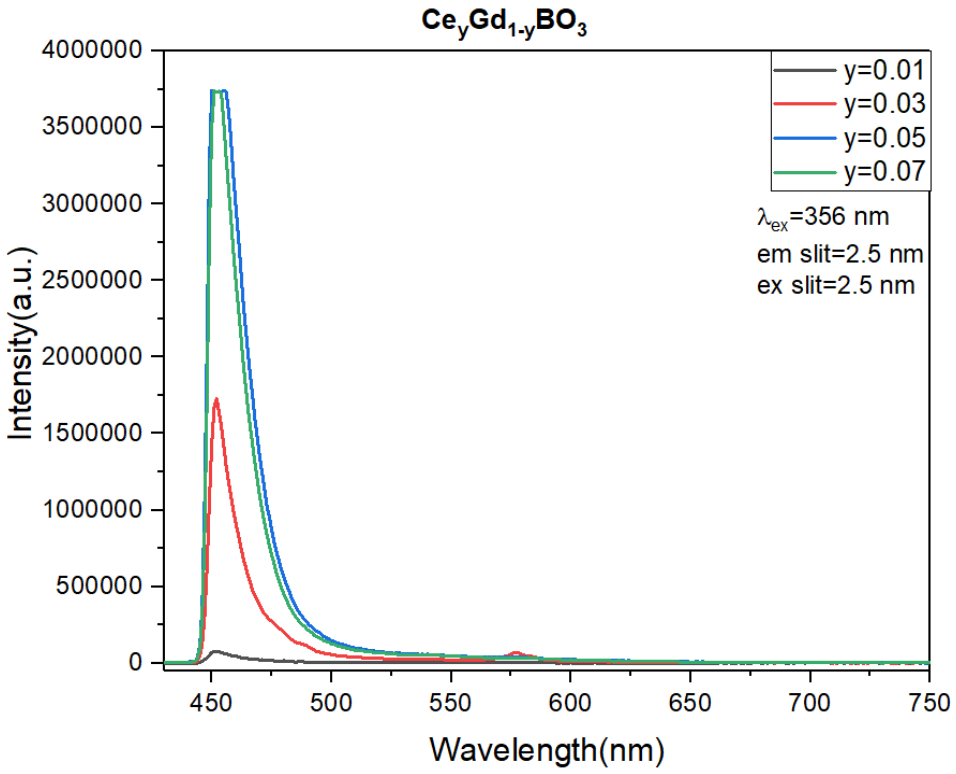

Figure 4.1. Photoluminescence Measurement of Ce^{3+} Doped $GdBO_3$ under 356 nm with filter

The photoluminescence emission (**Figure 3.33**) spectra were taken for the mole fractions as y = 0.01, 0.03, 0.05, 0.07. When the emission spectra were examined, it is seen that the best concentration for the light intensity of emission is at y = 0.05-mole concentration. Since after y= 0.05, the intensity of emitted light from the compound becomes narrower; therefore, it can be said that emission decreases after 5 % doping concentration.

B. Photoluminescence Measurement of Ce^{3+} Doped $GdBO_3$ under Excitation 331 nm

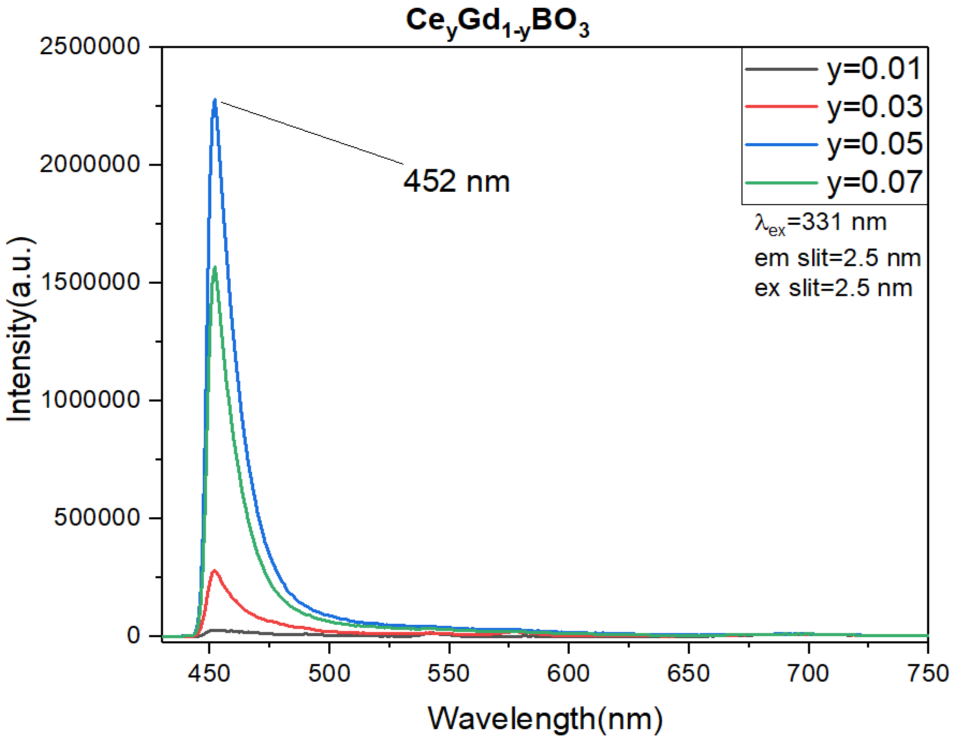

Figure 4.2. Photoluminescence measurement of Ce^{3+} doped $GdBO_3$ under excitation 331 nm

C. Photoluminescence Measurement of Ce^{3+}/Dy^{3+} Codoped $GdBO_3$ under Excitation 331 nm

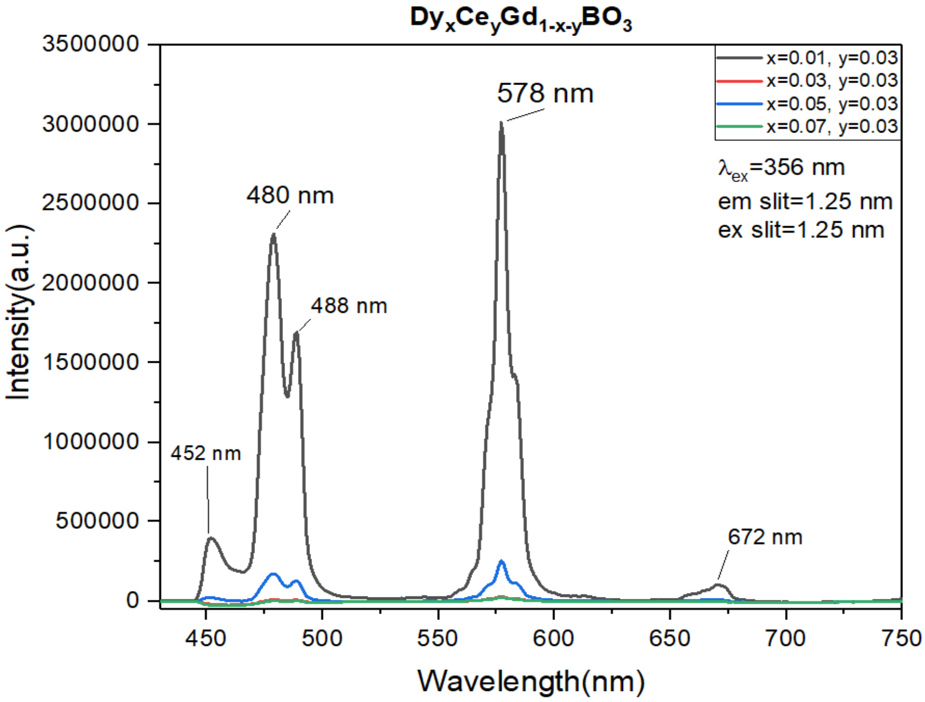

Figure 4.3. Photoluminescence measurement of Ce^{3+}/Dy^{3+} codoped $GdBO_3$ under Excitation 356 nm with an emission filter

D. Comparison of Intensities of Dy^{3+} Emission under excitation and Ce^{3+}/Dy^{3+} Cooped $GdBO_3$ Emission under Excitation 331 nm

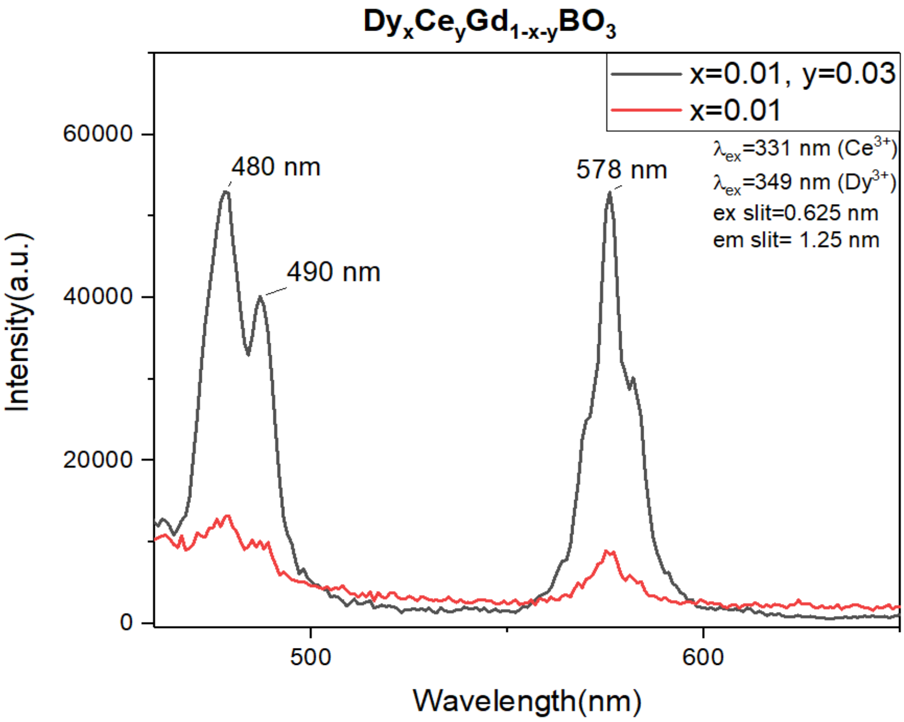

Figure 4.4. Photoluminescence measurements of Dy^{3+} doped under excitation and Ce^{3+}/Dy^{3+} Cooped $GdBO_3$ under Excitation 331 nm

Using these spectra shows that the emission of Dy^{3+} ion can be increased by a factor of 6 with Ce^{3+}-Dy^{3+} energy transfer. There was no filter used for emission in these measurements, so there was a peak around 660 nm from the excitation source; for that reason, the emission spectra were given in the range from 450 to 620 nm.

REFERENCES

Akman, P., Ulusan, S., Banerjee, S., & Yılmaz, A. (2020). Core-Shell type, Ce^{3+}, Tb^{3+} doped $GdBO_3$ system: Synthesis and Celecoxib Drug Delivery Application. *Microporous and Mesoporous Materials*. Elsevier Inc. https://doi.org/10.1016/j.eplepsyres.2019.106192

Alves, R. T., Trindade, C. M., Santos, W. Q., Gouveia-Neto, A. S., Bueno, L. A., Mathias, C. F., & Nalin, M. (2016). Dy^{3+}/Tb^{3+} -codoped tunable warm light-emitting fluorogermanate glass phosphor. *Optical Engineering*, *55*(11), 117103. https://doi.org/10.1117/1.oe.55.11.117103

Amami, J., Hreniak, D., Guyot, Y., Pazik, R., Strek, W., Goutaudier, C., & Boulon, G. (2007). New optical tools used for characterization of phase transitions in nonlinear nano-crystals. Example of Yb^{3+}-doped $BaTiO_3$. *Journal of Physics Condensed Matter*, *19*(9). https://doi.org/10.1088/0953-8984/19/9/096204

Ambast, A. K., Kunti, A. K., Som, S., & Sharma, S. K. (2013). Near-white-emitting phosphors based on tungstate for phosphor-converted light-emitting diodes. *Applied Optics*, *52*(35), 8424–8431. https://doi.org/10.1364/AO.52.008424

Arun Kumar, R., & Dhanasekaran, R. (2011). Growth and characterization of LCOB and NdLCOB single crystals for laser applications. *Journal of Crystal Growth*, *318*(1), 636–641. https://doi.org/10.1016/j.jcrysgro.2010.11.037

Auzel, F. (2004). Upconversion and Anti-Stokes Processes with f and d Ions in Solids. *Chemical Reviews*, *104*(1), 139–173. https://doi.org/10.1021/cr020357g

Bahadur, A., Dwivedi, Y., & Rai, S. B. (2013). Optical properties of cerium doped oxyfluoroborate glass. *Spectrochimica Acta - Part A: Molecular and Biomolecular Spectroscopy*, *110*, 400–403. https://doi.org/10.1016/j.saa.2013.03.066

Balachander, L., Ramadevudu, G., Shareefuddin, M., Sayanna, R., & Venudharc, Y. C. (2013). IR analysis of borate glasses containing three alkali oxides. *ScienceAsia*, *39*(3), 278–283. https://doi.org/10.2306/scienceasia1513-1874.2013.39.278

Berezin, M. Y., & Achilefu, S. (2011). Between the ideal and the real: Gender relations within the Indian joint family. *Chemical Reviews*, *110*(5), 36–63. https://doi.org/10.1021/cr900343z. Fluorescence

Bloembergen, N. (1959). Solid state infrared quantum counters. *Physical Review Letters*, *2*(3), 84–85. https://doi.org/10.1103/PhysRevLett.2.84

Capper, P., Kasap, S., & Willoughby, A. (2010). *Luminescent Materials and Applications*. *Bulk Crystal Growth of Electronic, Optical and Optoelectronic Materials*. Wiley Series in Materials for Electronic and Optoelectronic Applications. https://doi.org/10.1002/9780470012086

Chadeyron, G., El-Ghozzi, M., Mahiou, R., Arbus, A., & Cousseins, J. C. (1997). Revised Structure of the Orthoborate YBO_3. *Journal of Solid State Chemistry*, *128*(2), 261–266. https://doi.org/10.1006/jssc.1996.7207

Chengaiah, T., Kiran Kumar, K., & Rama Moorthy, L. (2018). Preparation and luminescence properties of Dy^{3+}-doped $Na^3Gd(PO_4)_2$ nanophosphor for solid state white LEDs. *Materials Today: Proceedings*, *5*(10), 21232–21240. https://doi.org/10.1016/j.matpr.2018.06.523

Cornelis R. Ronda. (2008). *Luminescence: From Theory to Application*. (C. R. Ronda, Ed.). WILEY-VCH Verlad Gmb&Co. KGaA.

Crosby, G. A., & Demas, J. N. (1971). Measurement of photoluminescence quantum yields. Review. *The Journal of Physical Chemistry*, *75*(8), 991–1024. https://doi.org/10.1021/j100678a001

Devi, H. F., Devi, K. T., & Singh, T. D. (2020). Synthesis, Characterization, Optical and Electrical Properties of Citrate Mediated Terbium Doped ZnO Nanoparticles for Multifunctional Applications. *Integrated Ferroelectrics, 204*(1), 81–89. https://doi.org/10.1080/10584587.2019.1674976

Dieke, G. H., Crosswhite, H. M., & Dunn, B. (1961). Emission Spectra of the Doubly and Triply Ionized Rare Earths*. *Journal of the Optical Society of America*, *51*(8), 820. https://doi.org/10.1364/josa.51.000820

Dobretsova, E. A., Borovikova, E. Y., Boldyrev, K. N., Kurazhkovskaya, V. S., & Leonyuk, N. I. (2014). IR spectroscopy of rare-earth aluminum borates $RAl_3(BO_3)_4$ (R = Y, Pr-Yb). *Optics and Spectroscopy (English Translation of Optika i Spektroskopiya), 116*(1), 77–83. https://doi.org/10.1134/S0030400X14010068

Duan, C., Liang, L., Li, L., Zhang, R., & Xu, Z. P. (2018). Recent progress in upconversion luminescence nanomaterials for biomedical applications. *Journal of Materials Chemistry B, 6*(2), 192–209. https://doi.org/10.1039/c7tb02527k

Edukondalu, A., Srinivasu, C., Rahman, S., Sathe, V., & Kumar, K. S. (2014). Raman spectroscopic studies on mixed alkali borotungsten glasses. *AIP Conference Proceedings*, *1591*(March), 836–838. https://doi.org/10.1063/1.4872773

Fang, Z., Cao, R., Zhang, F., Ma, Z., Dong, G., & Qiu, J. (2014). Efficient spectral conversion from visible to near-infrared in transparent glass ceramics containing Ce^{3+}-Yb^{3+} codoped $Y_3Al_5O_{12}$ nanocrystals. *Journal of Materials Chemistry C*, *2*(12), 2204–2211. https://doi.org/10.1039/c3tc32231a

Gribovskii, V. P., A. M. S. S., Myhajlenko, S., Ghose, D., Hippler, R., Gumlich, H.-E., Zeinert, A., … Chandra, E. L. D. (1998). *Luminescence of Solids*. (D. R. Vij, Ed.), *Luminescence of Solids*. https://doi.org/10.1007/978-1-4615-5361-8

Grobelna, B., Synak, A., & Bojarski, P. (2012). The luminescence properties of dysprosium ions in silica xerogel doped with $Gd_{1.6}Dy_{0.4}(WO_4)_3$. *Optica Applicata*, *42*(2), 337–344. https://doi.org/10.5277/oa120211

Han, L., Sun, Y., & Sun, J. (2016). Synthesis and luminescence properties of white-light-emitting phosphor $Sr_3GdNa(PO_4)_3F:Dy^{3+}$. *Journal of Rare Earths, 34*(1), 12–16. https://doi.org/10.1016/S1002-0721(14)60571-8

Helvaci, C. (2015). Borates. In R. C. Selley (Ed.). Elsevier Ltd.

Herrmann, A., Othman, H. A., Assadi, A. A., Tiegel, M., Kuhn, S., & Rüssel, C. (2015). Spectroscopic properties of cerium-doped aluminosilicate glasses. *Optical Materials Express*, *5*(4), 720. https://doi.org/10.1364/ome.5.000720

Hızal Abacı, Ö. C., Mete, E., Esenturk, O., & Yılmaz, A. (2019). Tunable optical properties and DFT calculations of RE^{3+} codoped $LaBO_3$ phosphors. *Optical Materials, 98*(December). https://doi.org/10.1016/j.optmat.2019.109487

Hussin, R., Hamdan, S., Halim, D. N. F. A., & Husin, M. S. (2010). The origin of emission in strontium magnesium pyrophosphate doped with Dy_2O_3. *Materials Chemistry and Physics*, *121*(1–2), 37–41. https://doi.org/10.1016/j.matchemphys.2009.12.033

Isokawa, Y., Hirano, S., Kawano, N., Okada, G., Kawaguchi, N., & Yanagida, T. (2018). Dosimetric and scintillation properties of Ce-doped Li_3PO_4-B_2O_3 glasses. *Journal of Non-Crystalline Solids, 487*(November 2017), 1–6. https://doi.org/10.1016/j.jnoncrysol.2018.02.015

Jain, A., Blum, C., & Subramaniam, V. (2009). Fluorescence Lifetime Spectroscopy and Imaging of Visible Fluorescent Proteins. In *Advances in Biomedical Engineering* (First Edit, pp. 147–176). Elsevier. https://doi.org/10.1016/B978-0-444-53075-2.00004-6

Jia, G., Zhang, C., Wang, C., Liu, L., Huang, C., & Ding, S. (2012). Uniform and well-dispersed $LaBO_3$ hierarchical architectures: Synthesis, formation, and luminescence properties. *CrystEngComm*, *14*(2), 579–584.

https://doi.org/10.1039/c1ce05973d

Juárez-Batalla, J., Meza-Rocha, A. N., Muñoz, G. H., Camarillo, I., & Caldiño, U. (2016). Luminescence properties of Tb^{3+}-doped zinc phosphate glasses for green laser application. *Optical Materials*, *58*, 406–411. https://doi.org/10.1016/j.optmat.2016.06.022

Jung, K. Y., Kim, E. J., & Kang, Y. C. (2004). Morphology Control and Optimization of Luminescent Property of YBO_3:Tb Phosphor Particles Prepared by Spray Pyrolysis. *Journal of The Electrochemical Society*, *151*(3), H69. https://doi.org/10.1149/1.1646155

Kesavulu, C. R., & Jayasankar, C. K. (2011). White light emission in Dy^{3+}-doped lead fluorophosphate glasses. *Materials Chemistry and Physics*, *130*(3), 1078–1085. https://doi.org/10.1016/j.matchemphys.2011.08.037

Khan, I., Rooh, G., Rajaramakrishna, R., Srisittipokakun, N., Wongdeeying, C., Kiwsakunkran, N., … Tuscharoen, S. (2019). Photoluminescence and white light generation of Dy_2O_3 doped Li_2O-BaO-Gd_2O_3- SiO_2 for white light LED. *Journal of Alloys and Compounds*, *774*, 244–254. https://doi.org/10.1016/j.jallcom.2018.09.156

Kubasiewicz, K., Runowski, M., Lis, S., & Szczeszak, A. (2015). Synthesis, structural and spectroscopic studies on $GdBO_3$:Yb^{3+}/Tb^{3+}@SiO2 core-shell nanostructures. *Journal of Rare Earths*, *33*(11), 1148–1154. https://doi.org/10.1016/S1002-0721(14)60539-1

Lapaev, D. V., G.Nikiforov, V., Lobkov, V. S., Knyazev, A. A., Ziyatdinova, R. M., & Galyametdinov, Y. G. (2020). A vitrified film of an anisometric europium(III) b-diketonate complex with a low melting point as a reusable luminescent temperature probe with excellent sensitivity in the range of 270–370 K. *Journal of Materials Chemistry C*, 27–29. https://doi.org/10.1039/d0tc00625d

LEVIN, E. M., ROTH, R. S., & MARTIN, J. B. (1961). POLYMRPHISM OF

ABO3 TYPE RARE EARTH BORATES. *THE AMERICAN MINERALOGIST, 46*(1954), 1030–1055.

Leyre, S., Coutino-Gonzalez, E., Joos, J. J., Ryckaert, J., Meuret, Y., Poelman, D., … Hanselaer, P. (2014). Absolute determination of photoluminescence quantum efficiency using an integrating sphere setup. *Review of Scientific Instruments, 85*(12). https://doi.org/10.1063/1.4903852

Lindon, J. C., Tranter, G. E., & Holmes, J. L. (Eds.). (1942). *Encyclopedia of Spectroscopy and Spectrometry* (Vol. 1–3). Academic Press.

Lu, Q. F., Li, J., & Wang, D. J. (2013). Single-phased silicate-hosted phosphor with 660 nm-featured band emission for biological light-emitting diodes. *Current Applied Physics, 13*(7), 1506–1511. https://doi.org/10.1016/j.cap.2013.05.013

Luyanda L. Noto, Hendrik C. Swart, Bakang M. Mothudi, P. S. M. and M. S. D. (2011). The Dynamics of Luminescence. In *Luminescence - An Outlook on the Phenomena and their Applications* (pp. 95–115). INTECH.

Maccari, S., Piazza, P. V., Marie, J., Angelucci, L., Simon, H., & I, M. L. M. (1991). *Solid State Luminescence Theory, materials and devices*. (A.H. Kitai, Ed.) (Vol. 548).

Mahata, M. K., Hofsäss, H. C., & Vetter, U. (2012). Photon-Upconverting Materials: Advances and Prospects for various Emerging Applications. In C. Yu, R. Chen, J. J. Li, J. J. Li, M. Drahansky, M. . Paridah, … J. Coates (Eds.), *Luminescence - An Outlook on the Phenomena and their Applications* (p. 13). https://doi.org/10.1016/j.colsurfa.2011.12.014

Mahata, M. K., Koppe, T., Hofsäss, H., Kumar, K., & Vetter, U. (2015). Host sensitized luminescence and time-resolved spectroscopy of YVO_4: Ho^{3+} nanocrystals. *Physics Procedia* (Vol. 76). Elsevier B.V. https://doi.org/10.1016/j.phpro.2015.10.023

Mazelev, L. Y. (1960). *Borate Glasses*. *Borate Glasses* (Vol. 12). https://doi.org/10.1007/978-1-4899-4677-5

Mellor, J. W. (1929). *A Comprehensive Treatise on Inorganic and Theoretical Chemistry V* (Vol. V (B, Al,). NEWYORK, TORONTO: LONGSMAN, GREEN AND CO. LTD.

Miyakawa, T., & Dexter, D. L. (1970). Phonon sidebands, multiphonon relaxation of excited states, and phonon-assisted energy transfer between ions in solids. *Physical Review B*, *1*(7), 2961–2969. https://doi.org/10.1103/PhysRevB.1.2961

Nair, R. G., Nigam, S., Sudarsan, V., Rao, R., Vatsa, R. K., & Jain, V. K. (2018). Synthesis Conditions on the Nature of $GdBO_3$ Phase Formed. *Chemistry Select*, *3*(26), 7496–7506. https://doi.org/10.1002/slct.201801409

Nassar, E. J., Ciuffi, K. J., Calefi, P. S., Avila, L. L., Bandeira, L. C., Cestari, A., … Matos, M. G. (2009). Europium III: Different Emission Spectra in Different Matrices, the Same Element. In L. M. Moreno (Ed.), *Europium: Compounds, Production and Applications* (pp. 11–22).

Nawalha, H. S., & Rohwer, L. S. (2003). *Handbook of Luminescence, display materials and devices*. American Scientific Publishers.

Neharika, Kumar, V., Singh, V. K., Sharma, J., Ntwaeaborwa, O. M., & Swart, H. C. (2016). Synthesis and photoluminescence study of a single dopant near white light emitting $Li_4CaB_2O_6:Dy^{3+}$nanophosphor. *Journal of Alloys and Compounds*, *688*, 939–945. https://doi.org/10.1016/j.jallcom.2016.07.039

Nyk, M., Kumar, R., Ohulchanskyy, T. Y., Bergey, E. J., & Prasad, P. N. (2008). High contrast in vitro and in vivo photoluminescence bioimaging using near infrared to near infrared up-conversion in Tm^{3+} and Yb^{3+} doped fluoride nanophosphors. *Nano Letters*, *8*(11), 3834–3838. https://doi.org/10.1021/nl802223f

Pantazis, P., Maloney, J., Wu, D., & Fraser, S. E. (2010). Second harmonic generating (SHG) nanoprobes for in vivo imaging. *Proceedings of the National Academy of Sciences of the United States of America*, *107*(33), 14535–14540. https://doi.org/10.1073/pnas.1004748107

Pauwels, D., Masson, N. Le, Viana, B., A.Kahn-Harari, Loef, E. V. D. van, Dorenbos, P., & Eijk, C. W. E. van. (2000). A Novel Inorganic Scintillator: $LuSi_2O_7:Ce^{3+}$ (LPS). *IEEE TRANSACTIONS ON NUCLEAR SCIEKCE*, *47*(6), 1787–1790.

Pitscheider, A., Kaindl, R., Oeckler, O., & Huppertz, H. (2011). The crystal structure of π-$ErBO_3$: New single-crystal data for an old problem. *Journal of Solid State Chemistry*, *184*(1), 149–153. https://doi.org/10.1016/j.jssc.2010.11.018

Potdevin, A., Chadeyron, G., Boyer, D., Caillier, B., & Mahiou, R. (2005). Sol-gel based YAG : Tb^{3+} or Eu^{3+} phosphors for application in lighting sources. *Journal of Physics D: Applied Physics*, *38*(17), 3251–3260. https://doi.org/10.1088/0022-3727/38/17/S29

Prasad, A., Rao, A. S., Gupta, M., & Prakash, G. V. (2018). Morphological and luminescence studies on $KGdF_4:Yb^{3+}/Tb^{3+}$ up-conversion nanophosphors. *Materials Chemistry and Physics*, *219*(April), 13–21. https://doi.org/10.1016/j.matchemphys.2018.07.056

Ren, M., Lin, J. H., Dong, Y., Yang, L. Q., Su, M. Z., & You, L. P. (1999). Structure and phase transition of $GdBO_3$. *Chemistry of Materials*, *11*(6), 1576–1580. https://doi.org/10.1021/cm990022o

Sauer, M., Hofkens, J., & Enderlein, J. (2011). *Handbook of Fluorescence Spectroscopy and Imaging-From Single Molecules to Ensembles*. Singapore: WILLEY-VCH.

Scanda, J. (Ed.). (2007). *COLORIMETRY-Understandimgthe CIE System*. Hoboken: JOHN WILEY & SONS, INC., PUBLICATION.

SEYYİDOĞLU, S. (2009). Synthesis and Characterization of Novel Rare Earth Phosphates and Rietveld Structural Analysis of Rare Earth Orthoborates, (September), 209.

Shang, M., Li, C., & Lin, J. (2014). How to produce white light in a single-phase host? *Chemical Society Reviews*, *43*(5), 1372–1386. https://doi.org/10.1039/c3cs60314h

Shrivastava, N., Khan, L. U., Khan, Z. U., Vargas, J. M., Moscoso-Londoño, O., Ospina, C., … Sharma, S. K. (2017). Building block magneto-luminescent nanomaterials of iron-oxide/ZnS@LaF_3:Ce^{3+},Gd^{3+},Tb^{3+} with green emission. *Journal of Materials Chemistry C*, *5*(9), 2282–2290. https://doi.org/10.1039/c6tc05053k

Shyichuk, A. (2015). *Synthesis, physicochemical characterization and computational studies of selected lanthanide-doped luminophores*.

Singh-Rachford, T. N., & Castellano, F. N. (2010). Photon upconversion based on sensitized triplet-triplet annihilation. *Coordination Chemistry Reviews*, *254*(21–22), 2560–2573. https://doi.org/10.1016/j.ccr.2010.01.003

Song, Y., Guo, N., & You, H. (2011). Synthesis and luminescent properties of Cerium-, Terbium-, or Dysprosium-doped $Gd_4Si_2O_7N_2$ materials. *European Journal of Inorganic Chemistry*, (14), 2327–2332. https://doi.org/10.1002/ejic.201001150

Sorokina, I. T. (2003). Solid-State Mid-Infrared Laser Sources. *Solid-State Mid-Infrared Laser Sources*, (May). https://doi.org/10.1007/3-540-36491-9

Sun, M., Ma, L., Chen, B. J., Stepongzi, F., Liu, F., Pan, Z. W., … Wang, X. J. (2014). Comparison of up-converted emissions in Yb^{3+}, Er^{3+} co-doped $Gd_2(WO_4)_3$ and Gd_2WO 6 phosphors. *Journal of Luminescence*, *152*(October 2017), 218–221. https://doi.org/10.1016/j.jlumin.2013.10.047

Szczeszak, A., Grzyb, T., Lis, S., & Wiglusz, R. J. (2012). Revision of structural properties of $GdBO_3$ nanopowders doped with Eu^{3+} ions through spectroscopic studies. *Journal of the Chemical Society. Dalton Transactions, 41*(19), 5824–5831. https://doi.org/10.1039/c2dt12154a

Thejo Kalyani, N., & Dhoble, S. J. (2012). Organic light emitting diodes: Energy saving lighting technology - A review. *Renewable and Sustainable Energy Reviews*, *16*(5), 2696–2723. https://doi.org/10.1016/j.rser.2012.02.021

Tian, G., Zheng, X., Zhang, X., Yin, W., Yu, J., Wang, D., … Zhao, Y. (2015). TPGS-stabilized $NaYbF_4$: ER Upconversion nanoparticles for dual-modal fluorescent/CT imaging and anticancer drug delivery to overcome multi-drug resistance. *Biomaterials*, *40*, 107–116. https://doi.org/10.1016/j.biomaterials.2014.11.022

Trupke, T., Shalav, A., Richards, B. S., Würfel, P., & Green, M. A. (2006). Efficiency enhancement of solar cells by luminescent up-conversion of sunlight. *Solar Energy Materials and Solar Cells*, *90*(18–19), 3327–3338. https://doi.org/10.1016/j.solmat.2005.09.021

Valeur, B., & Berberan-Santos, M. N. (2012). *Molecular Fluorescence-Principles and Applications* (Second). Weinheim: WILEY-VCH Verlad Gmb&Co. KGaA.

Velchuri, R., Kumar, B. V., Devi, V. R., Prasad, G., Prakash, D. J., & Vithal, M. (2011). Preparation and characterization of rare earth orthoborates, $LnBO_3$ (Ln = Tb, La, Pr, Nd, Sm, Eu, Gd, Dy, Y) and LaBO3:Gd, Tb, Eu by metathesis reaction: ESR of $LaBO_3$:Gd and luminescence of $LaBO_3$:Tb, Eu. *Materials Research Bulletin*, *46*(8), 1219–1226. https://doi.org/10.1016/j.materresbull.2011.04.006

Vengosh, A., Heumann, K. G., Juraske, S., & Kasher, R. (1994). Boron Isotope Application for Tracing Sources of Contamination in Groundwater. *Environmental Science and Technology*, *28*(11), 1968–1974. https://doi.org/10.1021/es00060a030

Virk, H. S. (Ed.). (2014). *Luminescence - Basic Concepts, Applications and Instrumentation*. https://doi.org/10.1007/s13398-014-0173-7.2

Vu, T. H. Q., Bondzior, B., Stefanska, D., Miniajluk, N., & Deren, P. J. (2020). Synthesis, Structure, Morphology, and Luminescent Properties of Ba_2MgWO_6:Eu^{3+} Double Perovskite Obtained by a Novel Co-Precipitation Method. *Materials*, *13*(1614). https://doi.org/10.3390/ma13071614

Wang, F., Deng, R., Wang, J., Wang, Q., Han, Y., Zhu, H., … Liu, X. (2011). Tuning upconversion through energy migration in core-shell nanoparticles. *Nature Materials*, *10*(12), 968–973. https://doi.org/10.1038/nmat3149

Wang, F., Han, Y., Lim, C. S., Lu, Y., Wang, J., Xu, J., … Liu, X. (2010). Simultaneous phase and size control of upconversion nanocrystals through lanthanide doping. *Nature*, *463*(7284), 1061–1065. https://doi.org/10.1038/nature08777

Wen, S., Zhou, J., Schuck, P. J., Suh, Y. D., Schmidt, T. W., & Jin, D. (2019). Future and challenges for hybrid upconversion nanosystems. *Nature Photonics*, *13*(12), 828–838. https://doi.org/10.1038/s41566-019-0528-x

Winefordner, J. D. (1963). of Atomic Emission Lines in Emission Flame Photometry and Absorption Lines in Absorption Flame Photometry, *17*(5).

Wong, K.-L., Bünzli, J.-C. G., & Tanner, P. A. (2020). Quantum yield and brightness. *Journal of Luminescence*, 117256. https://doi.org/10.1016/j.jlumin.2020.117256

Woods, W. G. (1994). An introduction to boron: History, sources, uses, and chemistry. *Environmental Health Perspectives*, *102*(SUPPL. 7), 5–11. https://doi.org/10.2307/3431956

Wu, J., Zhang, L., Ben, Y., Chen, H., Fu, X., & Wong, C. (2017). Improved full-color emission and switched luminescence in single $Ca_3(PO_4)_2$: Dy^{3+}, Eu3+phosphors for white LEDs. *Journal of Alloys and Compounds*, *697*(2017), 215–221. https://doi.org/10.1016/j.jallcom.2016.12.135

Wu, M., Congreve, D. N., Wilson, M. W. B., Jean, J., Geva, N., Welborn, M., … Baldo, M. A. (2016). Solid-state infrared-to-visible upconversion sensitized by colloidal nanocrystals. *Nature Photonics*, *10*(1), 31–34. https://doi.org/10.1038/nphoton.2015.226

Wu, Y., Tian, M., Peng, J., Koschan, M., Greeley, I., Foster, C., & Melcher, C. L. (2019). On the Role of Li^+ Codoping in Simultaneous Improvement of Light Yield, Decay Time, and Afterglow of $Lu_2SiO_5:Ce^{3+}$ Scintillation Detectors. *Physica Status Solidi - Rapid Research Letters*, *13*(2), 1–5. https://doi.org/10.1002/pssr.201800472

Würth, C., Grabolle, M., Pauli, J., Spieles, M., & Resch-Genger, U. (2011). Comparison of methods and achievable uncertainties for the relative and absolute measurement of photoluminescence quantum yields. *Analytical Chemistry*, *83*(9), 3431–3439. https://doi.org/10.1021/ac2000303

Yang, C. H., Pan, Y. X., & Zhang, Q. Y. (2007). Enhanced white light emission from Dy^{3+}/Ce^{3+} codoped $GdAl_3(BO_3)_4$ phosphors by combustion synthesis. *Materials Science and Engineering B: Solid-State Materials for Advanced Technology*, *137*(1–3), 195–199. https://doi.org/10.1016/j.mseb.2006.11.010

Yang, Z., Li, T., Li, P., Wang, Z., Xu, S., Bai, Q., & Dong, H. (2016). Synthesis and luminescence properties of novel white emitting phosphor $KMgLa(PO_4)_2:Dy^{3+}$. *Journal of Luminescence*, *178*, 178–182. https://doi.org/10.1016/j.jlumin.2016.05.053

Zhang, H., Chen, Z. H., Liu, X., & Zhang, F. (2020). A mini-review on recent progress of new sensitizers for luminescence of lanthanide doped nanomaterials. *Nano Research*, *12*(1). https://doi.org/10.1007/s12274-020-2661-8

Zhang, Q. Y., & Huang, X. Y. (2010). Recent progress in quantum cutting phosphors. *Progress in Materials Science*, *55*(5), 353–427.

https://doi.org/10.1016/j.pmatsci.2009.10.001

Zhang, Z. J., Jin, T. T., Xu, M. M., Huang, Q. Z., Li, M. R., & Zhao, J. T. (2015). Low-temperature vaterite-type $LuBO_3$, a vacancy-stabilized phase synthesized at high temperature. *Inorganic Chemistry*, *54*(3), 969–975. https://doi.org/10.1021/ic502337x

Zhou, J. C., Yang, Z. L., Dong, W., Tang, R. J., Sun, L. D., & Yan, C. H. (2011). Bioimaging and toxicity assessments of near-infrared upconversion luminescent $NaYF_4$:Yb, Tm nanocrystals. *Biomaterials*, *32*(34), 9059–9067. https://doi.org/10.1016/j.biomaterials.2011.08.038

Zhou, J., Liu, Q., Feng, W., Sun, Y., & Li, F. (2015). Upconversion luminescent materials: Advances and applications. *Chemical Reviews*, *115*(1), 395–465. https://doi.org/10.1021/cr400478f

Zhou, L. Y., Wei, J. S., Shi, J. X., Gong, M. L., & Liang, H. Bin. (2008). A novel green phosphor $GdCaAlO_4:Tb^{3+}$ for PDP application. *Journal of Luminescence*, *128*(8), 1262–1266. https://doi.org/10.1016/j.jlumin.2007.12.030

Zmojda, J., Kochanowicz, M., Miluski, P., & Dorosz, D. (2014). Side-detecting optical fiber doped with Tb^{3+} for ultraviolet sensor application. *Fibers*, *2*(2), 150–157. https://doi.org/10.3390/fib2020150

Zulfiqar Ali Ahamed, S., Madhukar Reddy, C., & Deva Prasad Raju, B. (2013). Structural, thermal and optical investigations of Dy^{3+} ions doped lead containing lithium fluoroborate glasses for simulation of white light. *Optical Materials*, *35*(7), 1385–1394. https://doi.org/10.1016/j.optmat.2013.02.006